

AD-A149 529

THE EFFECT OF FILLER WIRE AND FLUX COMPOSITIONS ON THE
MICROSTRUCTURE AND (U) COLORADO SCHOOL OF MINES GOLDEN
DEPT OF METALLURGICAL ENGINEE. N A FLECK AUG 84

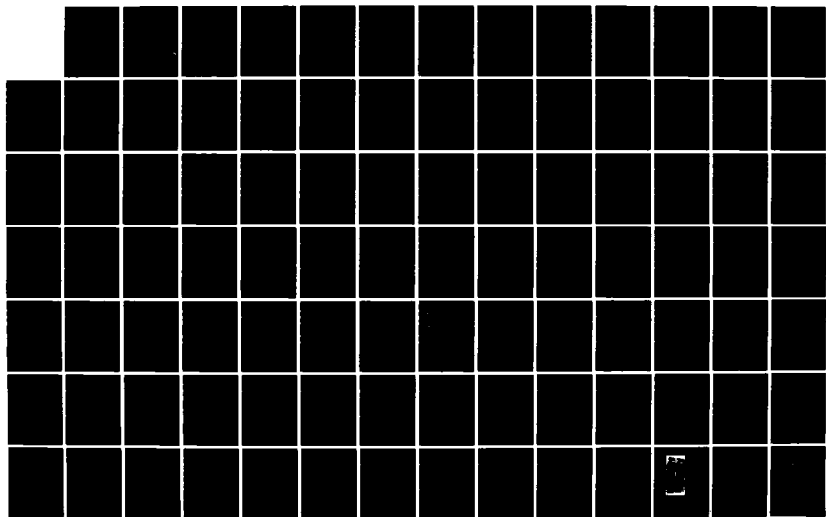
14

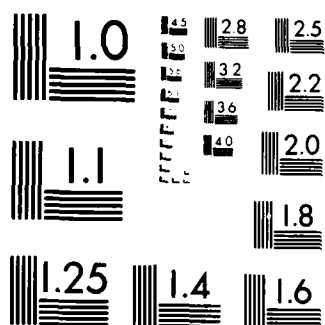
UNCLASSIFIED

DTNSRDC/SME-CR-17-84 N00014-83-K-0779

F/G 11/9

NL





MICROCOPY RESOLUTION TEST CHART
NATIONAL BUREAU OF STANDARDS-1963-A

AD-A149 529

DTNSRDC-SME-CR-17-84
Contract No: N00014-83-K-0779

THE EFFECT OF FILLER WIRE AND FLUX COMPOSITIONS ON THE MICROSTRUCTURE AND
PROPERTIES OF MICROALLOYED STEEL WELD METAL

by

Norbert A. Fleck, II

Center for Welding Research
Department of Metallurgical Engineering
Colorado School of Mines
Golden, Colorado 80401

August 1984

DTIC FILE COPY

DTIC
ELECTE
JAN 15 1985
A

APPROVED FOR PUBLIC RELEASE; DISTRIBUTION UNLIMITED

Prepared for
David W. Taylor Naval Ship R&D Center
Bethesda, Maryland 20084

85 01 08 163

UNCLASSIFIED

SECURITY CLASSIFICATION OF THIS PAGE (When Data Entered)

REPORT DOCUMENTATION PAGE		READ INSTRUCTIONS BEFORE COMPLETING FORM
1. REPORT NUMBER DTNSRDC/SME-CR-17-84	2. GOVT ACCESSION NO. AD-A149529	3. RECIPIENT'S CATALOG NUMBER
4. TITLE (and Subtitle) THE EFFECT OF FILLER WIRE AND FLUX COMPOSITONS ON THE MICROSTRUCTURE AND PROPERTIES OF MICROALLOYED STEEL WELD METAL		5. TYPE OF REPORT & PERIOD COVERED Research & Development
		6. PERFORMING ORG. REPORT NUMBER
7. AUTHOR(s) Norbert A. Fleck, II		8. CONTRACT OR GRANT NUMBER(s) N00014-83-K-0779
9. PERFORMING ORGANIZATION NAME AND ADDRESS Center for Welding Research Department of Metallurgical Engineering Colorado School of Mines Golden, Colorado 80401		10. PROGRAM ELEMENT PROJECT, TASK AREA & WORK UNIT NUMBERS Program Element 62761N Task Area SF-61-541-591 Work Unit 2803-134
11. CONTROLLING OFFICE NAME AND ADDRESS Naval Sea Systems Command (SEA 05R25) Washington, DC 20362		12. REPORT DATE August 1984
14. MONITORING AGENCY NAME & ADDRESS (if different from Controlling Office) David Taylor Naval Ship R&D Center Bethesda, Maryland 20084		13. NUMBER OF PAGES 130
		15. SECURITY CLASS. (of this report) UNCLASSIFIED
		15a. DECLASSIFICATION DOWNGRADING SCHEDULE
16. DISTRIBUTION STATEMENT (of this Report) APPROVED FOR PUBLIC RELEASE; DISTRIBUTION UNLIMITED		
17. DISTRIBUTION STATEMENT (of the abstract entered in Block 20, if different from Report)		
18. SUPPLEMENTARY NOTES		
19. KEY WORDS (Continue on reverse side if necessary and identify by block number) HSLA Steel Submerged Arc Welding Microstructure Welding Carbon Equivalent Weld Metal Flux		
20. ABSTRACT (Continue on reverse side if necessary and identify by block number) (1 over)		

DD FORM 1 JAN 73 1473

EDITION OF 1 NOV 65 IS OBSOLETE

S N 0102-LF-014-6601

UNCLASSIFIED

SECURITY CLASSIFICATION OF THIS PAGE (When Data Entered)

SECURITY CLASSIFICATION OF THIS PAGE (When Data Entered)

Standard quantitative metallographic techniques were used to evaluate the volume fraction of the weld metal microconstituents, the acicular ferrite lath spacing, and the average prior austenite grain size. Along with hardness values, other weld metal properties were obtained from subsize (4.0 x 10.0 x 25.0 mm) Charpy V-Notch specimens, subsize (7.0 x 10 x 55.0 mm) Izod specimens, and subsize (5.0 x 2.5 x 101.6 mm) tensile specimens.

Results indicated that a commercial low SiO_2 , high CaF_2 flux, combined with a filler wire microalloyed with titanium, boron, and molybdenum, provided the optimal microstructure in terms of weld metal properties. Welding with a low SiO_2 flux was shown to produce high oxygen in the weld metal, a coarse acicular ferrite, and a low fraction of grain boundary ferrite. The study further indicated that replacing MgO with CaO in the flux produced a slightly coarser microstructure which exhibited poorer weld metal properties. This result implies that MgO does not simply substitute for CaO in submerged arc welding fluxes. The experimental results also showed that the low SiO_2 , high CaF_2 flux alone did not produce good weld metal microstructures in the absence of microalloyed filler wire. The percentages of acicular ferrite increased systematically with increase in the Ito-Bessyo carbon equivalent in the range of 0.17 - 0.22. Experimental mechanical testing confirmed the generally accepted principle that increasing volume fractions of fine acicular ferrite will result in improved weld metal properties. Further analysis indicated that increasing weld metal oxygen content in the range from 100 to 500 ppm reduced weld metal toughness through a austenite grain boundary pinning effect. At high oxygen content, fine oxide particles were assumed to refine the austenite grains, thereby allowing formation of larger fractions of grain boundary ferrite. The fractions of ferrite formed for a given grain size were shown to be consistent with fractions predicted by well-established overall transformation kinetics theory.

[illegible]

UNCLASSIFIED

SECURITY CLASSIFICATION OF THIS PAGE(When Data Entered)

ABSTRACT

Experimental submerged arc welds were made on quenched and tempered 3/4-in.-thick C-Mn-Mo-Nb plate using various combinations of filler wires and fluxes. The welds were made under conditions of constant heat input (75 kJ/in) and a constant deposition ratio of wire speed to travel speed of 13.

Standard quantitative metallographic techniques were used to evaluate the volume fraction of the weld metal microconstituents, the acicular ferrite lath spacing, and the average prior austenite grain size. Along with hardness values, other weld metal properties were obtained from subsize (5.0 x 10.0 x 55.0 mm) Charpy V-Notch specimens, subsize (7.6 x 7.6 x 55.0 mm) Izod specimens, and subsize (5.0 x 9.5 x 101.6 mm) tensile specimens.

Results indicated that a commercial low SiO_2 , high CaF_2 flux, combined with a filler wire microalloyed with titanium, boron, and molybdenum, provided the optimal microstructure in terms of weld metal properties. Welding with a high SiO_2 flux was shown to produce high oxygen in the weld metal, increasing the volume fraction of grain boundary ferrite. The study further indicated that replacing MgO with CaO in the flux produced a slightly

coarser microstructure which exhibited poorer weld metal properties. This result implies that MgO does not simply substitute for CaO in submerged arc welding fluxes. The experimental results also showed that the low SiO_2 , high CaF_2 flux alone did not produce good weld metal microstructures in the absence of microalloyed filler wire. The percentages of acicular ferrite increased systematically with increase in the Ito-Bessyo carbon equivalent in the range of 0.18 - 0.22. Experimental mechanical testing confirmed the generally accepted principle that increasing volume fractions of fine acicular ferrite will result in improved weld metal properties. Further analysis indicated that increasing weld metal oxygen content in the range from 100 to 500 ppm reduced weld metal toughness through a austenite grain boundary pinning effect. At high oxygen content, fine oxide particles were assumed to refine the austenite grains, thereby allowing formation of larger fractions of grain boundary ferrite. The fractions of ferrite formed for a given grain size were shown to be consistent with fractions predicted by well-established overall transformation kinetics theory.

TABLE OF CONTENTS

	Page
ABSTRACT.....	iii
TABLE OF CONTENTS.....	v
LIST OF FIGURES.....	viii
LIST OF TABLES.....	xv
ACKNOWLEDGEMENTS.....	xvi
I. INTRODUCTION.....	1
I.1. MICROALLOYED STEELS.....	1
I.2. WELDING CONSUMABLES.....	2
I.2.1. The Nature Of Fluxes.....	3
I.2.2. Chemical Reactions Of Submerged Arc Welding...	4
I.3. VARIOUS MICROSTRUCTURES OF HSLA WELDMENTS.....	13
I.4. FACTORS WHICH INFLUENCE THE WELD METAL MICROSTRUCTURE.....	22
I.4.1. Heat Input Effects.....	22
I.4.2. Weld Metal Composition Effects.....	24
I.4.3. Weld Metal Inclusion Effects.....	34
II. MATERIALS AND EXPERIMENTAL PROCEDURE.....	37
II.1. FLUX PREPARATION.....	37
II.2. WIRE PREPARATION.....	39
II.3. WELDING OPERATION.....	41

II.4.	METALLOGRAPHY.....	41
II.5.	CHEMICAL COMPOSITION.....	45
II.6.	HARDNESS.....	48
II.7.	MECHANICAL TESTING.....	48
II.8.	ELECTRON MICROSCOPY.....	51
III.	RESULTS AND DISCUSSION.....	54
III.1.	WELDING OPERATION.....	54
III.2.	WELD METAL MICROSTRUCTURAL ANALYSIS.....	57
III.3.	ELEMENT EFFECTS.....	65
III.4.	MECHANICAL TESTING.....	76
III.5.	EFFECT OF PRIOR AUSTENITE GRAIN SIZE.....	91
IV.	CONCLUSIONS.....	106
V.	REFERENCES CITED.....	109

APPENDICES

APPENDIX A.	Weld Metal Dilution, Weld Metal Penetration, And Bead Area Of The Welds.....	117
-------------	---	-----

APPENDIX B.	Summary Of The Average Acicular Ferrite Lath Size And The Average Prior Austenite Grain Size Diameter.....	118
-------------	--	-----

APPENDIX C.	Summary Of The Hardness Measurements Of The Welds.....	119
APPENDIX D.	Calculation Of The Amount Of Boron Per Grain Boundary Area Of The Weds.....	120
APPENDIX E.	Picture Of The Welding Equipment Used In This Study.....	121
APPENDIX F.	Simple And Cumulative Size Distribution Of The Inclusions Extracted From Weld TB-OP...	122
APPENDIX G.	Chemical Composition Of The Inclusions Extracted From Weld Tb-OP.....	123

LIST OF FIGURES

Figure No.	Title	Page
1.	Weld metal oxygen content as a function of CaF_2 and FeO additions to the flux.....	8
2.	Weld metal oxygen content as a function of FeO additions to the flux.....	11
3.	Examples of weld metal grain boundary ferrite (GF) and polygonal ferrite (PF) found in microalloyed HSLA steels. (2% nital etch) 750x...	15
4.	Example of weld metal ferrite with aligned second phase (AC) found in microalloyed HSLA steels. (2% nital etch) 750x.....	17
5.	Example of weld metal acicular ferrite (AF) found in microalloyed HSLA steels. (2% nital etch) 1500x.....	19
6.	Schematic of continuous cooling transformation diagram of a microalloyed HSLA steel weldment showing the different microconstituent start temperatures.....	20
7.	Examples of weld metal ferrite carbide (FC), grain boundary ferrite (GF), and acicular ferrite (AF) found in microalloyed HSLA steels. (2% nital etch) 1500x.....	21
8.	Schematic of continuous cooling transformation diagram of a microalloyed HSLA steel weldment showing the effect of two different cooling rates on weld metal microstructural transformation.....	23

9.	Schematic of continuous cooling transformation diagram of a microalloyed HSLA steel weldment showing the effects of hardenability on weld metal microstructural transformation.....	25
10.	Relationship between total titanium and insoluble titanium in microalloyed steel weld metal containing different amounts of aluminum and oxygen (61).....	32
11.	Relationship between total titanium and insoluble nitrogen in microalloyed steel weld metal containing different amounts of aluminum and oxygen (61).....	33
12.	Inclusion size distribution and type for (76) a. coarse grain boundary ferrite b. acicular ferrite.....	36
13.	Schematic of a microalloyed HSLA steel weldment showing the section from which the prior austenite grain size was measured. Also included is a weld metal micrograph showing the prior austenite grain boundaries. (5% nital etch) 100x.....	46
14.	Schematic of a microalloyed HSLA steel weldment showing the calculation for compositional differences.....	47
15.	Schematic of a submerged arc weld showing the dimensions and orientation of subsize Charpy V-Notch specimens.....	50
16.	Schematic of a submerged arc weld showing the dimensions and orientation of subsize Izod specimens.....	52
17.	Schematic of a submerged arc weld showing the dimensions and orientation of tensile barspecimens	53

18. Relationship between flux basicity and compositional differences in silicon and manganese of submerged arc welds performed on quenched and tempered C-Mn-Mo-Nb plate..... 56
- 19a. Centerline microstructures of four experimental submerged arc welds made on quenched and tempered C-MN-Mo-Nb plate. Welding consumables for each weld are given in Tables III and IV. All welds were made at a heat input of 75 KJ/in and a deposition ratio of 13. (2% nital etch) 500x.....
- 19b. Centerline microstructures of four experimental submerged arc welds made on quenched and tempered C-MN-Mo-Nb plate. Welding consumables for each weld are given in Tables III and IV. All welds were made at a heat input of 75 KJ/in and a deposition ratio of 13. (2% nital etch) 500x..... 59
20. The volume percentages of microconstituents observed at the weld center line of seven experimental submerged arc welds performed on quenched and tempered C-Mn-Mo-Nb plate..... 61
21. The mean acicular ferrite lath spacing observed at the center line of seven experimental submerged arc welds performed on quenched and tempered C-Mn-Mo-Nb plate..... 62
22. Hardness plotted as a function of acicular ferrite lath spacing of submerged arc welds performed on quenched and tempered C-Mn-Mo-Nb plate..... 64
23. The volume percentage of acicular ferrite of submerged arc welds performed on quenched and tempered C-Mn-Mo-Nb plate as a function of their respective Ito-Bessyo carbon equivalent numbers... 67

24. The volume percentage of primary ferrite of submerged arc welds performed on quenched and tempered C-Mn-Mo-Nb plate as a function of their respective Ito-Bessyo carbon equivalent numbers... 68
25. The volume percentage of grain boundary ferrite of submerged arc welds performed on quenched and tempered C-Mn-Mo-Nb plate as a function of their respective Ito-Bessyo carbon equivalent numbers... 69
26. The volume percentage of acicular ferrite of submerged arc welds performed on C-Mn-Si plate as a function of their respective Ito-Bessyo carbon equivalent numbers having two different levels of titanium..... 70
27. The volume percentage of acicular ferrite of submerged arc welds performed on quenched and tempered C-Mn-Mo-Nb plate as a function of their respective weld metal titanium contents..... 71
28. The volume percentage of acicular ferrite of submerged arc welds performed on quenched and tempered C-Mn-Mo-Nb plate as a function of their respective grain boundary boron concentrations.... 73
29. The volume percentage of grain boundary ferrite of submerged arc welds performed on quenched and tempered C-Mn-Mo-Nb plate as a function of their respective grain boundary boron concentrations.... 74
30. Subsize (5.0 x 10.0 x 55.0 mm) Charpy impact values of two submerged arc welds performed on quenched and tempered C-Mn-Mo-Nb plate as a function of temperature..... 77
31. Subsize (5.0 x 10.0 x 55.0 mm) Charpy fracture surfaces of two submerged arc welds performed on quenched and tempered C-Mn-Mo-Nb plate showing the effect of temperature on fracture appearance..... 78

32. Subsize (7.6 x 7.6 x 55.0 mm) Izod impact impact values of submerged arc welds performed on quenched and tempered C-Mn-Mo-Nb plate as a function of their respective acicular ferrite contents..... 80
33. Subsize (7.6 x 7.6 x 55.0 mm) Izod impact impact values of submerged arc welds performed on quenched and tempered C-Mn-Mo-Nb plate as a function of their respective primary ferrite contents..... 81
34. Subsize (7.6 x 7.6 x 55.0 mm) Izod fracture surfaces of seven submerged arc welds performed on quenched and tempered C-Mn-Mo-Nb plate showing the different fracture appearances produced at constant test temperature..... 82
35. The percent shear fracture area from subsize (7.6 x 7.6 x 55.0 mm) Izod specimens of submerged arc welds performed on quenched and tempered C-Mn-Mo-Nb plate as a function of their respective primary ferrite contents..... 83
36. Subsize (7.6 x 7.6 x 55.0 mm) Izod impact impact values of submerged arc welds performed on quenched and tempered C-Mn-Mo-Nb plate as a function of their respective acicular ferrite spacing..... 84
- 37a. Weld centerline fractographs of two subsize (7.6 x 7.6 x 55.0 mm) Izod specimens taken at the notch and 0.64 mm in from the notch. The specimen orientation is shown in Figure 16. Crack propagated from left to right. 1000x..... 86
- 37b. Weld centerline fractographs of two subsize (7.6 x 7.6 x 55.0 mm) Izod specimens taken at the notch and 0.64 mm in from the notch. The specimen orientation is shown in Figure 16. Crack propagated from left to right. 1000x..... 87

- 37c. Weld centerline fractographs of two subsize (7.6 x 7.6 x 55.0 mm) Izod specimens taken at the notch and 0.64 mm in from the notch. The specimen orientation is shown in Figure 16. Crack propagated from left to right. 1000x..... 88

- 37d. Weld centerline fractographs of two subsize (7.6 x 7.6 x 55.0 mm) Izod specimens taken at the notch and 0.64 mm in from the notch. The specimen orientation is shown in Figure 16. Crack propagated from left to right. 1000x..... 89

- 38. The volume percentage of grain boundary ferrite of submerged arc welds performed on quenched and tempered C-Mn-Mo-Nb plate as a function of their respective weld metal oxygen contents..... 92

- 39. The prior austenite grain diameter of submerged arc welds performed on quenched and tempered C-Mn-Mo-Nb plate as a function of their respective weld metal oxygen contents..... 93

- 40. Effect of weld metal oxygen content on the inclusion volume fraction (88)..... 95

- 41. Effect of weld metal oxygen content on the mean particle diameter (88)..... 96

- 42. The volume percentage of grain boundary ferrite of submerged arc welds performed on quenched and tempered C-Mn-Mo-Nb plate as a function of their respective prior austenite grain diameters..... 97

- 43. Schematic comparing low oxygen weld metal to high oxygen weld metal showing the Avrami relationship between the volume fraction of grain boundary ferrite and the prior austenite grain diameter.... 99

- 44. The volume fraction grain boundary ferrite of submerged arc welds performed on quenched and tempered C-Mn-Mo-Nb plate as a function of their respective prior austenite grain diameters..... 102
- 45. Schematic of a continuous cooling transformation diagram of a microalloyed HSLA steel weldment showing the effect of prior austenite grain size on weld metal microstructural transformation..... 105

LIST OF TABLES

Table No.	Title	Page
I.	Classification of Microstructures in Low C-Low Alloy Steel Weld Metal and Terminology (Review) (25).....	14
II.	Summary of the Optimal Amounts of Ti-B Addition Upon Submerged Arc Weld Metals.....	30
III.	Summary of Flux Compositions, in Weight Percent...	38
IV.	Summary of Welding Wire Composition, in Weight Percent.....	40
V.	Summary of Baseplate and Weld Metal Compositions, in Weight Percent.....	42
VI.	Summary of Welding Parameters for Experimental Welds.....	43
VII.	Compositional Differences of the Weld Metal, in Weight Percent.....	49

I. INTRODUCTION

I.1. MICROALLOYED STEELS

High strength, low-alloy (HSLA) steels, which have been developed for high strength and toughness applications such as arctic linepipes, are superior to plain carbon steels, but cost significantly less than alloy steels. Other desired properties of microalloyed steels include good weldability, good ductility, good formability, and high fracture resistance. Microalloyed steels are typically low carbon-manganese steels with small amounts of elements added such as niobium, vanadium, aluminum, or titanium. High yield strengths are largely obtained through a refinement of grain size, produced by the addition of these elements in combination with various forms of thermo-mechanical processing. In addition to increasing the yield strength, a fine ferrite grain size also enhances toughness and increases the ductility. The size distribution, shape, and volume fraction of non-metallic inclusions and second-phase particles will also influence the mechanical properties of HSLA steels.

Submerged arc weldments of microalloyed steel also obviously require high strength and toughness properties which are governed by the weld metal microstructure. The

optimal microstructure for carbon-manganese steel weld metals has been generally agreed upon to consist of a high amount of acicular ferrite (1). This fine grained, high angle grain boundary microstructure gives optimal weld metal strength and toughness properties. The influence on weld metal mechanical properties as controlled either by the microconstituents or by inclusions was investigated by Taylor and Farrar (2). They showed that below 300 ppm oxygen, the effects of the microconstituents were to dominate the mechanical behavior; between 300 and 600 ppm oxygen, there was shared microconstituent and inclusion control; and above 600 ppm oxygen, the inclusion effects were dominant. The mechanical properties are controlled by a number of factors including welding process parameters, (current, voltage, and travel speed), welding consumables, (composition of flux and filler wire), and base metal composition.

I.2. WELDING CONSUMABLES

The consumed materials in submerged arc welding include the wire electrode and the welding flux. The welding consumables contain balanced additions of various alloying elements (Nb, V, Cu, Ni, Cr, Mo, B) and complex deoxidizers (Si, Mn, Al, Ti) to develop the optimal weld metal

microstructure. Alloying elements may change toughness through solid solution effects in ferrite and modifications of the microstructure, which include grain size, the type of transformation product (hardenability), and the type of carbides produced. The microstructure and its related mechanical properties of HSLA weldments will depend on the multiple interactions of the welding consumables and the baseplate.

1.2.1 The Nature Of Fluxes

The submerged arc welding fluxes, which are granular, fuseable, mineral materials containing oxides or carbonates of manganese, silicon, calcium, magnesium, aluminum, titanium, sodium, and other compounds such as calcium fluoride, have a variety of functions (3) which include:

- 1) protecting the weld pool from the atmosphere (oxygen, nitrogen, and hydrogen).
- 2) deoxidizing the weld pool.
- 3) decreasing the impurities in the weld, or weld pool refining.
- 4) stabilizing the arc.
- 5) controlling the weld metal composition.
- 6) insulating the weld.

- 7) controlling the bead morphology.

I.2.2. Chemical Reactions Of Submerged Arc Welding

The chemical reactions occur very rapidly in welding as compared to ladle refining in steel because of both the extremely high metal temperatures involved, and the very large slag/metal and gas/metal interfacial area available for interaction. However, the characteristic non-isothermal nature of arc welding makes it is very difficult to outline the sequence of reactions taking place during various stages of the process. As a result, the understanding of weld metal chemistry is far less developed than that of steelmaking. As a consequence, predictions of the weld metal chemical composition, based on those of the welding consumables and the parent plate, must be done solely on empirical grounds, and it is only possible at present to describe the reaction pattern in general terms.

The chemical interactions taking place during submerged arc welding can be derived from a simplified two step reaction model proposed by Grong and Christensen (4). This model assumes:

- 1) A high temperature stage, where at least some of the reactions approach a state of

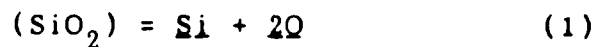
pseudo-equilibrium.

- 2) A cooling stage, where the concentrations established during the initial stage tend to re-adjust by precipitation of new phases.

In the case of submerged arc welding, the high temperature stage include both slag/metal and gas/metal interactions, the former factor being more important. This stage includes reactions occurring at the electrode tip, in the arc plasma, and in the hot part of the weld pool. The cooling stage starts immediately after the passage of the arc and is characterized by deoxidation reactions, such as precipitation of non-metallic inclusions in the bath, succeeded by a more or less complete separation of the dispersed particles. The boundary between the two stages is not very well defined, which means that deoxidation and phase separation may proceed simultaneously with oxidation in the hot part of the weld pool. In the following, the sequence of chemical reactions in submerged arc welding will be briefly discussed in light of this two stage model.

In submerged arc welding, the flux will be the main source of oxygen due to its content of easily reduced oxides such as SiO_2 , MnO , TiO_2 , etc. Consequently, during the high temperature stage, oxygen will be introduced into the weld

metal (location of the main reaction is not known at the present state) to an increasing extent, with an increasing oxygen potential of the flux, according to the overall reactions:



During cooling of the weld pool, a supersaturation with respect to the various deoxidation reactants is initially increasing. When the conditions for nucleation of the oxide inclusions are reached, deoxidation by a specific reactant will occur. Thus, conditions for competitive reactions between the various deoxidation elements, either introduced by the filler metal or the base metal, are established. These processes can lead to loss of certain deoxidation elements not present in the flux, and to a pickup of deoxidation elements present as oxides in the flux.

The degree of deoxidation achieved will be determined by the possibilities of the oxide inclusions to collide, grow, and float out of the weld pool before metal

solidification. As a result, it is very difficult to predict on theoretical grounds the final weld metal oxygen content.

Early investigators (5-8) attempted to improve the toughness of submerged arc welds by varying the standard high silica SiO_2 -CaO-MgO flux. Poor toughness properties were attributed to the large volume of inclusions and high amounts of oxygen and silicon in the welds. Lewis, et al.(8) obtained welds with lower oxygen contents (450 ppm as compared to 960 ppm) and fewer and smaller inclusions using a modified flux which consisted of 40% CaO, 20% SiO_2 , 20% CaF_2 , 10% MgO, and 5% TiO_2 . They found that CaF_2 and TiO_2 additions were beneficial in improving the weld metal toughness. Lower weld metal oxygen contents (and thus higher weld metal toughnesses) are now being obtained with new submerged arc welding fluxes that are based on lower silicon contents, and usually with a substantial CaF_2 content. Researchers have shown large variations in weld metal oxygen content with both FeO and CaF_2 additions to manganese silicate and calcium silicate flux systems, as shown in Figure 1 (9-10). Data such as these show the importance of developing advanced submerged arc welding fluxes to produce the optimal weld metal microstructure.

Researchers (11-12) have also shown that as the oxygen

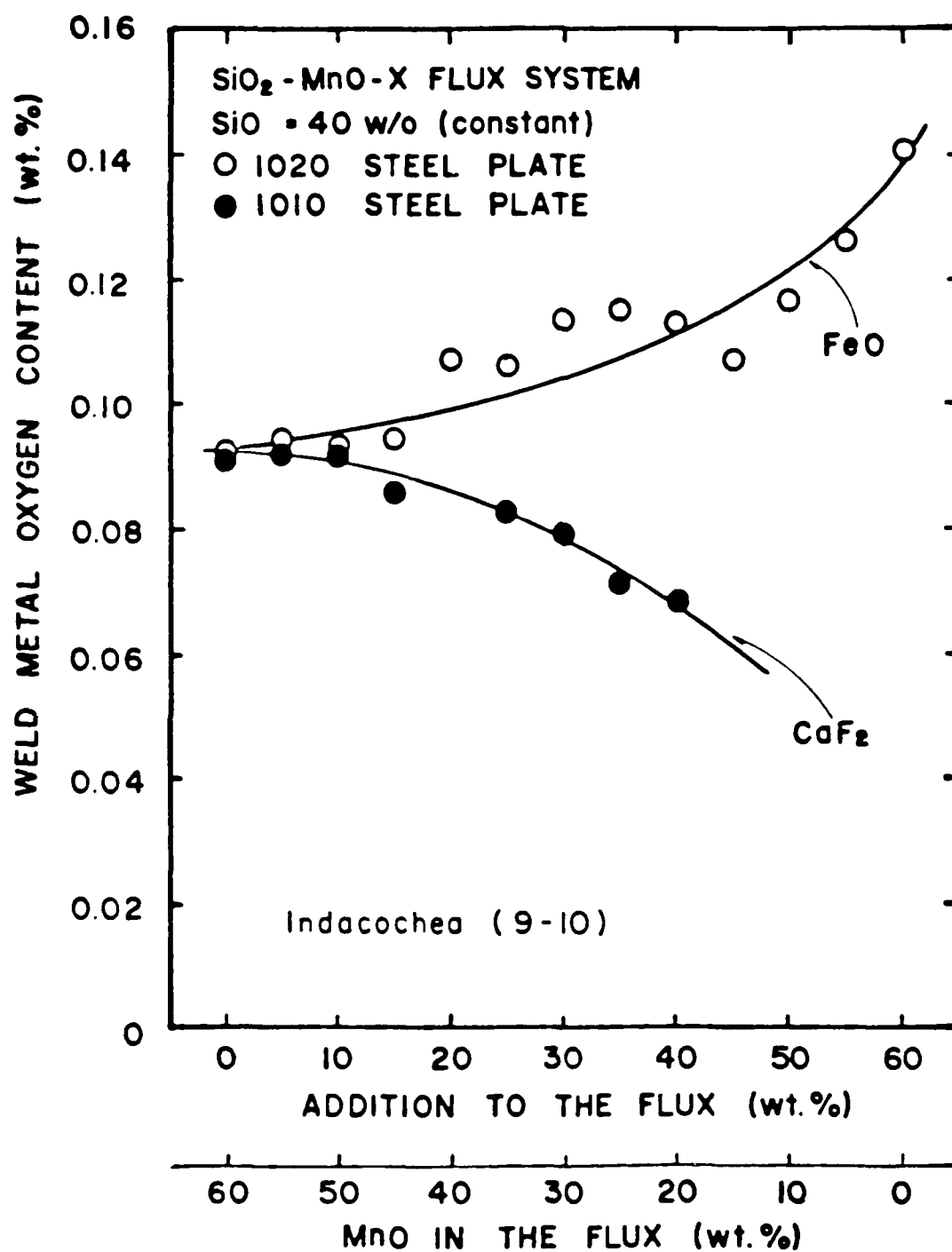


Figure 1. Weld metal oxygen content as a function of CaF₂ and FeO additions to the flux.

content varies due to different flux basicities, the inclusion composition will also change. In the iron and steel making industries, the concept of basicity is used to describe the refining behavior of the slag. Oxides are either classified as acid oxides or basic oxides depending on their capacity of forming or breaking anion networks. Tuliani, et al., (13), proposed a basicity index (BI) that is now the most commonly used in welding metallurgy today. It reads as follows:

$$BI = \frac{CaO + CaF_2 + MgO + K_2O + Na_2O + Li_2O + 1/2(MnO + FeO)}{SiO_2 + 1/2(Al_2O_3 + TiO_2 + ZrO_2)} \quad (4)$$

A decrease in the total number of non-metallic inclusions is normally associated with an increase in flux basicity. Researchers (13-16) have shown that an increase in flux basicity will decrease the amount of oxygen in the weld metal and improve toughness. Eager (17) has recently shown that, by using two different forms of the basicity equation, the weld metal oxygen content drops from 900 ppm to 300 ppm for a basicity index change from 0.5 to 1.5 and then remains constant with increasing basicity.

Tuliani, Boniszewski, and Eaton (13) admitted, however,

that their basicity index equation had a serious error in that it was unable to correlate the strength and toughness of welds made with high Al_2O_3 , TiO_2 , and ZrO_2 fluxes correctly. Submerged arc welds using a variety of reagent grade manganese silicate fused fluxes were made and studied by Indacochea and Olson (18). They found that by holding the SiO_2 content constant at 40 percent, the weld metal oxygen content increased with FeO additions (see Figure 2). These results contradict the basicity index theory wherein MnO and FeO are considered to have equivalent behavior. Palm (19) could not justify how the mechanical properties of the weld metal could be fully characterized by the basicity of the flux. Other researchers (20-21) also agreed that using the basicity index to determine the weld metal oxygen content was fortuitous. They (19) explained that the oxygen's chemical potential, which represents the driving force for oxygen transfer from the oxide flux to the weld metal, is the important factor involved, not basicity. A high acidic oxide such as Al_2O_3 has a very low oxygen chemical potential, while basic oxides such as FeO and MnO have relatively high oxygen chemical potentials.

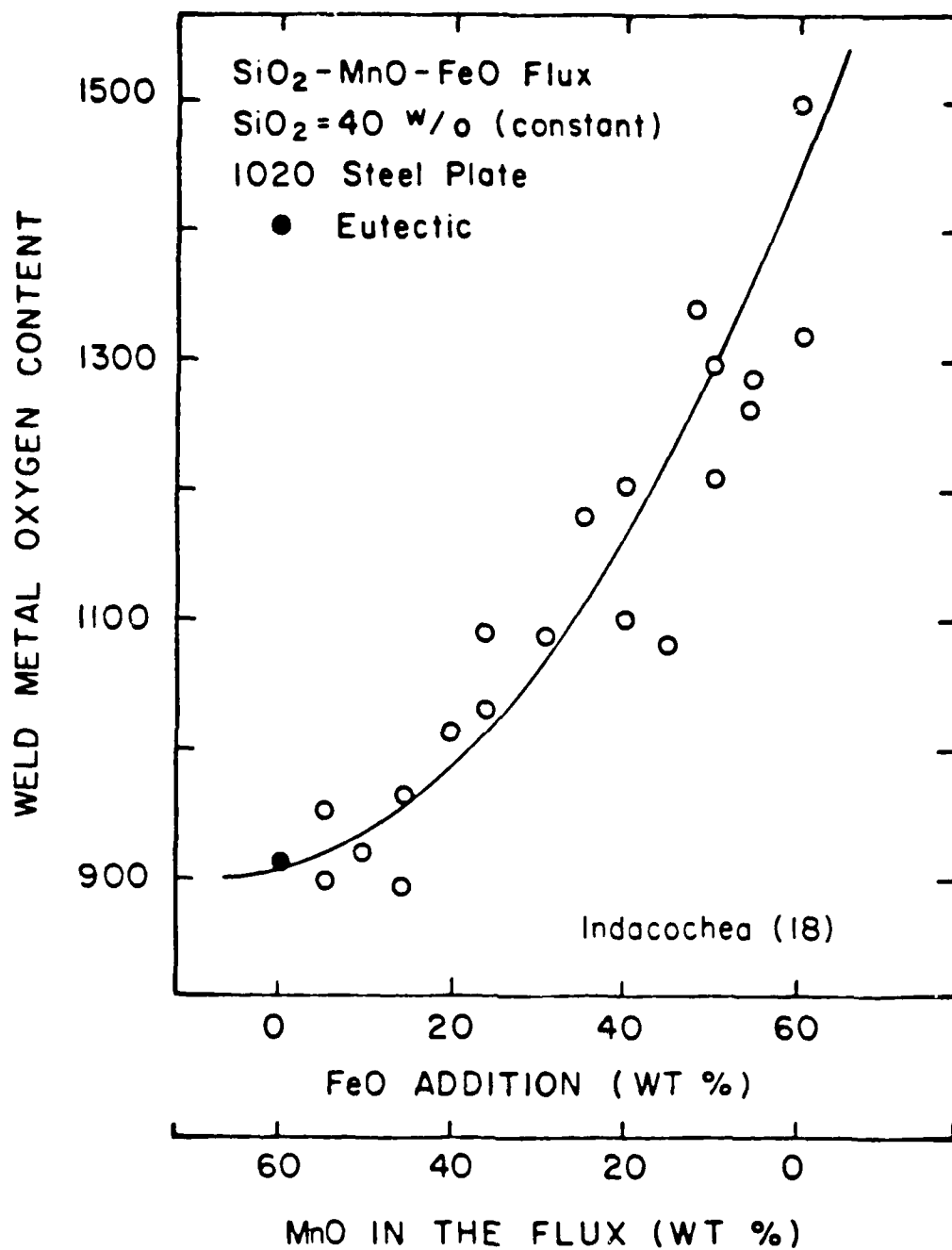


Figure 2. Weld metal oxygen content as a function of FeO additions to the flux.

An oxygen chemical potential equation for acidic fluxes was proposed by Noor (21):

$$O_f = \frac{100 - (\text{FeO} + \text{MnO} + \text{SiO}_2 + \text{TiO}_2)}{(\text{FeO} + \text{MnO} + \text{SiO}_2 + \text{TiO}_2)} \quad (5)$$

where O_f is the oxygen potential in the flux.

Unfortunately, this equation fails to predict the behavior of the more commonly used basic fluxes.

Other approaches to define basicity were also proposed and applied (22). Wood (23) suggested that the silica activity in the submerged arc welding flux should replace the basicity index. Wegrzyn (24) showed that the amount of manganese and silicon in the weld metal and the ratio of manganese to silicon could control the oxygen content in submerged arc welds made with neutral or basic fluxes. Although there have been multiple attempts to develop a simple parameter to represent the behavior of welding fluxes, none of them have been totally correct. Thus, more fundamental research in this area is necessary to develop an adequate empirical formula.

1.3. VARIOUS MICROSTRUCTURES OF HSLA WELDMENTS

The final weld metal microstructure, and thus toughness, in microalloyed steel results from the combined effects of the solidification structure and the corresponding decomposition of austenite on cooling. Numerous researchers (14,25-44) have attempted to characterize the weld metal microconstituents, and the terminology applied to these microstructures has not been universal, as shown in Table I. The metallographic terms used in this study follow the guidelines of Abson and Dolby (30). The five main categories of low carbon weld metal microstructure using these guidelines are: primary ferrite (F), ferrite with aligned second phase (AC), acicular ferrite (AF), ferrite-carbide aggregate (FC), and martensite (M).

1) Primary ferrite, which needs little or no undercooling, occurs by a nucleation and growth process. Primary ferrite occurs in two forms, grain boundary ferrite (GF) and polygonal ferrite (PF). When the cooling rate is extremely slow, grain boundary ferrite nucleates at the prior austenite grain boundaries. The ferrite grows in either elongated or granular form along the austenite grain boundaries, as shown in Figure 3. The grain boundary ferrite is usually considered detrimental in weldments

Table I. Classification of Microstructures in Low C-low Alloy Steel
Weld Metal and Terminology (Review) (25).

Dube, C.A. (26) Aaronsen, H.I. (27) Cochrane, R.C.* (28)	Widgery, D.J. (29)	Abson, D.J. (30)	Others (31-39)	Japanese researchers (14, 40-44)
Alloctriomorphic (polygonal) ferrite*	Proeutectoid ferrite	Grain boundary ferrite	Proeutectoid ferrite Grain boundary ferrite Polygonal ferrite Blocky ferrite	Proeutectoid ferrite Grain boundary ferrite Polygonal ferrite
		Polygonal ferrite	Perrite islands	Polygonal ferrite
Primary and secondary ferrite sideplates*	Lamellar component (product)	Perrite with aligned M A C	Perrite sideplate lath ferrite Upper bainite	Perrite sideplates lath like ferrite
Intragranular ferrite plates*	Acicular ferrite	Acicular ferrite	Acicular ferrite Fine bainitic ferrite	Acicular ferrite Needle like ferrite Fine grained ferrite
Massive ferrite				Granular ferrite
Microphases*				Granular ferrite
Pearlite	Pearlite	Perrite carbide aggregate Martensite M A constituent	Martensite M A constituent lath ferrite	Pearlite Martensite M A constituent High C martensite Upper bainite
Lath martensite Twinned martensite Retained austenite Upper (occasionally lower) bainite	Martensite			

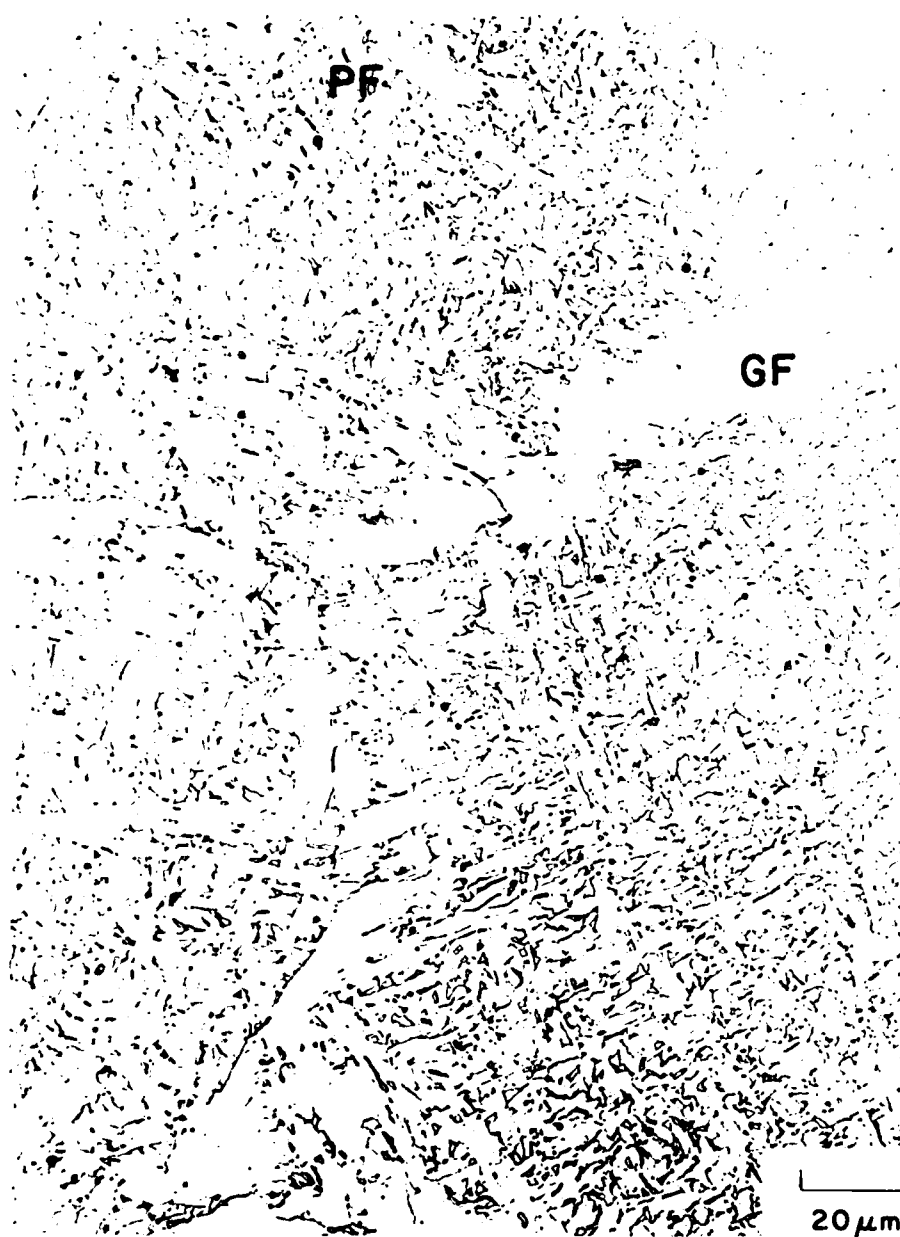


Figure 3. Examples of weld metal grain boundary ferrite (GF) and polygonal ferrite (PF) found in microalloyed HSLA steels. (2% nital etch) 750x.

because the ferrite veins provide for an easy crack propagation path. Figure 3 also gives an example of intragranular polygonal ferrite. Polygonal ferrite can be just as detrimental to the weld metal if it is sufficiently prevalent to provide a nearly continuous crack path.

2) Ferrite with aligned second phase requires some degree of undercooling. The boundary nucleated ferrite may grow away from the austenite grain boundary along a preferred growth direction as parallel laths as shown in Figure 4. Ferrite with aligned second phase is defined as two or more parallel laths of ferrite having an aspect ratio (length/width) greater than 4:1. A high proportion of coarse AC can decrease the weld metal toughness. A main problem using the guideline by Abson and Dolby is that sideplate ferrite and bainite are not distinguished, but are both categorized as "aligned carbide" morphologies. However, bainite and sideplate ferrite are formed by two totally different phase transformations. Bainite is a lower temperature transformation product than sideplate ferrite or acicular ferrite. During cooling, bainite forms as the final transformation product when acicular ferrite laths fail either to nucleate or to grow to mutual impingement.

3) Acicular ferrite, which requires a greater degree of undercooling than sideplate ferrite, is characterized by

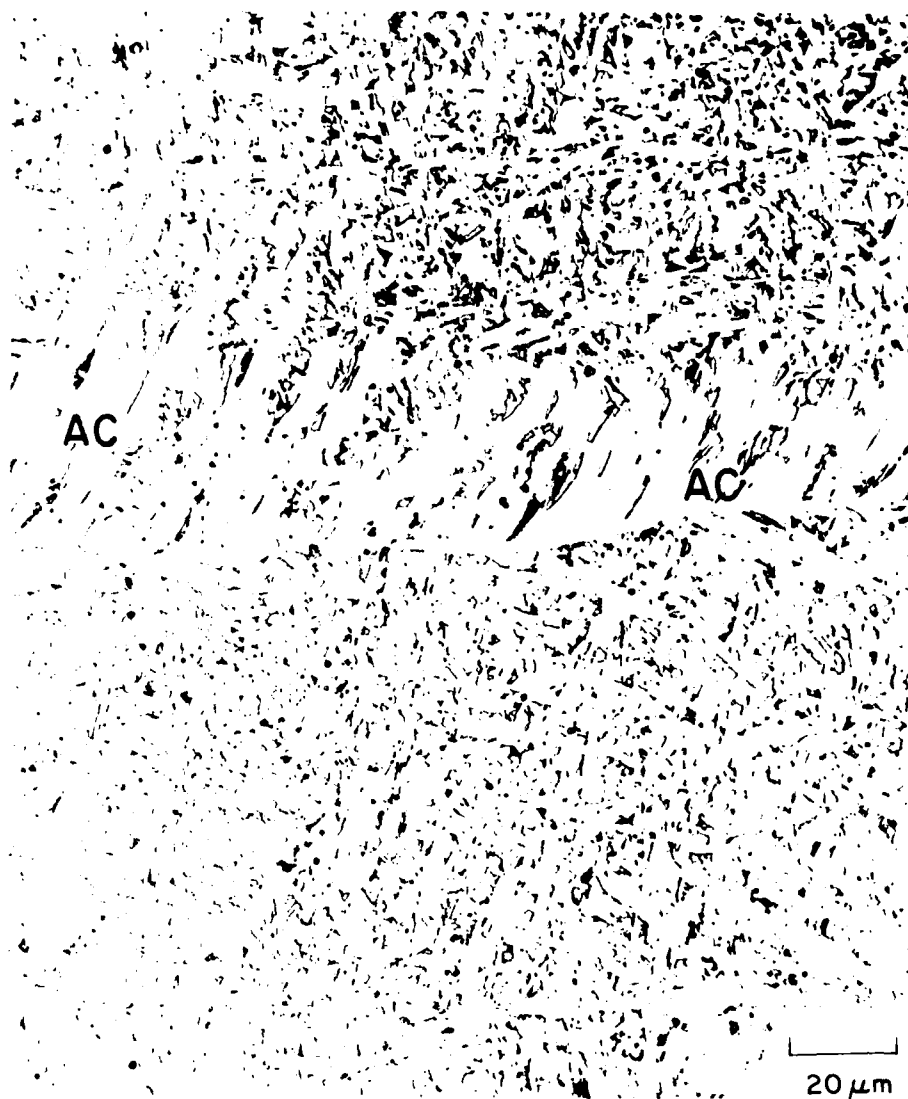


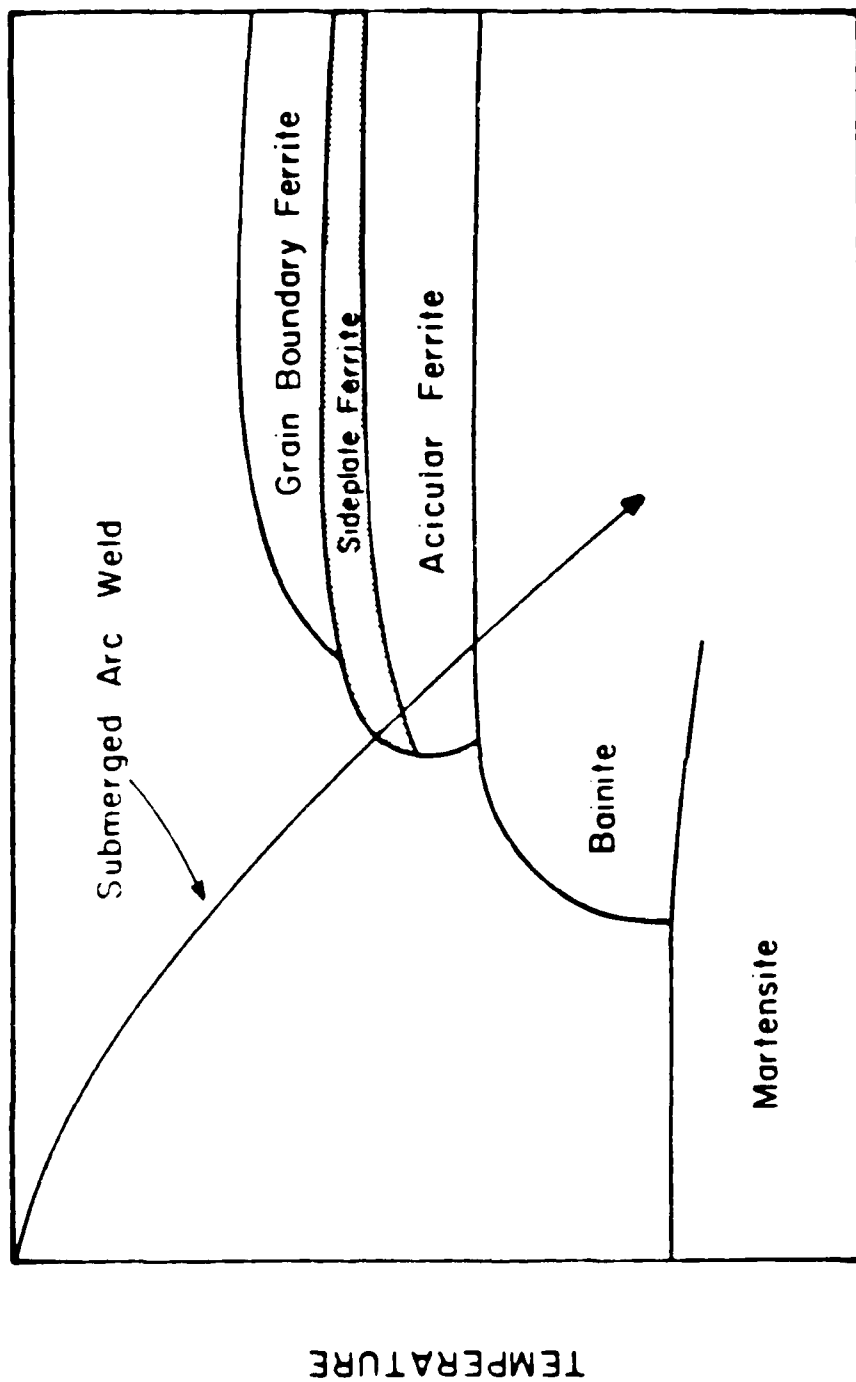
Figure 4. Example of weld metal ferrite with aligned second phase (AC) found in microalloyed HSLA steels. (2% nital etch) 750x.

fine interlocking ferrite laths of high acicularity, such as shown in Figure 5. The fine interlocking structure provides high resistance to cleavage initiation and propagation. Acicular ferrite heterogeneously nucleates intragranularly on non-metallic inclusions (1,15,39,45-46) and grows until impingement. The maximum lath size is governed by the mean spacing of nuclei. Therefore, a fine distribution of intragranular non-metallic inclusions results in fine intragranular laths (15). Observations by the electron microscope (46) have shown that the acicular ferrite laths have high angle boundaries with high dislocation substructures. The acicular ferrite formation start temperature is higher than that of bainite and martensite formation, but is slightly lower than that of grain boundary ferrite or sideplate ferrite, as shown in Figure 6.

4) Ferrite carbide aggregate (FC) is pearlite and ferrite with interphase carbides. Ferrite carbide aggregates, which are shown in Figure 7, need to be larger than the surrounding ferrite laths in order to be counted FC. The aggregates occur because excess carbon is rejected out of the ferrite into the austenite. The pools of carbon-enriched austenite trapped between ferrite laths then transforms during further cooling to FC, bainite, or even



Figure 5. Example of weld metal acicular ferrite (AF) found in microalloyed HSLA steels. (2% nital etch) 1500x.



LOG TIME

Figure 6. Schematic of continuous cooling transformation diagram of a microalloyed HSLA steel weldment showing the different microconstituent start temperatures.

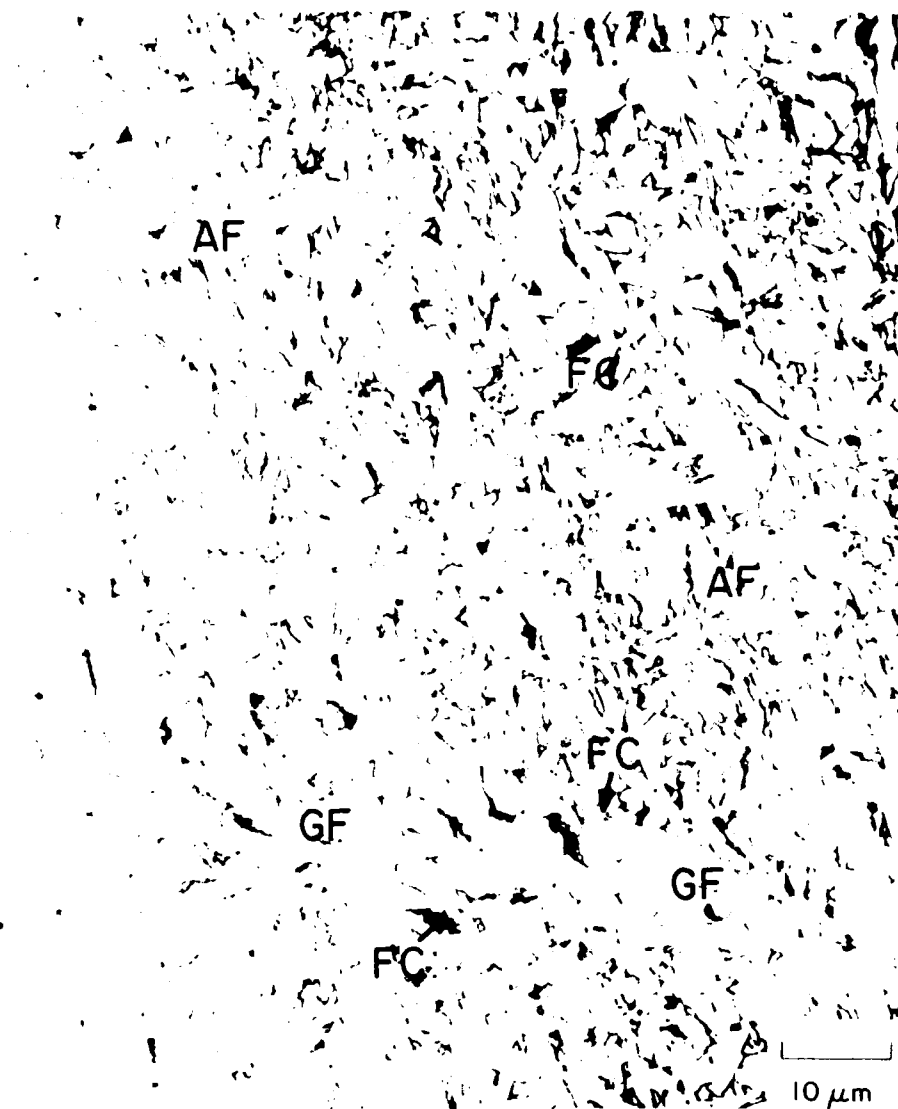


Figure 7. Examples of weld metal ferrite carbide (FC), grain boundary ferrite (GF), and acicular ferrite (AF) found in microalloyed HSLA steels. (2% nital etch) 1500x.

martensite.

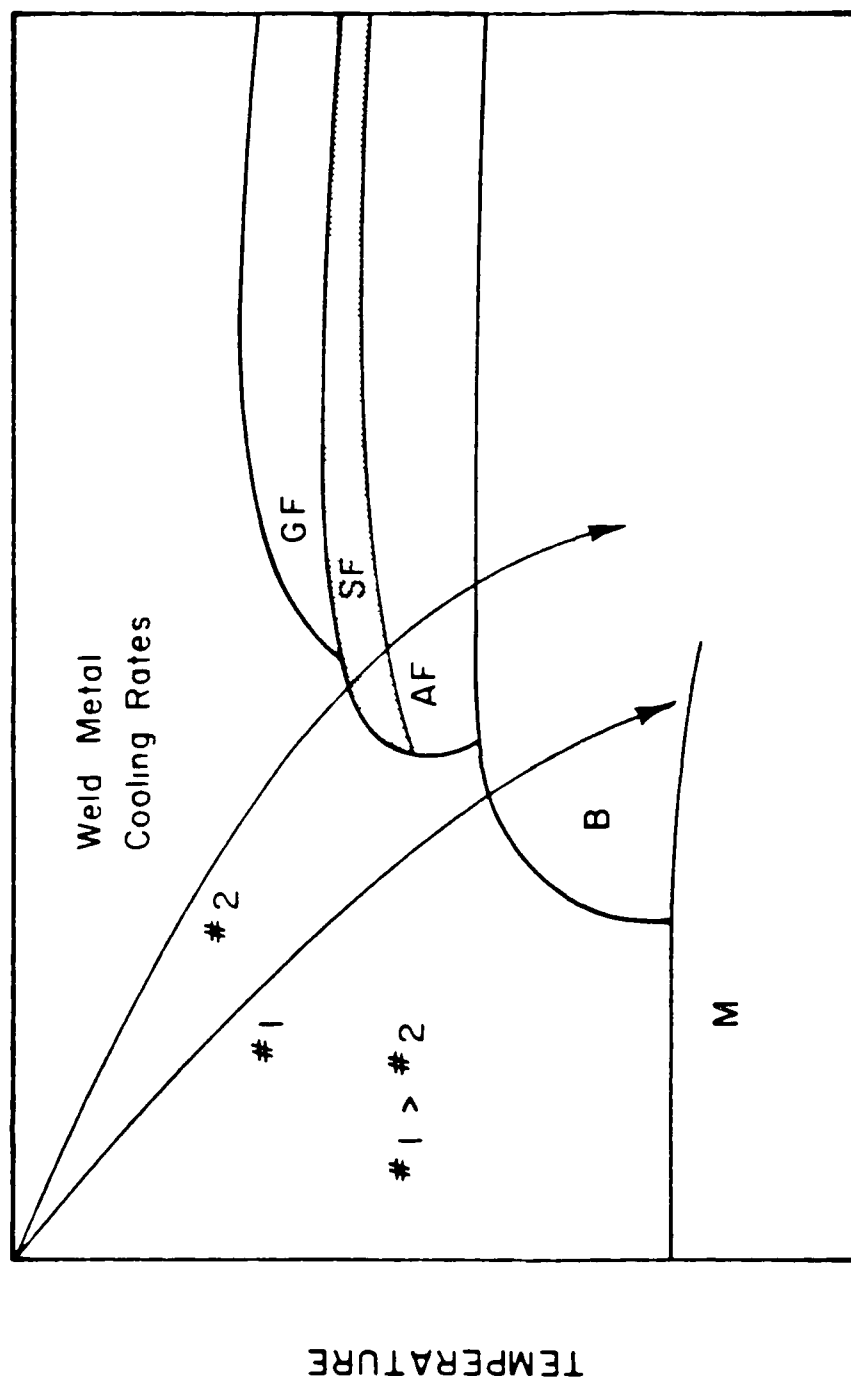
5.) Martensite (M) is formed when carbon-enriched retained austenite pools transform at large undercoolings. Small amounts of martensite have been reported to be very detrimental to weld metal properties (37).

1.4. FACTORS WHICH INFLUENCE THE WELD METAL MICROSTRUCTURE

The development of the microstructural constituents during the austenite decomposition in HSLA steel weld metal is very complex. The weld metal microstructure is mainly determined by the heat input and the weld metal composition. The inclusion content, which is a function of the weld metal composition, plays an important role in producing the weld metal microstructure.

1.4.1. Heat Input Effects

The influence of heat input or cooling rate on weld metal microstructure was studied by Glover (37). He showed that decreasing the heat input or increasing the cooling rate in low carbon steel will refine the weld metal microstructure from coarse primary ferrite to acicular ferrite, bainite, and eventually to martensite. Figure 8 is a schematic showing the effect of two different heat inputs on weld metal microstructural transformation. Figure 8 shows that an



LOG TIME

Figure 8. Schematic of continuous cooling transformation diagram of a microalloyed HSLA steel weldment showing the effect of two different cooling rates on weld metal microstructural transformation.

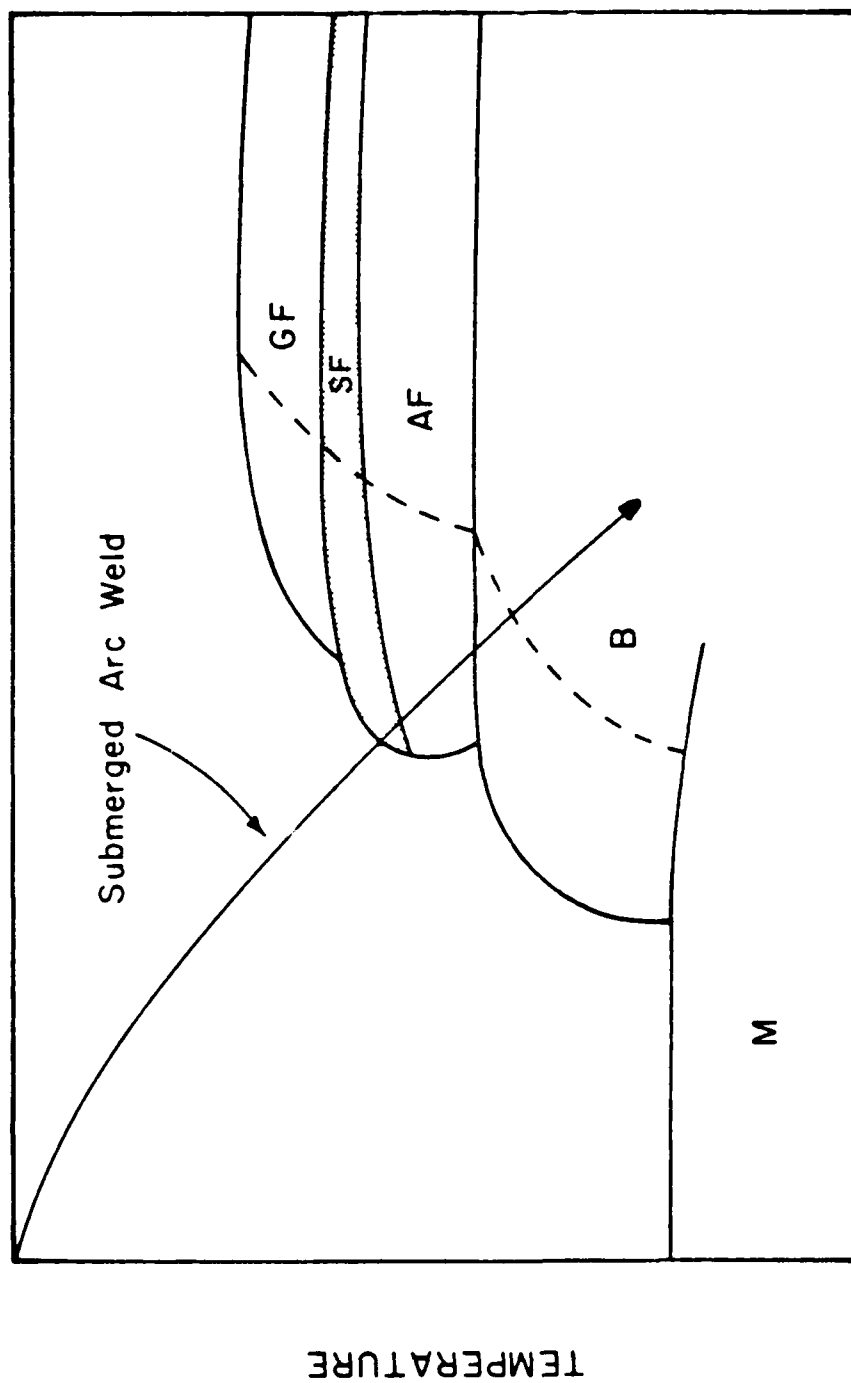
increased cooling rate will change the weld metal from a predominately acicular ferrite microstructure to one consisting primarily of bainite.

1.4.2. Weld Metal Composition Effects

The composition of the weld metal results from the alloying elements in the base plate, welding electrode, and the welding flux. The austenite decomposition transformations will shift to longer delay times when hardenability agents such as manganese, molybdenum, chromium, and boron are added. Figure 9 summarizes the effect of hardenability changes on weld metal transformation, and shows the importance of compositional control to produce the desired microstructure.

Carbon is the strongest hardenability agent, and is usually selected at the lowest possible level for the purpose of high fracture toughness and good weldability of HSLA steels. Small amounts of carbon can cause grain refinement, which will result in lowering the austenite-ferrite transformation temperature, if combined with strong carbide formers, such as niobium, vanadium, and zirconium. However, excess carbon usually tends to form large cementite particles which provide crack nucleation sites.

Manganese, which is a strong hardenability agent, will



LOG TIME

Figure 9. Schematic of continuous cooling transformation diagram of a microalloyed HSLA steel weldment showing the effects of hardenability on weld metal microstructural transformation.

strengthen the material by grain refinement and solid solution hardening. Manganese additions from 0.6 to 1.8 weight percent were shown by Evans (47) to refine and increase the amount of acicular ferrite in the weld metal and decrease the amount of primary ferrite. The explanation for this was that manganese both delays the ferrite-pearlite transformation and depresses the bainitic transformation temperature, forming fine-grained acicular ferrite. Evans' study also indicated that there is an specific amount of manganese to have in the weld deposit, (in his case it was 1.5 weight percent), which will produce optimal impact properties.

Molybdenum is another element that has a strong effect on hardenability (16). Molybdenum kinetically retards the austenite to ferrite transformation, which will lower the transformation temperature and cause a reduction in grain size. It also suppresses the pearlite formation, giving rise to acicular ferrite, bainite, and martensite. Molybdenum acts in conjunction with manganese to produce fine-grained acicular ferrite rather than coarse-grained primary ferrite. Too much molybdenum in the weld metal will produce a bainitic microstructure and/or undesirable molybdenum carbides, both which will reduce the toughness.

Niobium has been observed to decrease the amount of

acicular ferrite in the weld metal in some studies (32,48), but in others (16,32,49-51) an increase is reported. Invariably, additions of niobium reduced the amount of grain boundary ferrite. Increases in niobium have shown to increase the dislocation density (51-52), and precipitation has been reported in the as-welded plus reheat conditions (51-53). Niobium has been shown (32-33,53) to combine with carbon and/or nitrogen to form a fine dispersion of carbides, nitrides, or carbonitrides, in the austenite, thus retarding grain growth and recrystallization. At moderate levels of niobium of around 0.07 weight percent, molybdenum when used in combination with niobium will increase the toughness of the weld metal. However, at lower niobium levels, molybdenum does not effect the toughness.

Vanadium has been observed to promote acicular ferrite (49,54-56) for levels up to 0.1 weight percent in the absence of other elements, e.g. molybdenum (55). However, two studies have shown a decrease in ferrite with aligned carbide (48,54), while another study has observed an increase in ferrite with aligned carbide (57). Vanadium carbonitrides have been observed (52,58) and behave the same way as niobium carbonitrides, acting as grain growth and recrystallization inhibitors only at lower temperatures.

The effects of low levels of niobium (<0.02%) and

vanadium (<0.05%) have been summarized by Dolby (59). The effects of niobium and vanadium on weld metal microstructure and properties can differ if the cooling rate differs or if there are changes in alloy additions. In particular, at these low niobium and vanadium levels, observations show that:

- 1) an increase in Charpy V-Notch transition temperature occurs when $\Delta t_{800-500} < 50$ seconds, Mn < 1.1%, and there are no other deliberate alloy additions.
- 2) little change or some improvement in Charpy V-Notch transition temperature occurs when $\Delta t_{800-500} < 50$ seconds, Mn > 1.1%, or alloying with Mo, Ni, or Ti-B is present.
- 3) an increase in Charpy V-Notch transition temperature occurs when $\Delta t_{800-500} > 50$ seconds, Mn < 1.4%, and there are no other deliberate alloy additions.
- 4) an increase in Charpy V-Notch transition temperature occurs when Nb and V are added to multipass deposits from the wire, electrode coating, or the flux.

Titanium is an important element for improving weld metal toughness. Titanium can combine with oxygen to form titanium oxides (TiO) which promote intragranular nucleation of acicular ferrite (14,42). This has been reported to be related to a favorable crystallographic orientation between the nucleating agent and the nucleated ferrite. Titanium nitride particles (TiN) have also been shown to promote the formation of acicular ferrite (39).

Titanium is commonly added with boron. The rationale for the dual benefit is that the titanium nitride precipitates reduce the amount of free nitrogen in the weld metal, thus preventing boron nitride (BN) formation and allowing boron to segregate easily into prior austenite grain boundaries (14,42,60-61). The solute boron segregated at the austenite boundaries seems to suppress the nucleation of primary ferrite by a mechanism not yet clearly understood. Relatively low amounts of titanium (<0.02 weight percent) and boron (<0.005 weight percent), are typically added to microalloyed steel weld metal. The optimal values determined by other researchers are summarized in Table II (57,62-67). Titanium and boron contents depend on both other alloying elements and on the welding parameters of the submerged arc welding process.

Table II. Summary of the Optimal Amounts of Ti-B Addition Upon Submerged Arc Weld Metals (62)

Authors	Ti(%)	B(%)	Source		Ref
			Ti	B	
Shinmyo et al	0.02	0.0045	Flux (oxide)	Flux (oxide)	63
Hirabayashi et al	0.025 0.03	0.002	Wire	Wire	64
Shiga et al	<0.005	0.008 0.012	Wire	Flux	65
Ito et al	0.03 (Mo:0.2-0.35)	-	Wire	-	66
Garland et al	0.015	0.0005	Wire	Wire	57

The optimal ranges for titanium and boron within limits of other elements were determined by Masumoto (68) as follows:

Ti = 0.01 - 0.05% (< 0.03% preferred)

B = 0.001 - 0.003%

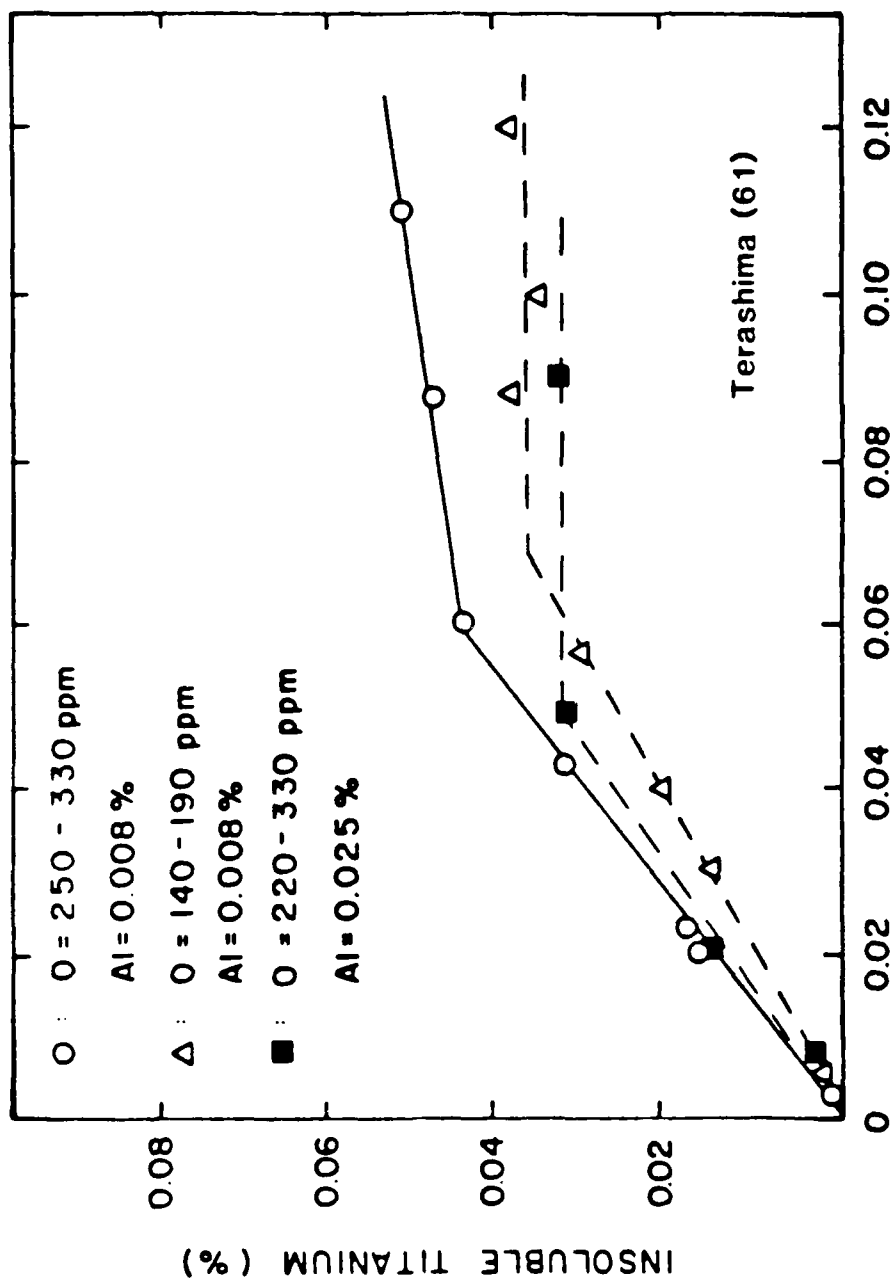
Mo = 0.15 - 0.35%

Nb < 0.025%

V < 0.035%

Al < 0.026% (< 0.015% preferred)

The amount of weld metal oxygen content seems to play an important role in determining the proper titanium and boron values. It has been shown by Terashima (61) that the optimal titanium content shifts to lower levels with decreasing weld metal oxygen content. Figures 10 and 11, which were taken from this paper, show that a decrease in oxygen or an addition of aluminum leads to a decrease in insoluble titanium and an increase in insoluble nitrogen. This suggests that, with decreasing oxygen in the weld metal, titanium fixes nitrogen more effectively because the insoluble titanium mainly exists as an oxide or nitride. Aluminum was shown to combine with oxygen in preference to titanium, allowing the free titanium to combine with nitrogen (61). Watanabe (69) showed that, in MIG welding,



TITANIUM CONTENT IN WELD METAL (%)

Figure 10. Relationship between total titanium and insoluble titanium in microalloyed steel weld metal containing different amounts of aluminum and oxygen (61).

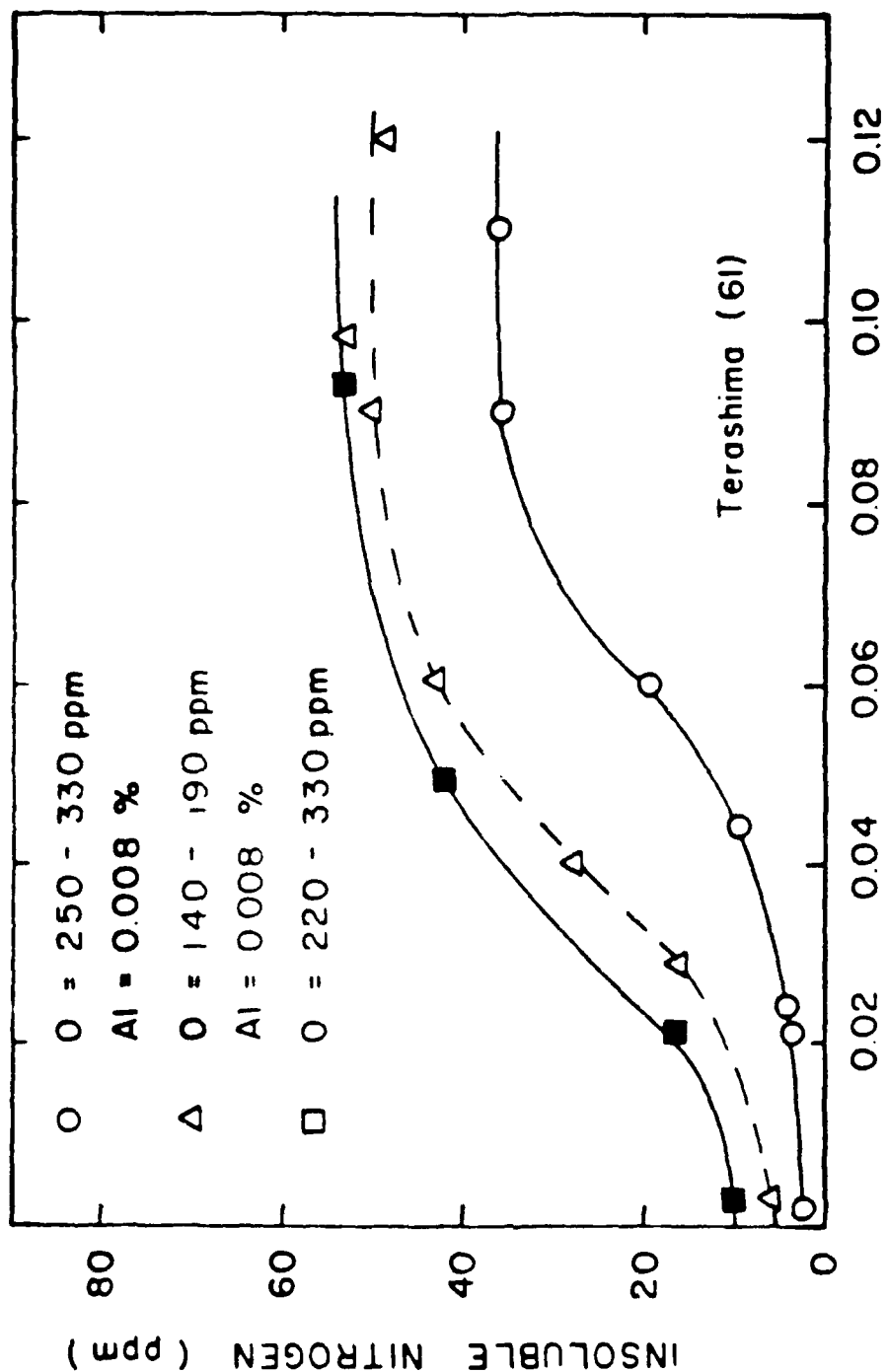


Figure 11. Relationship between total titanium and insoluble nitrogen in microalloyed steel weld metal containing different amounts of aluminum and oxygen (61).

insoluble boron as well as insoluble titanium increased with increasing weld metal oxygen. Koukabi (70) showed that, in low oxygen (<200ppm) submerged arc weldments, the toughness of the titanium bearing weldments was superior to the toughness of titanium-boron bearing weldments. The austenite to ferrite transformation temperature was shown to increase in titanium-boron weldments with increases in weld metal oxygen (71).

1.4.3. Weld Metal Inclusion Effects

Cochrane and Kirkwood (72), in dilatometric CCT studies, have shown oxygen to have a major effect on the transformation behavior of low-carbon austenite. High-oxygen weld metals began transforming at temperatures considerably above those of lower oxygen deposits, and they also proceeded to completion more rapidly as compared to the low oxygen weld metals. In low-carbon (0.08 %), high-manganese (1.8 %) weld deposits, Garland and Kirkwood (73) observed the formation of acicular ferrite using basic submerged arc welding fluxes with weld metal oxygen levels below 0.03 weight percent. However, a bainitic microstructure was obtained by using acidic fluxes which gave oxygen levels of 0.07 to 0.1 weight percent. The weld metal transformation behavior was explained (1,73-74) to be

influenced not by the effect of oxygen in solution but by the oxygen as it affects the number of small inclusions available as potential nucleation sites for transformation products during continuous cooling.

Researchers (75-76) have found that the inclusion shape and composition changes with the flux, and that different inclusions may nucleate different microstructures. This could be attributed to the inclusion/matrix interfacial energy, which would change with differences in composition of the inclusion. Pargeter (76) showed an association between inclusion type and microstructural constituents. Specifically, he found that inclusions containing manganese and silicon, with or without sulfur, were associated with coarse grain boundary ferrite and ferrite with aligned carbide, as indicated in Figure 12a. Aluminum-bearing inclusions seemed to be associated with acicular ferrite, Figure 12b. Thus it seems that weld metal oxygen is only indirectly related to the formation of a specific ferrite microstructure, but the density and size distribution of the inclusions appears to play an important role in the nucleation process of ferrite.

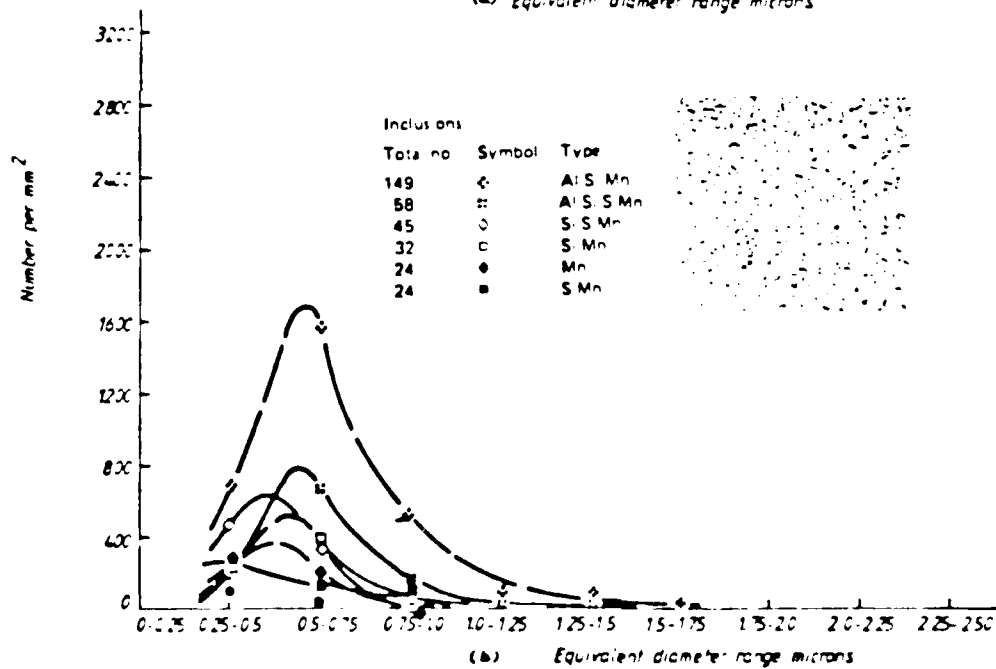
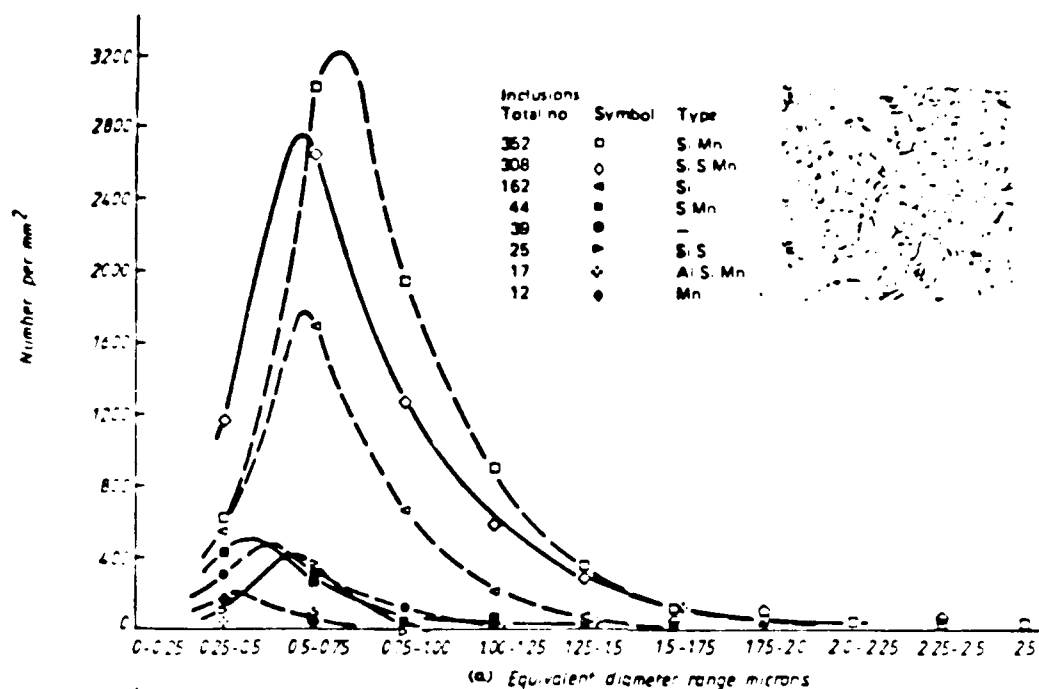


Figure 12. Inclusion size distribution and type for (76)
 a. coarse grain boundary ferrite
 b. acicular ferrite

II. MATERIALS AND EXPERIMENTAL PROCEDURE

II.1. FLUX PREPARATION

The four fluxes used in this study included one agglomerated commercial flux and three experimental fused fluxes. Compositions of these fluxes are given in Table III. The commercial flux, OP121TT, is a high MgO - CaF_2 - low SiO_2 flux made by Oerlikon. This flux will be designated "OP" throughout this report. The experimental fluxes include a 15% SiO_2 -50% MgO -35% CaF_2 flux designated "MgO", a 20% SiO_2 -50% CaO -30% CaF_2 flux designated "CaO", and a 40% SiO_2 -40% CaO -20% CaF_2 flux designated " SiO_2 ". The "MgO" and "CaO" fluxes are essentially equivalent, except that one contained 50% MgO while the other contained 50% CaO . These fluxes were designed to evaluate the potential differences between CaO and MgO additions. The fused fluxes were made using reagent grade chemicals which were mixed, then melted in a graphite crucible heated by a induction furnace and protected by a nitrogen cover gas. The furnace temperature was raised to at least 1550°C , then the crucible was removed, and the molten flux was poured into water at ambient temperature. The rapid quench caused the flux to break up into fine, very brittle sponge-like pieces. The flux was then dried under a heat lamp, and baked in a air-

TABLE III. Summary of Flux Compositions, in Weight Percent

<u>Flux</u>	<u>SiO₂</u>	<u>Al₂O₃</u>	<u>MgO</u>	<u>CaO</u>	<u>CaF₂</u>	<u>MnO</u>	<u>TiO₂</u>	<u>Na₂O</u>	<u>Fe₂O₃</u>
OP	10.7	17.3	31.7	6.6	24.1	1.1	0.86	0.78	1.9
MgO	15.0	--	50.0	--	35.0	--	--	--	--
CaO	20.0	--	--	50.0	30.0	--	--	--	--
SiO ₂	40.0	--	--	40.0	20.0	--	--	--	--

blowing furnace at approximately 800°C to remove water and excess carbon (introduced from the graphite crucibles during melting). The flux was crushed to a size that screened in the range from 14 to 100 mesh. The flux was introduced to the weld during the welding operation by means of a standard flux bin.

11.2. WIRE PREPARATION

Two 3/32-in. diameter filler wires were used in this study. These wires were: 1) TiBor 22, a commercial microalloyed steel wire made by Oerlikon and containing additions of boron and titanium (herein designated "TB"), and 2) a research heat with the same base composition as TiBor 22, but without boron, titanium, or molybdenum. This experimental wire, designated "CSM", was produced by shearing strips from a 1/8-in. thick plate, which were then swaged to final dimensions and cleaned in a 60% hydrochloric acid solution. The wire compositions are found in Table IV. The other two filler metal compositions mentioned in Table IV resulted when a pure molybdenum strip was added to a weld made with "CSM" wire (designated "CSM + Mo"), or when a pure molybdenum strip and a pure titanium strip were added to a weld made with "CSM" wire (designated "CSM + (Ti/Mo)").

Table IV. Summary of Welding Wire Composition, in Weight Percent.

Wire	C	Mn	P	S	Si	Cr	Ni	Mo	B	Nb	Cu	Ti	Al	O	N
TB	0.059	1.48	0.008	0.009	0.04	0.12	0.10	0.26	0.010	0.003	0.77	0.030	0.028	0.006	0.007
CSM	0.059	1.38	0.021	0.018	0.02	0.01	0.04	0.01	0.002	0.004	0.10	0.000	0.026	0.020	0.005
(CSM+ Mo)	0.059	1.38	0.021	0.018	0.02	0.01	0.04	0.67	0.002	0.004	0.10	0.000	0.026	0.020	0.005
(CSM+ Ti/Mo)	0.059	1.38	0.021	0.018	0.02	0.01	0.04	0.26	0.002	0.004	0.10	0.030	0.026	0.020	0.005

II.3. WELDING OPERATION

At the beginning of this investigation, welds were made of Lukens Steel Company's quenched and tempered 3/4-in.-thick C-Mn-Mo-Nb steel plate using a commercial wire (Tibor-22), and flux (OP-121TT). The composition of the baseplate is shown in Table V. The welding consumables are well known to produce fine acicular ferrite weld metal and thus, optimal weld metal properties. By using the commercial product weld as the basis for this investigation, and by keeping the heat input at 75 kJ/in (3.0 kJ/mm), and the deposition ratio of wire speed to travel speed constant at 13, a systematic variation of submerged arc welds were produced to investigate the influence of certain microalloying elements and flux variations in determining the quality of microalloyed steel weld metal. The welding parameters are given in Table VI, and their resulting compositions are given in Table V. Note that welds TB-OP* and CSM-OP* are duplications of welds TB-OP and CSM-OP respectively.

II.4. METALLOGRAPHY

The welds were sectioned transverse to the welding direction in at least three different areas. These areas were then examined both macroscopically and microscopically.

Table V. Summary of Baseplate and Weld Metal Compositions, in Weight Percent

Weld	C	Mn	P	S	Si	Cr	Ni	Mo	B	Nb	Cu	Ti	Al	O	H
TB- OP	0.080	1.52	0.012	0.007	0.17	0.12	0.12	0.25	0.0018	0.021	0.21	0.0041	0.024	0.027	0.010
TB- OP*	0.080	1.50	0.012	0.007	0.16	0.13	0.12	0.25	0.0015	0.020	0.31	0.0045	0.029	0.026	0.010
TB- CaO	0.083	1.53	0.012	0.008	0.17	0.13	0.12	0.25	0.0015	0.017	0.31	0.0039	0.024	0.012	0.009
TB- MgO	0.080	1.48	0.011	0.007	0.16	0.12	0.11	0.25	0.0018	0.019	0.34	0.0048	0.019	0.018	0.009
TB- SiO ₂	0.068	1.15	0.012	0.009	0.35	0.12	0.12	0.26	0.0011	0.017	0.36	0.0041	0.018	0.051	0.010
(CSM +Ti/Mo)- OP	0.080	1.50	0.014	0.011	0.15	0.10	0.10	0.25	0.0008	0.021	0.11	0.0030	0.038	0.032	0.009
(CSM+Mo)- OP	0.075	1.40	0.016	0.010	0.14	0.09	0.09	0.43	0.0003	0.018	0.10	0.0001	0.021	0.028	0.010
CSM- OP	0.078	1.46	0.015	0.009	0.15	0.09	0.10	0.13	0.0005	0.019	0.10	0.0001	0.024	0.042	0.008
CSM- OP*	0.078	1.49	0.015	0.009	0.15	0.10	0.10	0.12	0.0003	0.019	0.10	0.0001	0.026	0.041	0.009
Baseplate	0.093	1.57	0.013	0.010	0.20	0.12	0.12	0.26	0.0008	0.033	0.11	0.0001	0.024	0.009	0.011

Table VI. Summary of Welding Parameters for Experimental Welds

Weld	Wire	Flux	Volts	Current (amps)	Wire Speed (mm/s)	Travel Speed (mm/s)	Heat Input (KJ/mm)
TB- OP	TB	OP	29.5	530	66.5	5.2	3.00
TB- OP*	TB	OP	30.0	510	66.5	5.2	2.94
TB- CaO	TB	CaO	34.5	440	66.5	5.2	2.91
TB- MgO	TB	MgO	31.0	510	66.5	5.2	3.04
TB- SiO ₂	TB	SiO ₂	33.0	480	66.5	5.2	3.04
(CSM + Ti/Mo) - OP	CSM+Ti/Mo	OP	32.0	480	66.5	5.2	2.95
(CSM+Mo) - OP	CSM+Mo	OP	34.0	460	66.5	5.2	3.00
CSM- OP	CSM	OP	29.0	540	66.5	5.2	3.01
CSM- OP*	CSM	OP	30	505	66.5	5.2	2.91

For macroscopic examination, the welds were ground, polished, and etched with a solution of 85 volume percent water, 15 volume percent nitric acid, and 5 volume percent methanol. The samples were then photographed at the same magnification, 4X, in order to easily calculate the bead area, depth of penetration, and dilution of each weld. These data are summarized in Appendix A.

The weld samples were then repolished and etched with a 2 volume percent nital solution and analyzed on the metallograph. Since the microstructure of each weld was relatively constant throughout, the micrographs shown in this study were taken from the centerline of each weld bead as viewed parallel to the welding direction. Standard quantitative metallographic techniques were used to evaluate the volume fraction of the various microconstituents and the acicular ferrite lath size (77). The volume fraction of the microconstituents was calculated from over 800 point counts at 500X and 1000X using the guidelines for classification by Abson and Dolby (30). The accuracy of point counting was determined using the technique described by Gladman and Woodhead (78). The mean lath size was determined using the linear intercept technique on micrographs taken at 1000X.

For the purpose of determining prior austenite grain size, the welds were sectioned perpendicular to the columnar

growth direction (shown schematically in Figure 13). Prior austenite grain diameters were then measured and averaged using the linear intercept technique. To etch out the grain boundaries, several etchants were tried, with the most successful being a 5 volume percent nital solution. The prior austenite grain size values are summarized in Appendix B. The accuracy of the prior austenite grain diameter calculations were determined by following ASTM standards (77).

II.5. CHEMICAL COMPOSITION

The carbon, sulfur, oxygen, and nitrogen content of the weld metal were analyzed using Leco interstitial analyzers. All of the remaining elements were analyzed using an ARL 34,000 Emission Spectrometer. The wire and the weld metal were analyzed at least three different times in three different areas and then averaged to give the compositions listed in Tables IV and V respectively.

Compositional differences, were calculated by subtracting the nominal value from the analytical value. Figure 14 shows a schematic of how the nominal composition was calculated. The nominal composition is equal to the wire composition multiplied by the weight of the deposited metal, plus the base plate composition multiplied by the

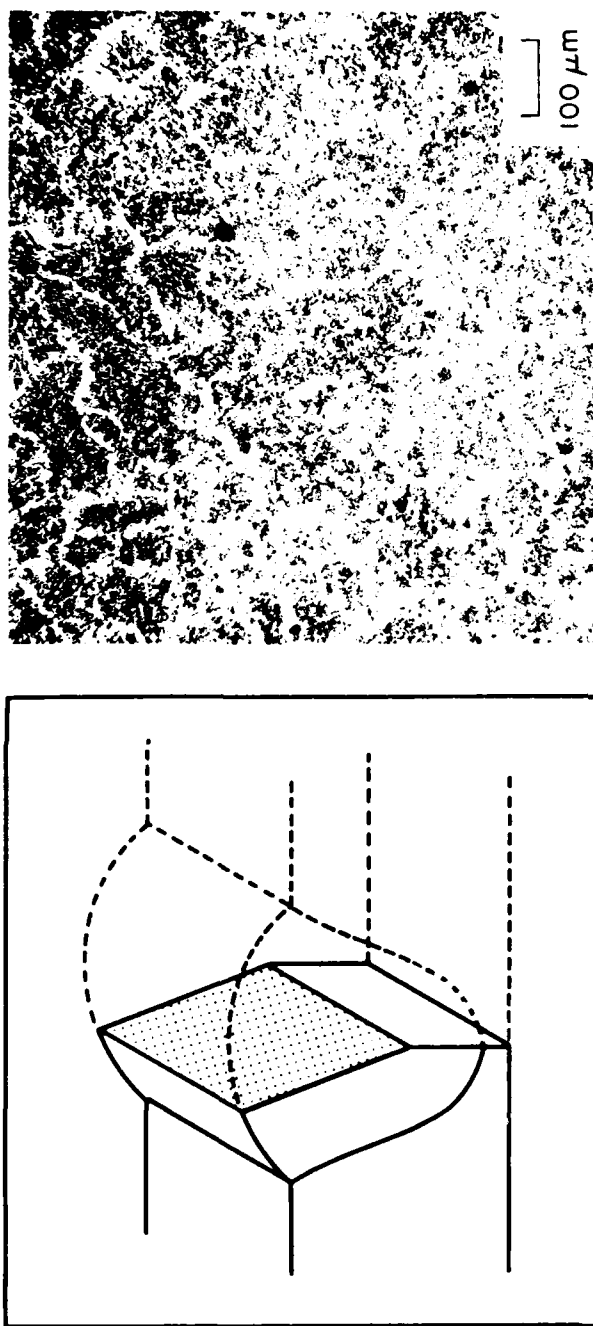
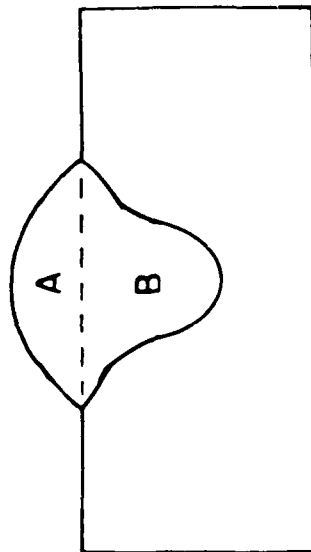


Figure 13. Schematic of a microalloyed HSLA steel weldment showing the section from which the prior austenite grain size was measured. Also included is a weld metal micrograph showing the prior austenite grain boundaries. (5% nital etch) 100x.



$$\text{Nominal Composition} = \frac{[A \times \{\text{Wire Composition}\}] + [B \times \{\text{Baseplate Composition}\}]}{A + B}$$

$$A + B$$

$$\text{Composition Difference} = \text{Analytical Value} - \text{Nominal Composition}$$

Figure 14. Schematic of a microalloyed HSLA steel weldment showing the calculation for compositional differences.

weight of the parent metal melted, all divided by the total weight of the fused metal. A negative compositional difference for a given element implies that a portion of that element was removed by the slag. In contrast, a positive compositional difference implies that the flux has rejected that element into the weld pool. The compositional differences for each weldment are summarized in Table VII.

II.6. HARDNESS

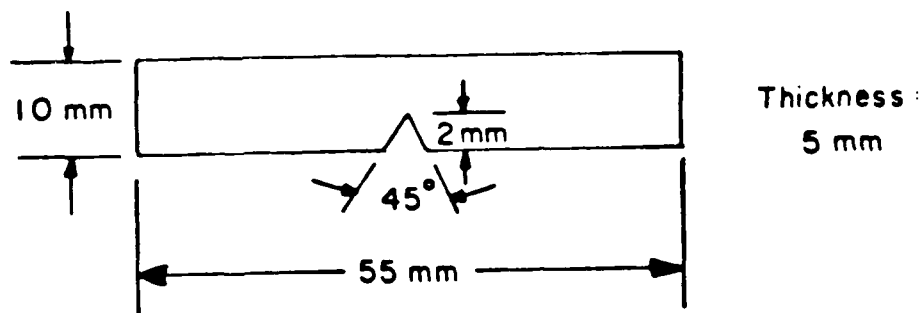
Weld metal hardness values were measured by using a Rockwell hardness tester. Measurements were taken from at least five different areas of the weld bead and then averaged. The values were then converted to the diamond pyramid hardness scale and are recorded in Appendix C. Microhardness values were also taken across the center of the weld bead. The average micro-hardness values are also given in Appendix C.

II.7. MECHANICAL TESTING

ASTM subsize (5.0 x 10.0 x 55.0 mm) Charpy specimens (79) were machined from welds TB-OP* and CSM-OP* as shown in Figure 15. Their impact energy results were measured at various temperatures using the Tinius Olsen

Table VII. Compositional Differences of the Weld Metal, in Weight Percent

Weld	ΔC	ΔMn	ΔP	ΔS	ΔSi	ΔCr	ΔNi	ΔMo	ΔB	ΔNb	ΔCu	ΔTi	ΔAl	ΔO	ΔN
TB															
OP	0.00	-0.01	+0.001	-0.003	+0.03	0.00	+0.01	0.00	-0.0026	0.00	-0.15	-0.0071	-0.02	+0.019	+0.001
TB															
CaO	+0.01	+0.00	+0.001	-0.002	+0.05	+0.01	0.00	-0.02	-0.0045	+0.01	-0.11	-0.0122	+0.01	+0.004	+0.001
TB															
MgO	0.00	-0.07	+0.000	-0.003	+0.03	-0.01	0.00	0.00	-0.0030	-0.01	-0.05	-0.0079	-0.02	+0.010	0.000
TB															
SiO ₂	-0.01	-0.39	+0.001	-0.001	+0.21	0.00	+0.01	0.00	-0.0033	-0.01	0.00	-0.0074	-0.03	+0.043	0.000
CSM + (Ti/Mo)															
OP	0.00	+0.01	-0.002	-0.002	+0.02	+0.02	+0.01	0.00	-0.0006	0.00	0.00	-0.0025	0.00	+0.019	0.000
CSM															
+ Mo															
OP	0.00	-0.08	0.000	-0.004	+0.03	+0.02	+0.01	0.00	-0.0012	0.00	-0.01	-0.0006	-0.02	+0.014	+0.002
CSM															
OP	0.00	-0.03	-0.001	-0.004	+0.03	+0.01	+0.01	0.00	-0.0009	0.00	0.00	-0.0003	-0.02	+0.028	0.000



ASTM Subsize Charpy Impact Tests Specimen Orientation

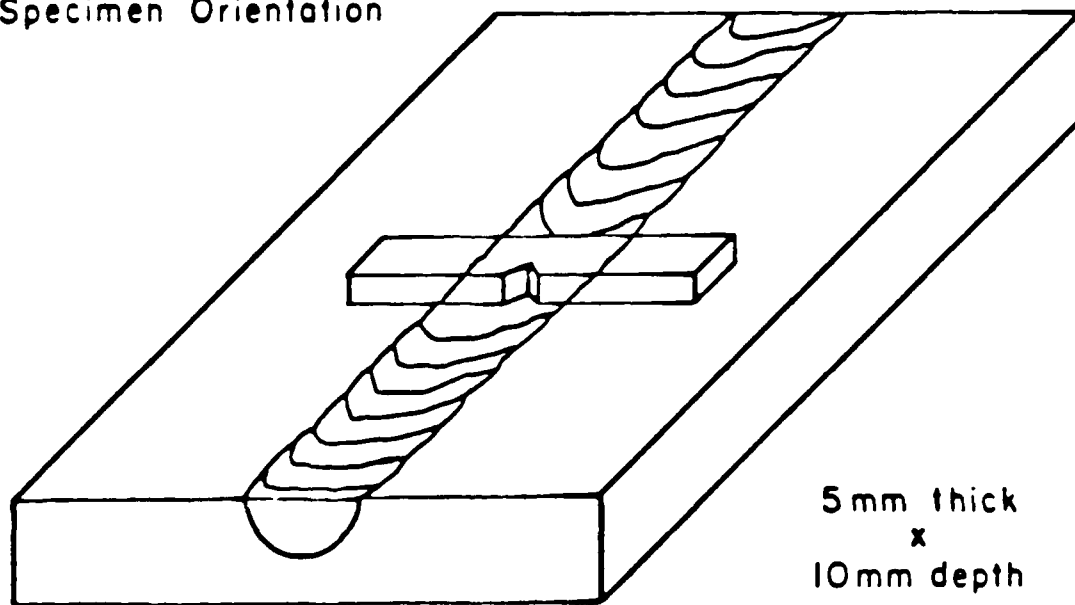


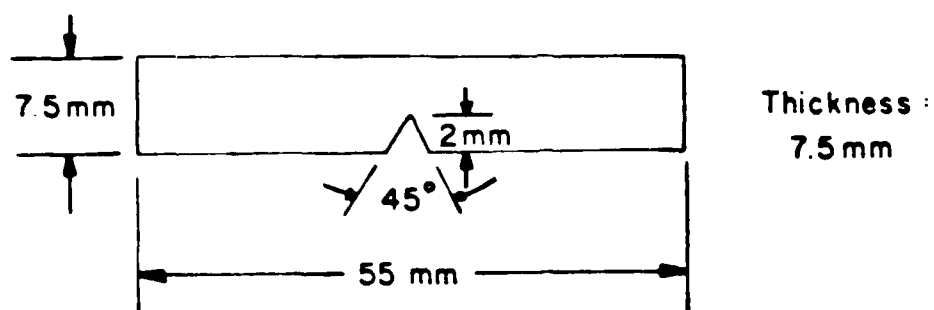
Figure 15. Schematic of a submerged arc weld showing the dimensions and orientation of subsize Charpy V-Notch specimens.

testing machine. Subsize (7.6 x 7.6 x 55.0 mm) Izod specimens were machined from all the weldments as shown in Figure 16. All these specimens were broken at -40°C with the Tinius Olsen testing machine. After both the Charpy and Izod bars had been broken, they were washed with methanol and stored in a dessicator. The fractured surface area was then examined by the naked eye to measure the percent shear fracture.

ASTM subsize (5.0 x 9.5 x 101.6 mm) tensile specimens (80), an example of which is shown in Figure 17, were also machined from welds TB-OP* and CSM-OP*. Tiny strain gauges were placed on the weld metal area of the specimen to record the weld metal yield strength.

11.8. ELECTRON MICROSCOPY

Weld metal fractographs of the Izod specimens were taken using the AMR scanning electron microscope. Since they were used to compare with the optical micrographs, the centerline fractographs were taken at 500X, 1000X and 2000X.



Subsize Izod Impact Test
Specimen Orientation

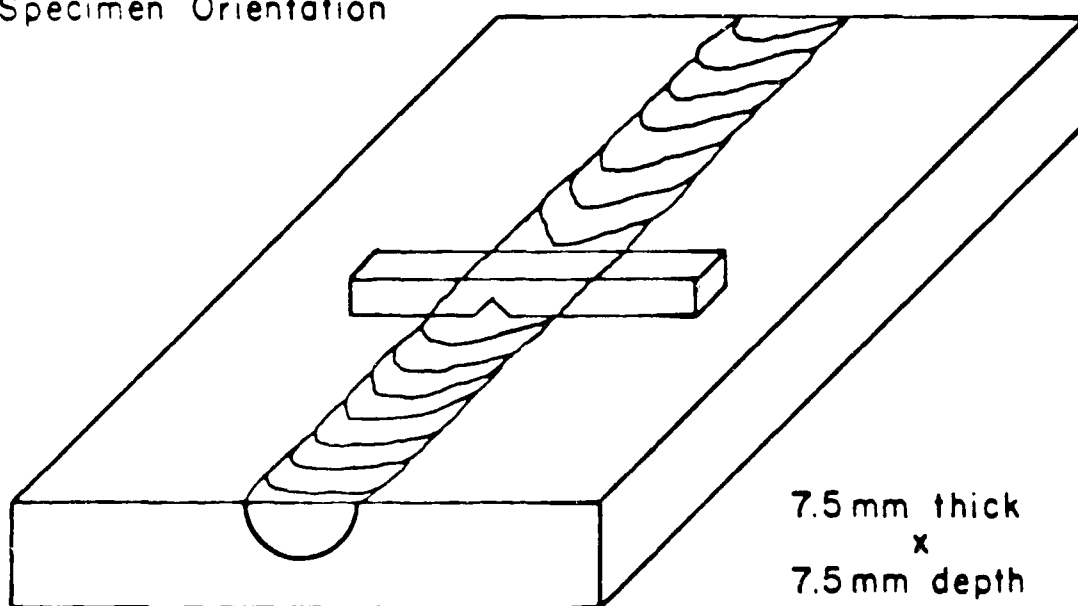
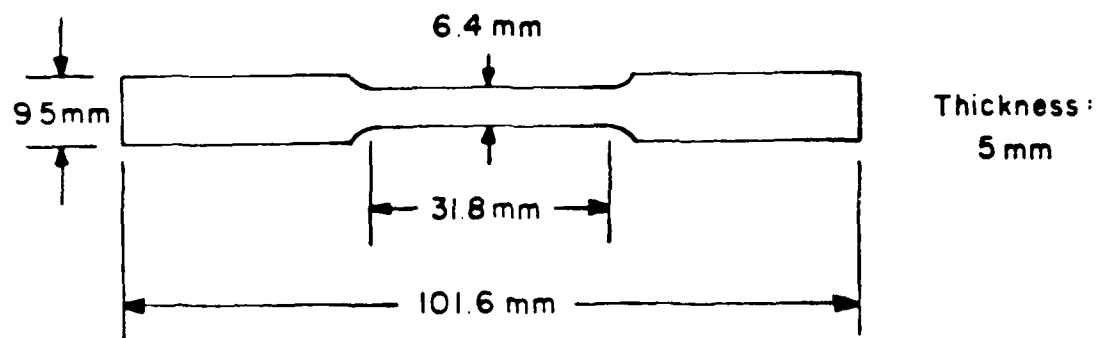


Figure 16. Schematic of a submerged arc weld showing the dimensions and orientation of subsize Izod specimens.



Subsize Tensile Test
Specimen Orientation

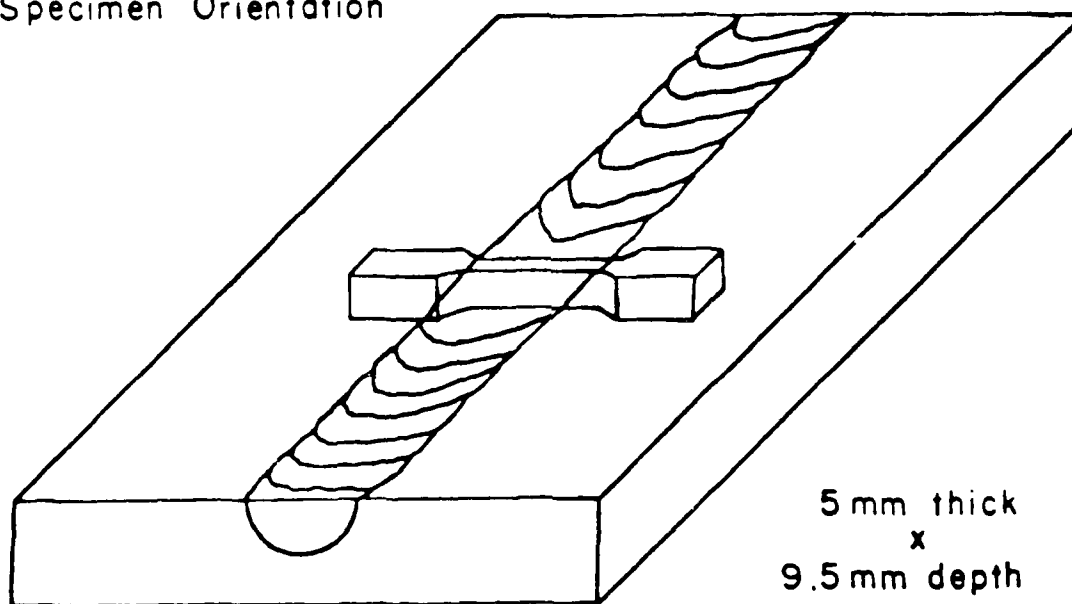


Figure 17. Schematic of a submerged arc weld showing the dimensions and orientation of tensile bar specimens.

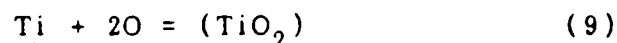
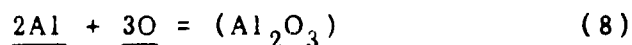
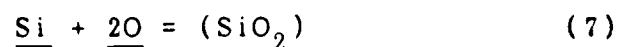
III. RESULTS AND DISCUSSION

III.1. WELDING OPERATION

Table V displays the systematic changes in the weld metal composition that were produced using the various wires and fluxes. Weld CSM-OP of course did not contain titanium or boron in the weld metal. The molybdenum content also dropped considerably (to 0.13 weight percent as compared to weld TB-OP which contained 0.25 weight percent) due to lack of molybdenum in the CSM filler metal. By adding molybdenum to the CSM wire to produce weld (CSM + Mo)-OP, then molybdenum plus titanium to produce weld (CSM + Ti/Mo)-OP, the effects of lone microalloying additions on weld metal microstructure and properties could be investigated.

By changing from the OP flux to the low oxygen potential CaO or MgO flux, the amount of oxygen in the weld metal was reduced considerably. Weld TB-SiO₂, which was produced by using a high oxygen potential silica flux, contained a weld metal oxygen content almost double that of the commercial weld TB-OP. Weld TB-SiO₂, when compared to weld TB-OP, also contained losses in carbon and manganese, as well as an increase in silicon. The compositional differences which are given in Table VII show a gain of 0.21 weight percent silicon and a loss of 0.39 weight percent

manganese in weld TB-SiO₂. Figure 18 displays a plot of the compositional changes of silicon and manganese versus the basicity index (given by Equation 4 on page 8). This graph shows that by increasing the basicity of the flux, the amount of silicon gained or manganese loss will become nil. One of the most important terms in the basicity index is the concentration of SiO₂. As already discussed on page 6, oxygen will be introduced into the weld pool during the high temperature stage due to a reduction of silica (Equation 1). Consequently upon cooling, the following competitive reactions between the various deoxidation elements present will take place:



This will lead, in the case of the high SiO₂ flux system, to an increase in the weld metal silicon content and a decrease in the manganese content, as indicated in Figure 18.

However, when welding is performed with fluxes containing lower amounts of silica, the oxygen picked up during welding will be low and hence, the oxidation loss of manganese will

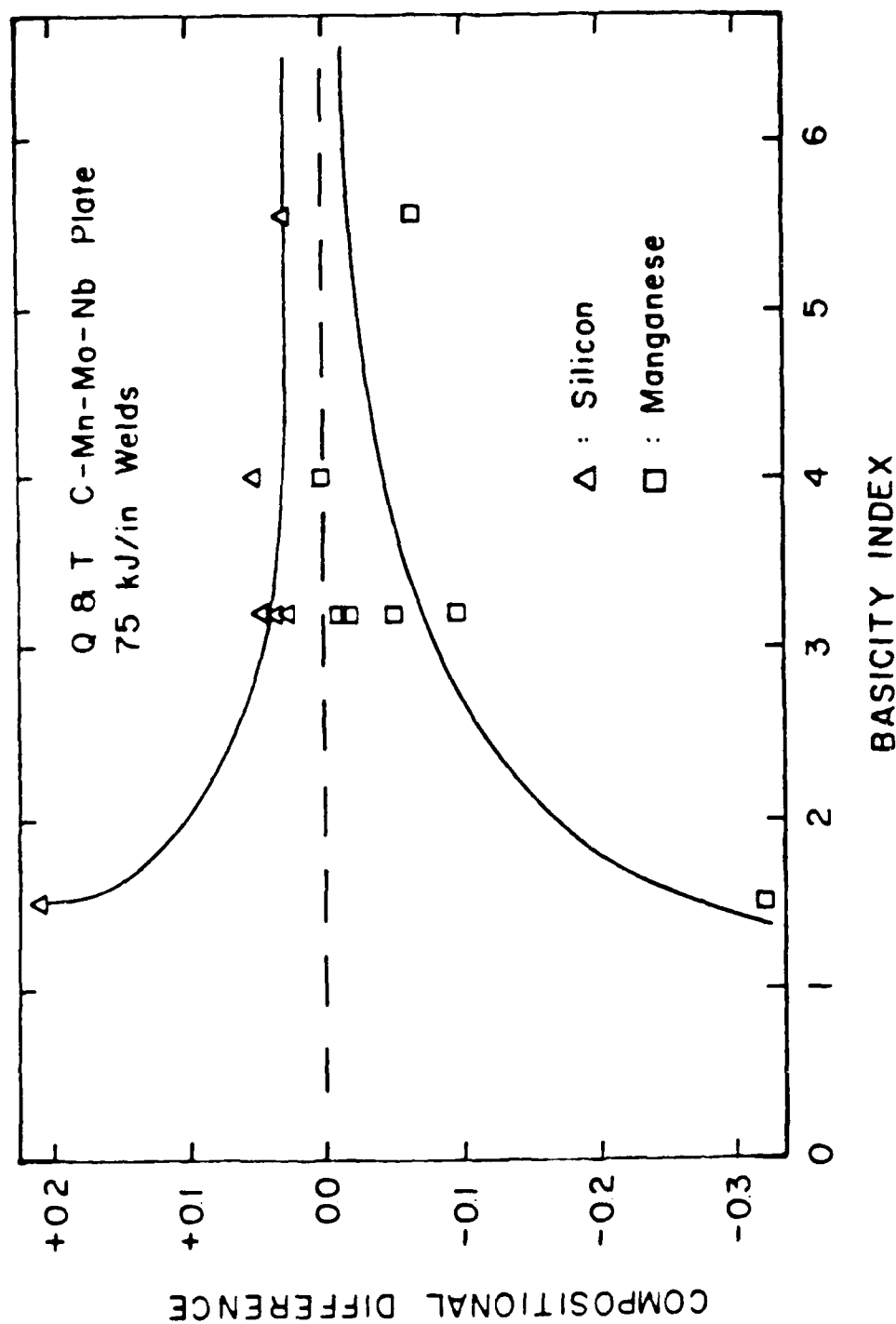


Figure 18. Relationship between flux basicity and compositional differences in silicon and manganese of submerged arc welds performed on quenched and tempered C-Mn-Mo-Nb plate.

also be small.

III.2. WELD METAL MICROSTRUCTURAL ANALYSIS

The resulting microstructures of the seven experimental weldments are presented at 500X in Figures 19a and 19b. The micrographs present the centerline microstructures of each weld bead as viewed parallel to the welding direction. The microstructures shown were found to be representative of the remainder of the bead. As shown in Figure 19a, a large volume fraction of fine acicular ferrite was produced in all of the experimental welds using the TiBor wire. In each of these four welds the remainder of the weld metal microstructure mainly consisted of primary ferrite (ranging from 11 percent in weld TB-OP to 29 percent in weld TB-SiO₂). The majority of the primary ferrite in these welds consisted of grain boundary ferrite, which ranged from 7 percent in weld TB-OP to 18 percent in weld TB-SiO₂.

Figure 19b shows the different weld metal microstructures produced by changing the wire. The micrographs show that by changing the wire from TB to CSM + Ti/Mo to CSM + Mo to CSM, the microstructure changes from almost entirely acicular ferrite to a structure consisting mainly of "AC" (which in more specific terms is bainite in these cases), with the remainder being made up of primary



TB-OP

20 μ 

TB-CaO

20 μ 

TB-MgO

20 μ TB-SiO₂20 μ

Figure 19a. Centerline microstructures of four experimental submerged arc welds made on quenched and tempered C-MN-Mo-Nb plate. Welding consumables for each weld are given in Tables III and IV. All welds were made at a heat input of 75 KJ/in and a deposition ratio of 13. (2% nital etch) 500x

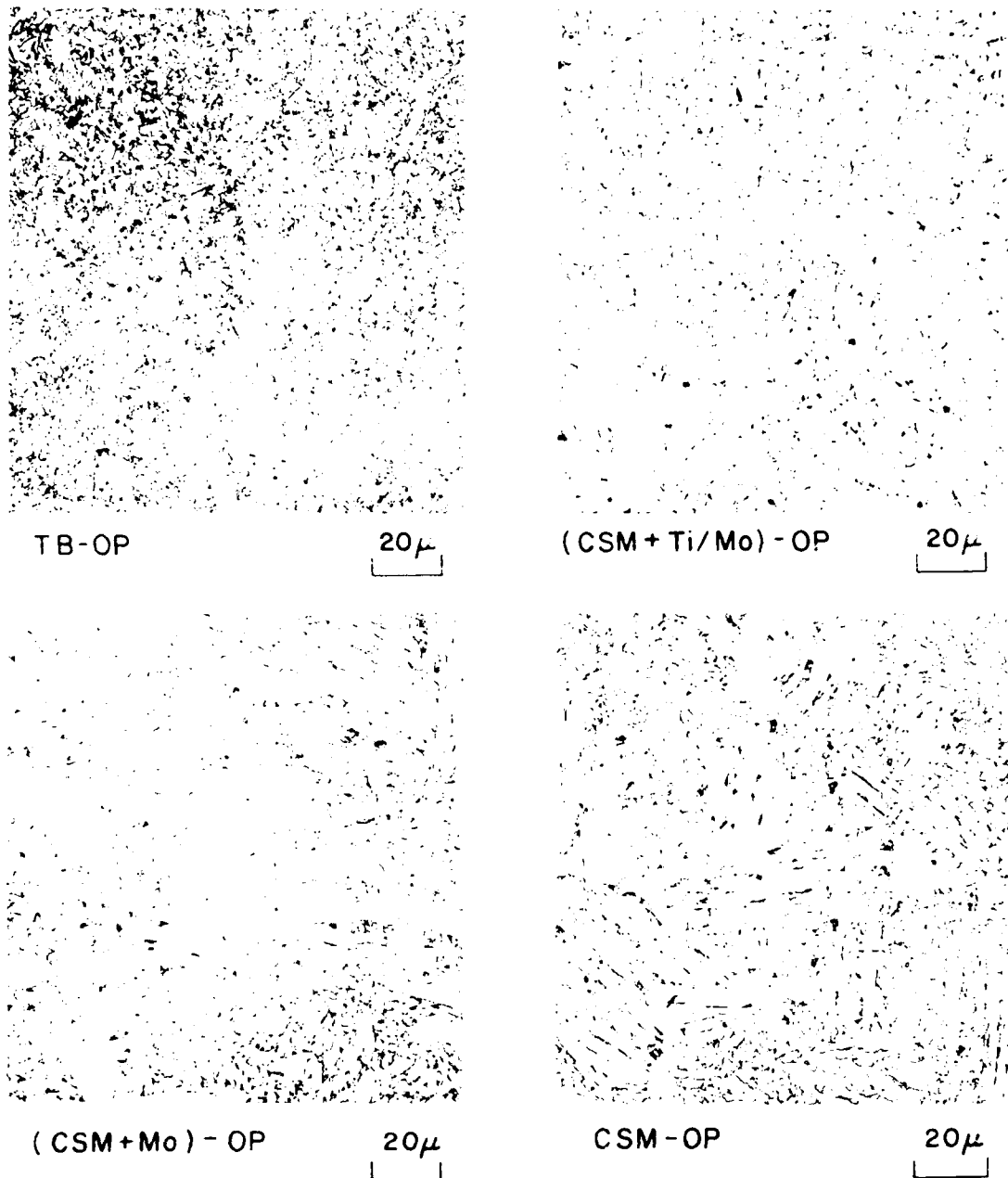


Figure 19b. Centerline microstructures of four experimental submerged arc welds made on quenched and tempered C-MN-Mo-Nb plate. Welding consumables for each weld are given in Tables III and IV. All welds were made at a heat input of 75 KJ/in and a deposition ratio of 13. (2% nital etch) 500x

and acicular ferrite.

The volume percent of the microconstituents and the acicular ferrite lath spacing are summarized for each weld in Figures 20 and 21 respectively. These figures substantiate the observations made from the micrographs in Figures 19a and 19b. The commercial product weld TB-OP contained the highest amount of acicular ferrite, approximately 85 percent, and the finest lath spacing of 1.4 microns. Weld TB-CaO produced 79 percent acicular ferrite, which was the second highest amount, and approximately the same acicular ferrite lath size as weld TB-OP. Weld TB-MgO contained 68 percent acicular ferrite followed by weld TB-SiO₂ with 63 percent. Their acicular ferrite lath sizes of 1.8 and 1.9 microns respectively were coarser than the two previous welds TB-OP and TB-CaO. The primary ferrite was found to increase in the weld as the flux changed from OP to CaO to MgO to SiO₂.

Weld CSM-OP, which was welded with a wire that did not contain molybdenum, titanium, or boron, exhibited the lowest amount of acicular ferrite, approximately 26 percent, and the coarsest microstructure. By adding molybdenum to the wire, weld (CSM + Mo)-OP produced little change to the volume percent of the microconstituents compared to weld CSM-OP, but did refine the acicular ferrite lath spacing

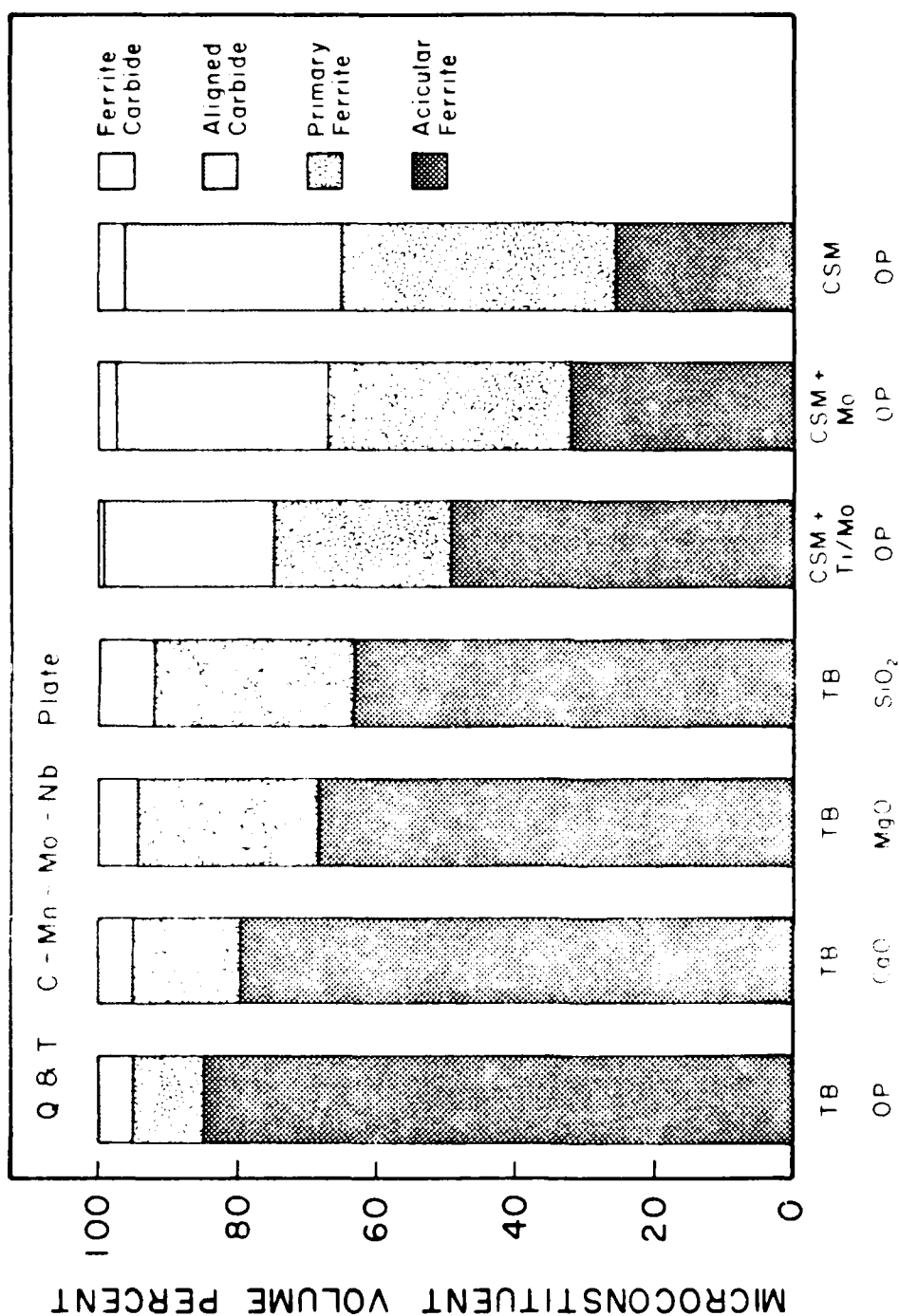


Figure 20. The volume percentages of microconstituents observed at the weld center line of seven experimental submerged arc welds performed on quenched and tempered C-Mn-Mo-Nb plate.

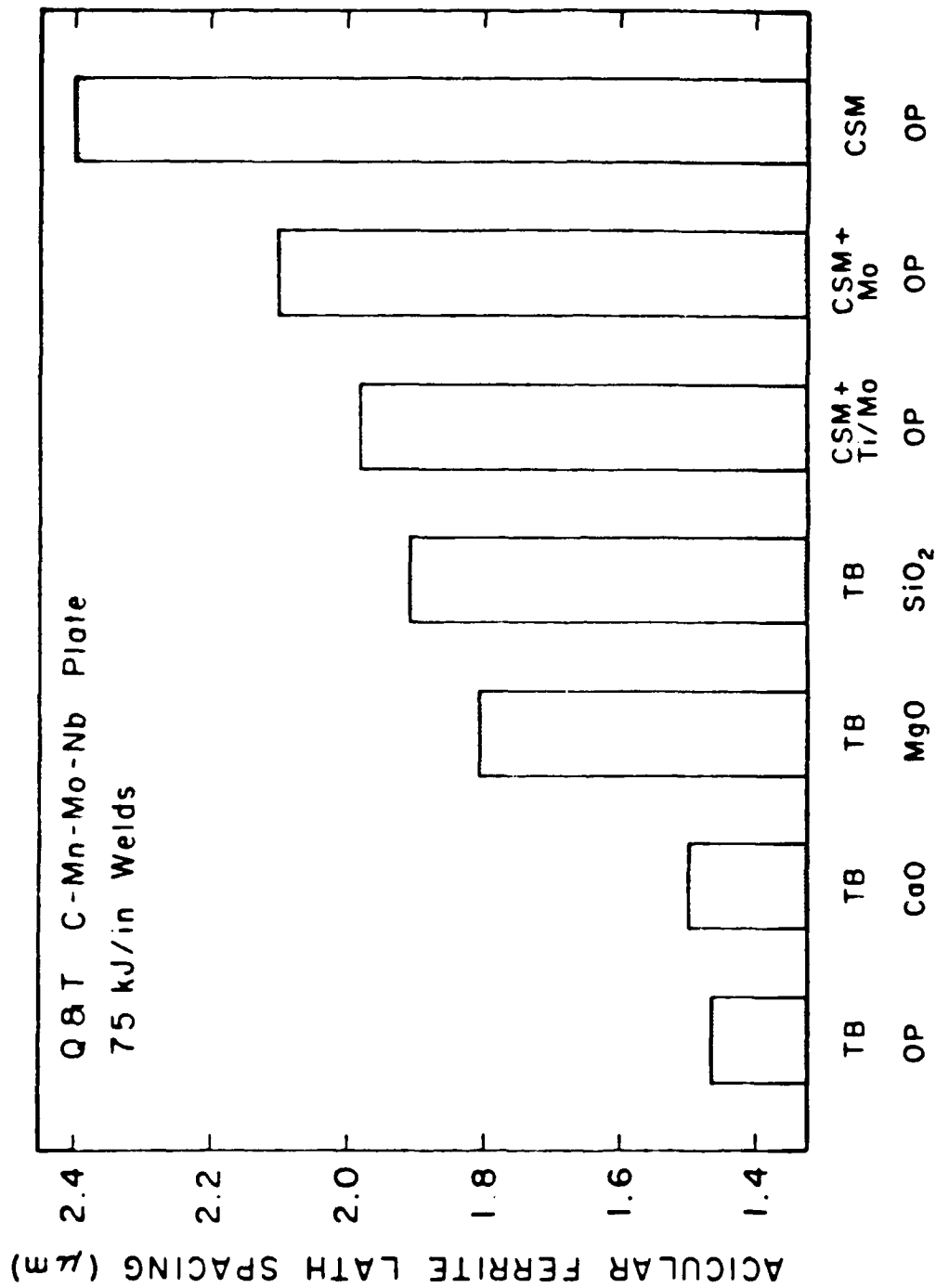


Figure 21. The mean acicular ferrite lath spacing observed at the center line of seven experimental submerged arc welds performed on quenched and tempered C-Mn-Mo-Nb plate.

from 2.4 to 2.1 microns. Weld (CSM + Ti/Mo)-OP showed a large change in microstructure which came from the addition of titanium and molybdenum to the weld pool from the wire. This weld produced about 50 percent acicular ferrite and contained an acicular ferrite lath spacing of 2.0 microns. The only compositional difference between weld (CSM + Ti/Mo)-OP and the commercial weld TB-OP, which produced the best microstructure, was that weld TB-OP contained boron in the weld metal. The change in transformation behavior due to this boron addition from the wire caused the volume percent acicular ferrite to increase from 50 to 85 percent, and refined the lath size from 2.0 to 1.4 microns. A comparison of Figures 20 and 21 show that there is a systematic correlation between the volume fraction of acicular ferrite and acicular ferrite lath spacing. An increase in the volume fraction from 26 percent to 85 percent, directly correlates with a decrease in mean lath size from approximately 2.4 microns to 1.4 microns.

Figure 22 shows the acicular ferrite lath spacing plotted against the hardness values that were recorded in Table VIII. This plot is analogous to a Hall-Petch (81) type expression of:

$$\sigma = \sigma_0 + k d^{-1/2} \quad (10)$$

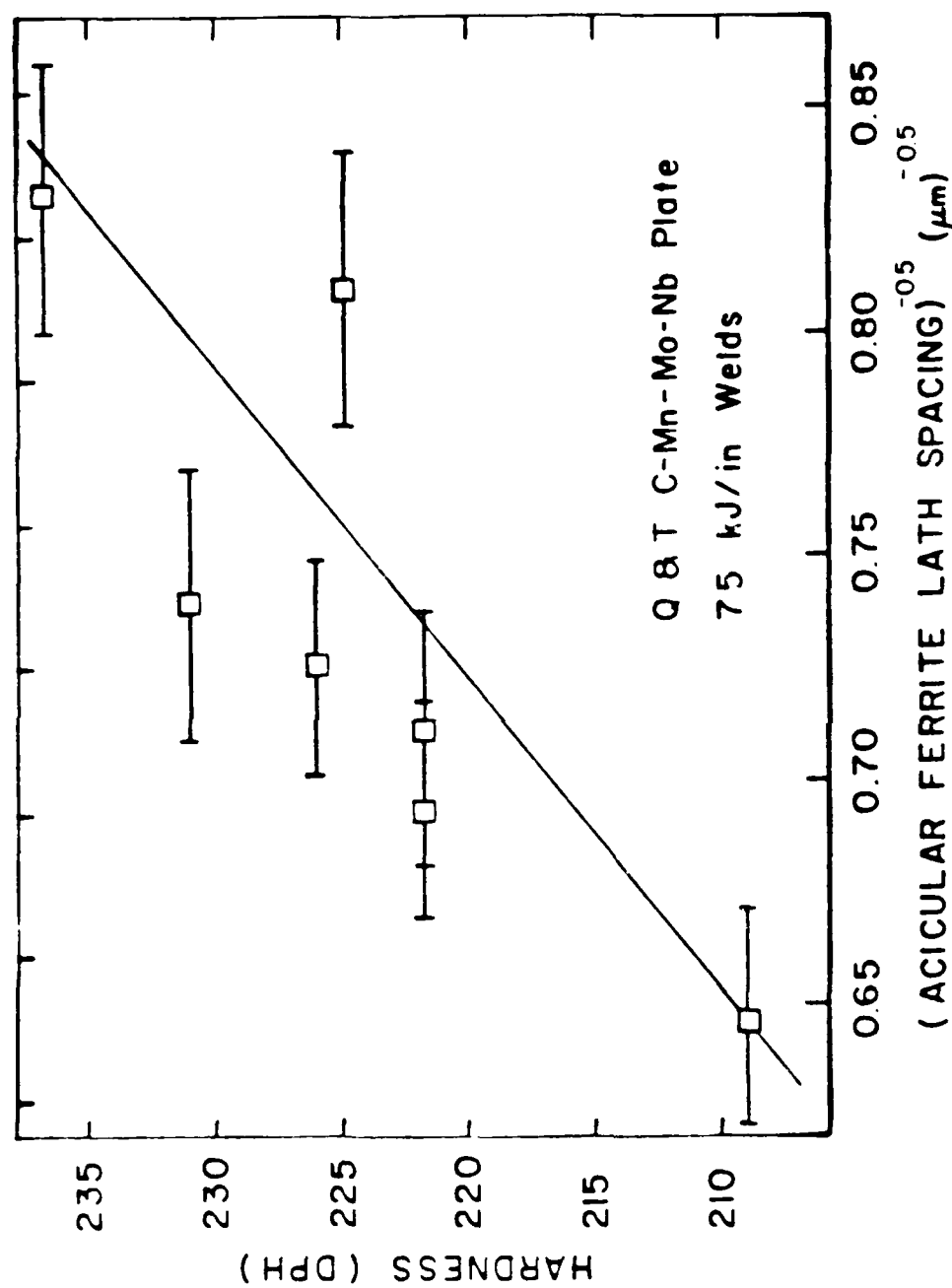


Figure 22. Hardness plotted as a function of acicular ferrite lath spacing of submerged arc welds performed on quenched and tempered C-Mn-Mo-Nb plate.

where σ is the yield strength, σ_0 is the base level of strength, k is a constant, and d is the average grain diameter. Equation 10 shows the dependence of grain size on strength, which can be directly related to hardness of the material by the following expression:

$$H = C_1 (\sigma) \quad (11)$$

where H is the hardness, and C_1 is a constant. Figure 22 exhibits a trend of decreasing hardness in the weld metal as the acicular ferrite lath size increases.

III.3. ELEMENT EFFECTS

An approach often taken to quantify the effect of alloy elements in weld metal is to relate the transformation products to a combined hardenability index such as an effective carbon equivalent. A carbon equivalent as formulated by Ito and Bessyo (82), which was initially used as a cold cracking parameter, has been used successfully to determine the relative hardenability of various microalloyed steels (83-84). This empirical expression is:

$$P_{cm} = C + \frac{(Mn + Cu + Cr)}{20} + \frac{Si}{30} + \frac{Ni}{60} + \frac{Mo}{15} + \frac{V}{10} + \frac{5B}{10} \quad (12)$$

where compositions are in weight percent. Figure 23 shows the P_{cm} carbon equivalent plotted against the volume percent acicular ferrite for each weldment. As the weld metal carbon equivalent is increased from 0.18 to 0.21, the acicular ferrite content in the microstructure increases from 26 to 85 percent. The volume percent grain boundary ferrite as well as the total amount of primary ferrite was plotted against the P_{cm} carbon equivalent and is shown in Figures 24 and 25 respectively. Both exhibit a decreasing trend in either grain boundary ferrite or primary ferrite with increasing carbon equivalent.

Grong (85) has reviewed the current literature, and shown that the Ito-Bessyo carbon equivalent is an indicator of the microstructure developed in weld metal only if the titanium level is greater than approximately 0.0045 weight percent, as shown in Figure 26. The titanium contents in the weld metals of the current study were plotted against the percent acicular ferrite in Figure 27. These data show the same trend as that presented in the previous figure. The two solid squares in Figure 27 represent welds (CSM + Mo)-OP and (CSM + Ti/Mo)-OP. For these welds, one of the differences between their respective weld metal compositions was that weld (CSM + Mo)-OP did not contain titanium. Although titanium can not be assumed to be the only

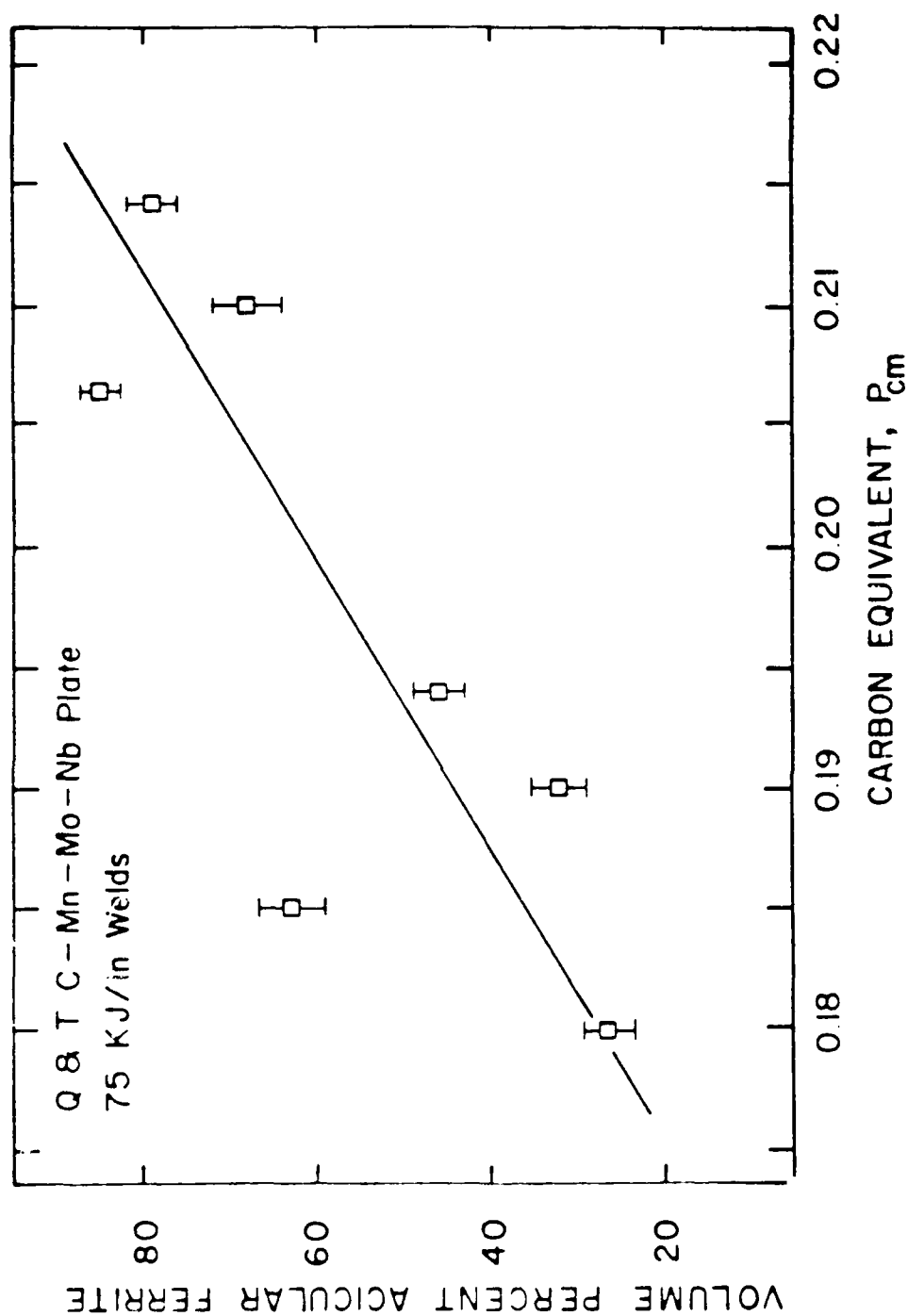


Figure 23. The volume percentage of acicular ferrite of submerged arc welds performed on quenched and tempered C-Mn-Mo-Nb plate as a function of their respective Ito-Bessyo carbon equivalent numbers.

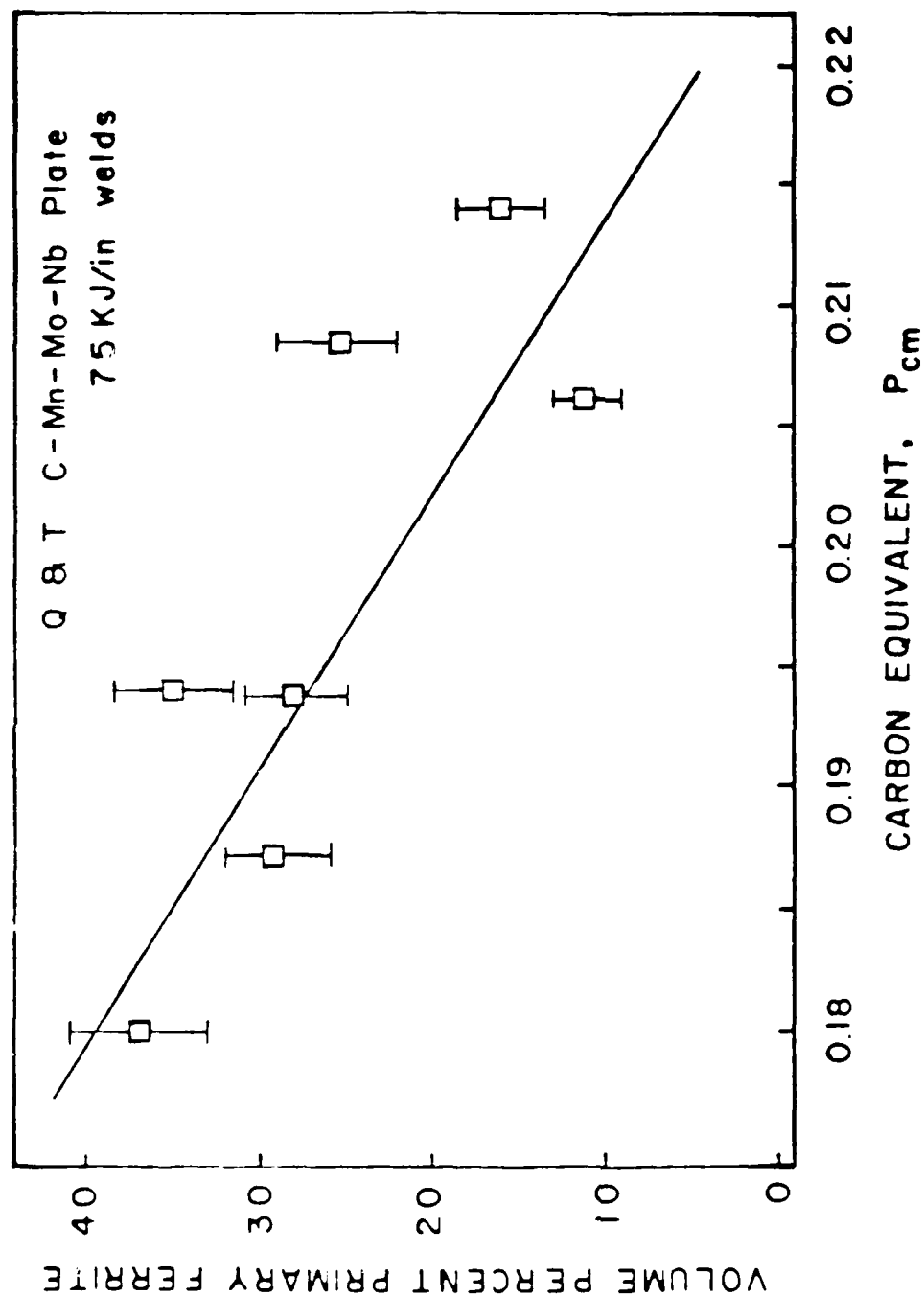
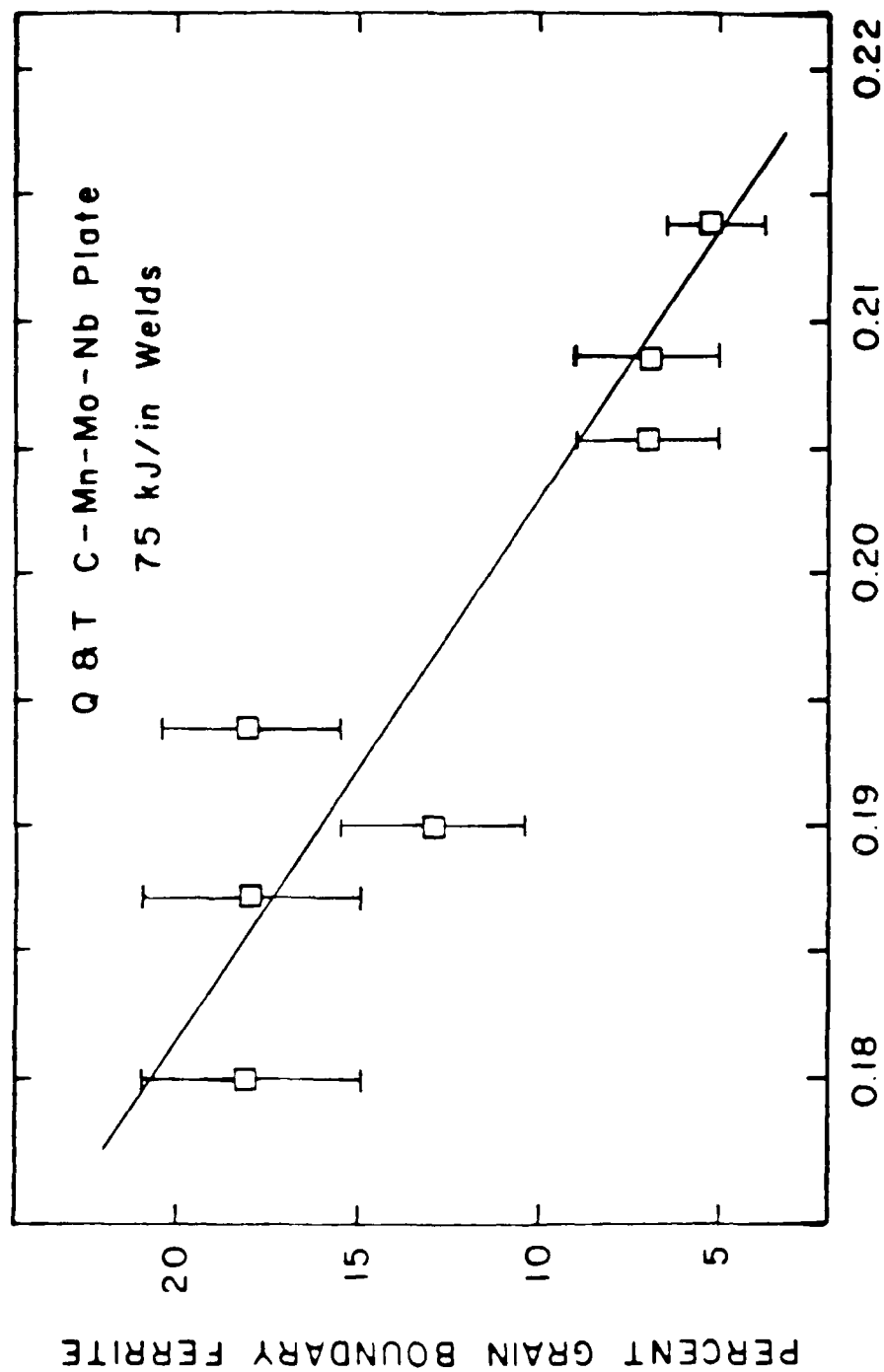


Figure 24. The volume percentage of primary ferrite of submerged arc welds performed on quenched and tempered C-Mn-Mo-Nb plate as a function of their respective Ito-Bessyo carbon equivalent numbers.



CARBON EQUIVALENT, P_{cm}

Figure 25. The volume percentage of grain boundary ferrite of submerged arc welds performed on quenched and tempered C-Mn-Mo-Nb plate as a function of their respective Ito-Bessyo carbon equivalent numbers.

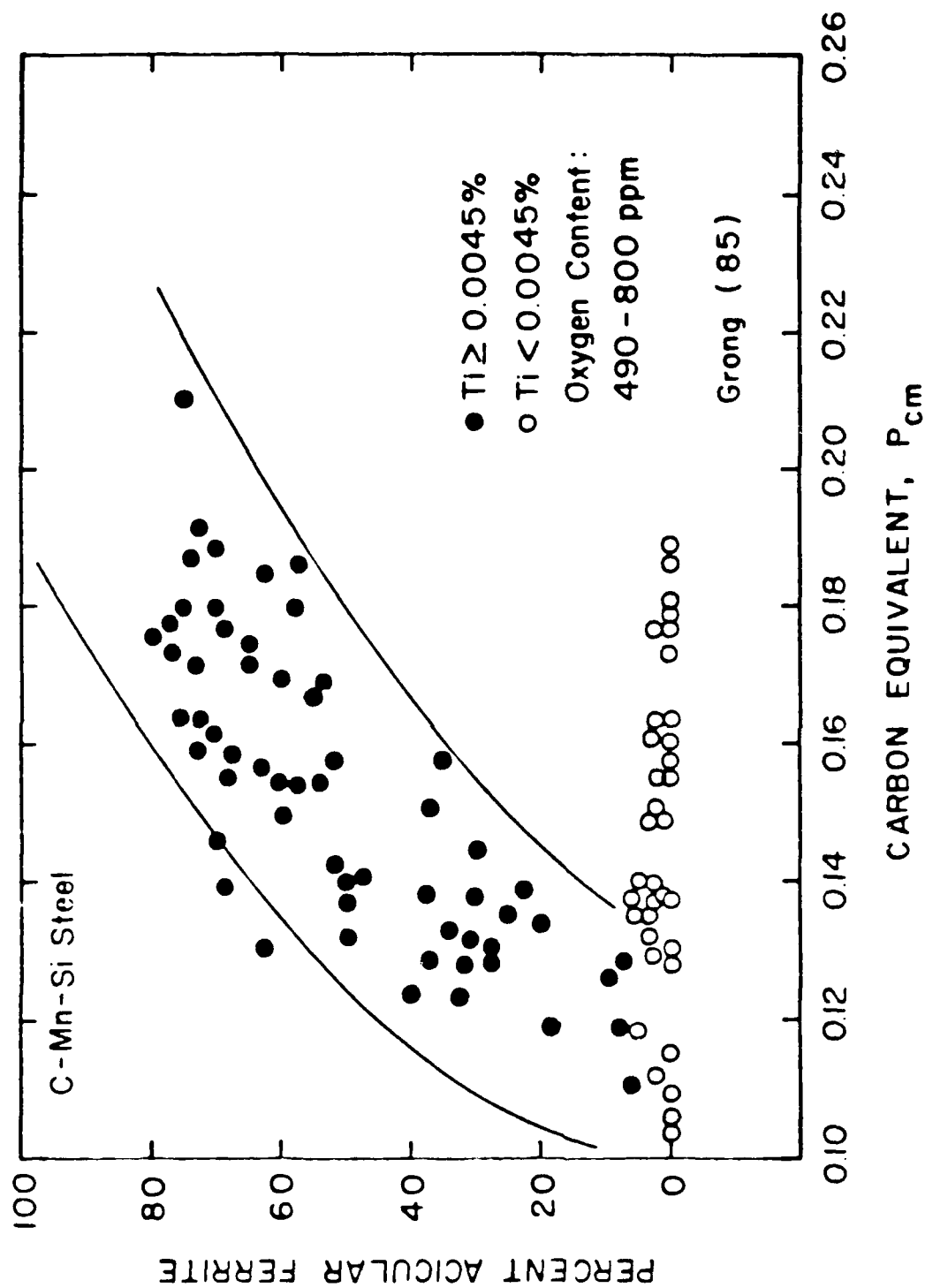


Figure 26. The volume percentage of acicular ferrite of submerged arc welds performed on C-Mn-Si plate as a function of their respective Ito-Bessyo carbon equivalent numbers having two different levels of titanium.

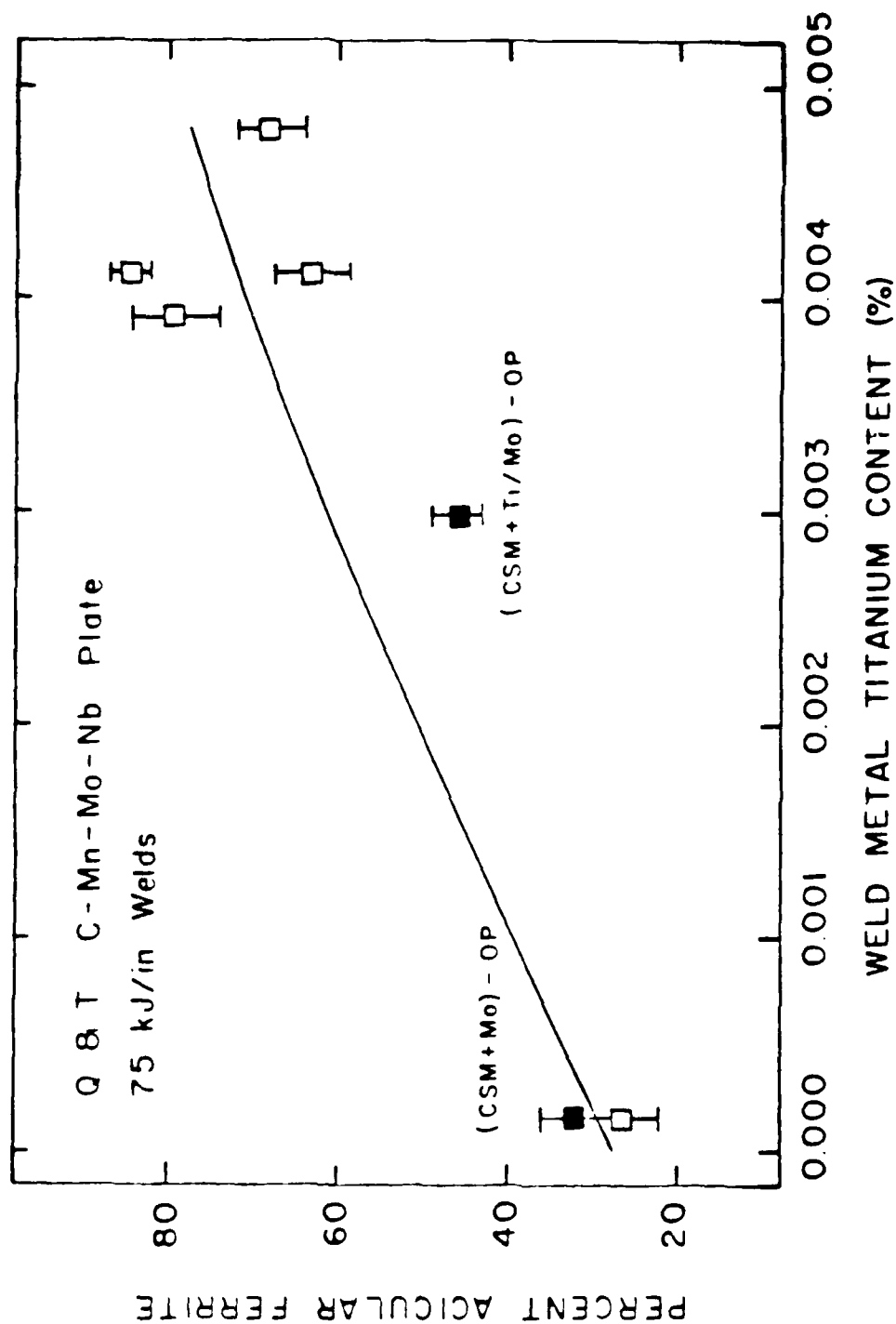


Figure 27. The volume percentage of acicular ferrite of submerged arc welds performed on quenched and tempered C-Mn-Mo-Nb plate as a function of their respective weld metal titanium contents.

important microalloying element, Figure 27 suggests that it is indeed important to the promotion of acicular ferrite.

Since titanium and boron have been shown by researchers (14,39-40,42,57,60-67) to have a favorable effect on the production of acicular ferrite, the calculation of the amount of boron per grain boundary area was made (see Appendix D) using the assumption that all the boron was at the grain boundaries. This is a reasonable assumption based on the result of Hondros and Seah (86) who showed that only one in ten thousand boron atoms would remain in solution in the lattice and not at the grain boundaries. Weld metal boron content per grain boundary area was plotted against the volume percent acicular ferrite, as shown in Figure 28. An increase in the amount of acicular ferrite (from 26 to 85 volume percent) with a corresponding increase in grain boundary concentration indicates that boron helps in the production of acicular ferrite, probably by suppressing the grain boundary ferrite transformation (39-40,42,60-61). Figure 29 shows the weld metal boron content per grain boundary area plotted against the percent grain boundary ferrite. A increase in grain boundary concentration was shown to decrease the amount of grain boundary ferrite in the weld metal from 18 to 5 percent. The two dark squares in this plot represent welds TB-OP and (CSM + Ti/Mo)-OP,

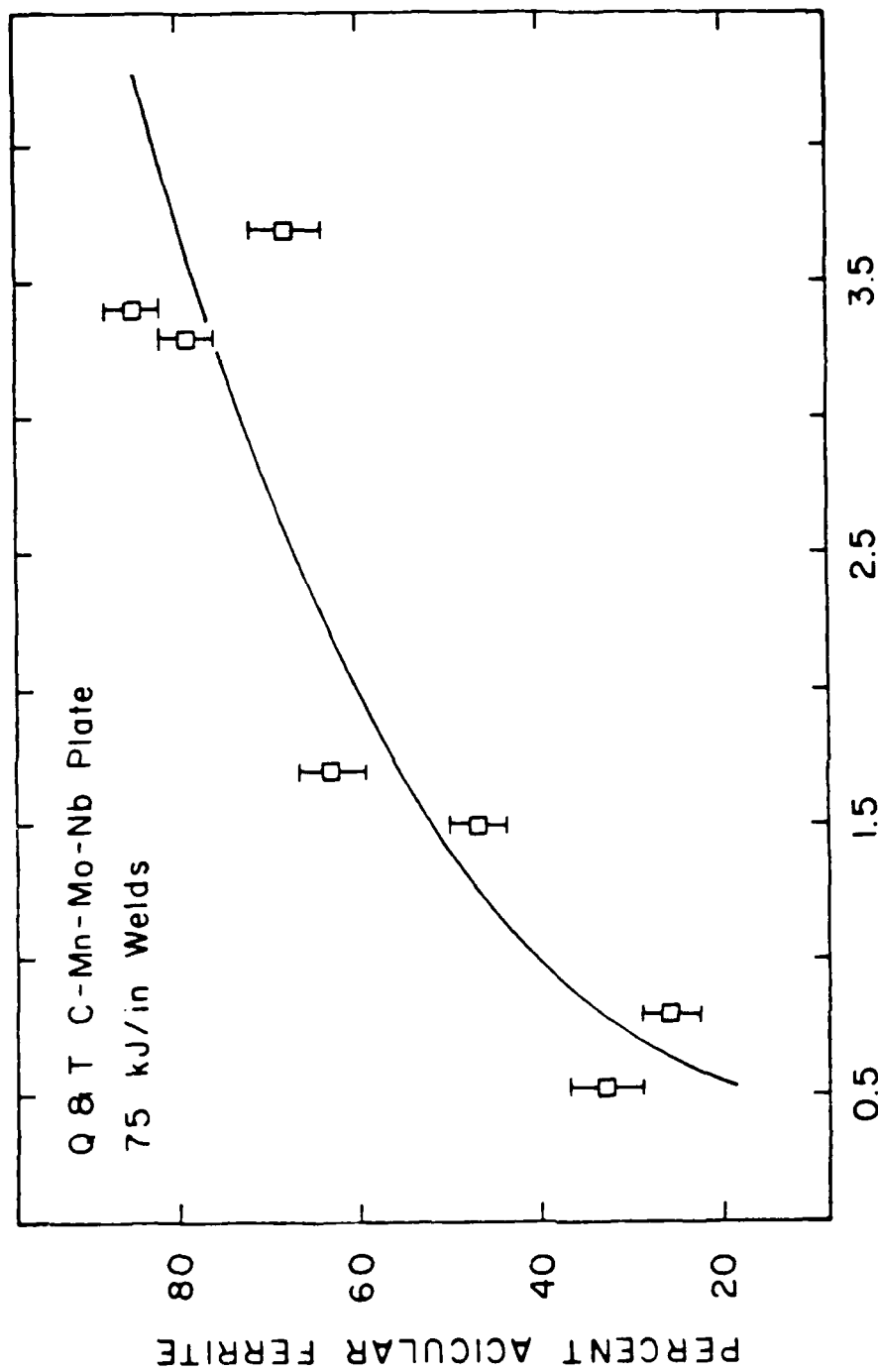


Figure 28. The volume percentage of acicular ferrite of submerged arc welds performed on quenched and tempered C-Mn-Mo-Nb plate as a function of their respective grain boundary boron concentrations.

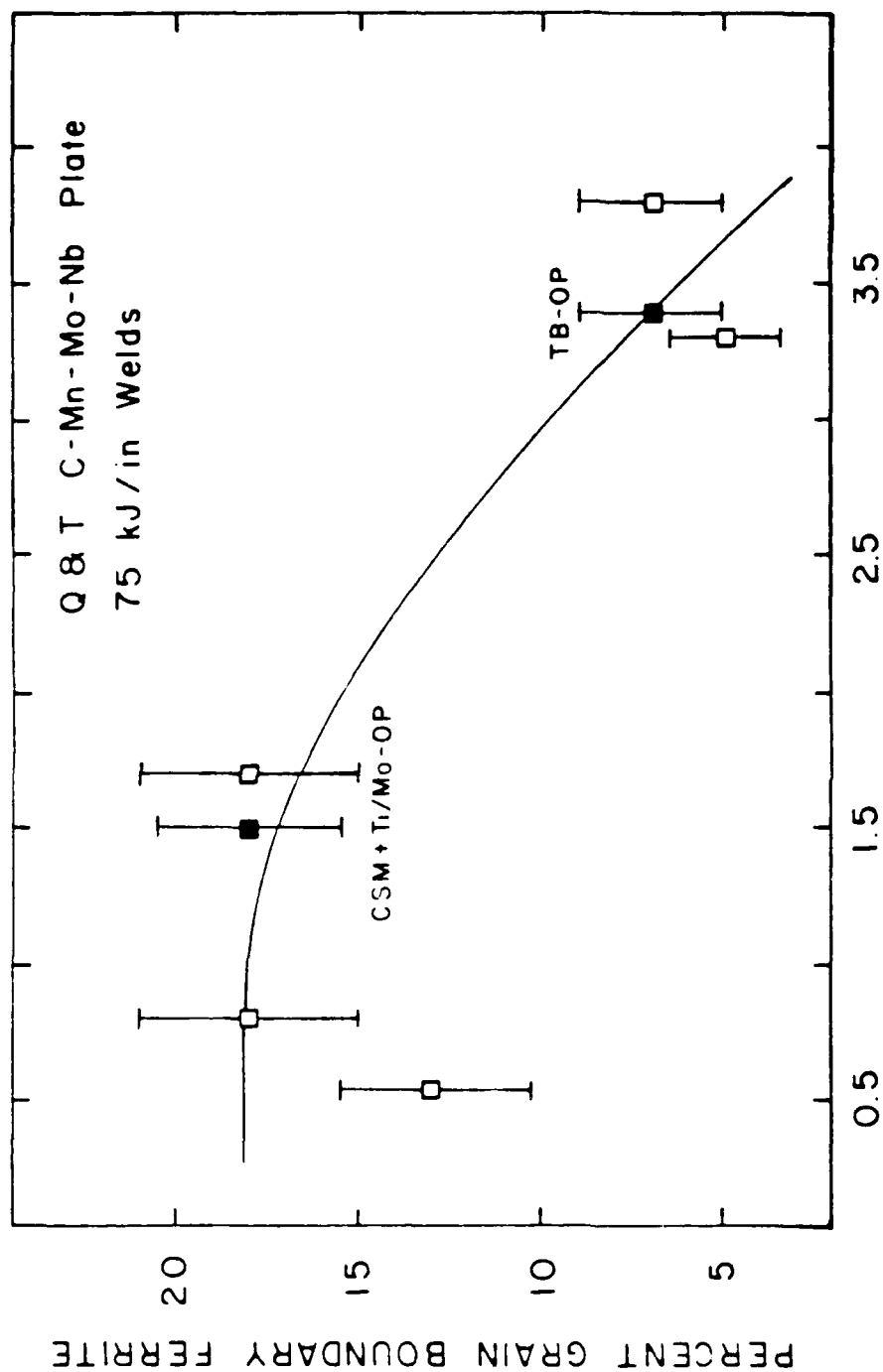


Figure 29. The volume percentage of grain boundary ferrite of submerged arc welds performed on quenched and tempered C-Mn-Mo-Nb plate as a function of their respective grain boundary boron concentrations.

with the main difference between their respective weld metal concentrations being a change of 0.0010 weight percent boron. This extra amount of boron changes the transformation behavior of the weld metal enough to decrease the volume percent grain boundary ferrite from 18 to 7 percent. Thus, the amount of grain boundary ferrite lost, corresponds to the gain of acicular ferrite that was shown in Figure 28. Although boron can not be assumed to be the only important microalloying element, Figures 28 and 29 agrees with other researchers (39-40,60-61) in showing that boron is indeed important in suppressing the nucleation of allotriomorphic ferrite.

Recent literature has shown (87) that excessive amounts of boron or titanium will be detrimental to the weld metal properties; thus, a specific amount of titanium and boron are required to produce the desired microstructure. The optimal values of these two elements are affected by other elements such as oxygen, nitrogen, aluminum, manganese, molybdenum, and nickel, as well as the welding parameters (87). Comparing the experimental weld metal compositions in Table V with data from researchers in Table II (57,62-67), shows that the optimal values of titanium and boron have not been exceeded.

III.4. MECHANICAL TESTING

Subsize Charpy specimens were tested from welds TB-OP and CSM-OP at various temperatures and these results are presented in Figure 30. Weld TB-OP, which is the best weld microstructurally, exhibited a transition temperature of about -100°C , while weld CSM-OP, the worst weld in terms of microstructure, showed a transition temperature of -40°C . The fracture surfaces of these impact specimens are shown in Figure 31, showing the percent shear fracture at their respective test temperatures. Subsize tensile bars were tested from welds TB-OP and CSM-OP and they exhibited the following weld metal yield strengths:

WELD	YIELD STRENGTH
TB-OP*	80 ksi
CSM-OP*	70 ksi

Comparing these results with the data in Figure 30, a fine interlocking acicular ferrite microstructure was shown to enhance the toughness of the weld as well as improving the weld metal yield strength, while welds that contain a large amount of primary ferrite and bainite will exhibit poorer weld metal properties.

Recorded impact values of subsize Izod specimens that

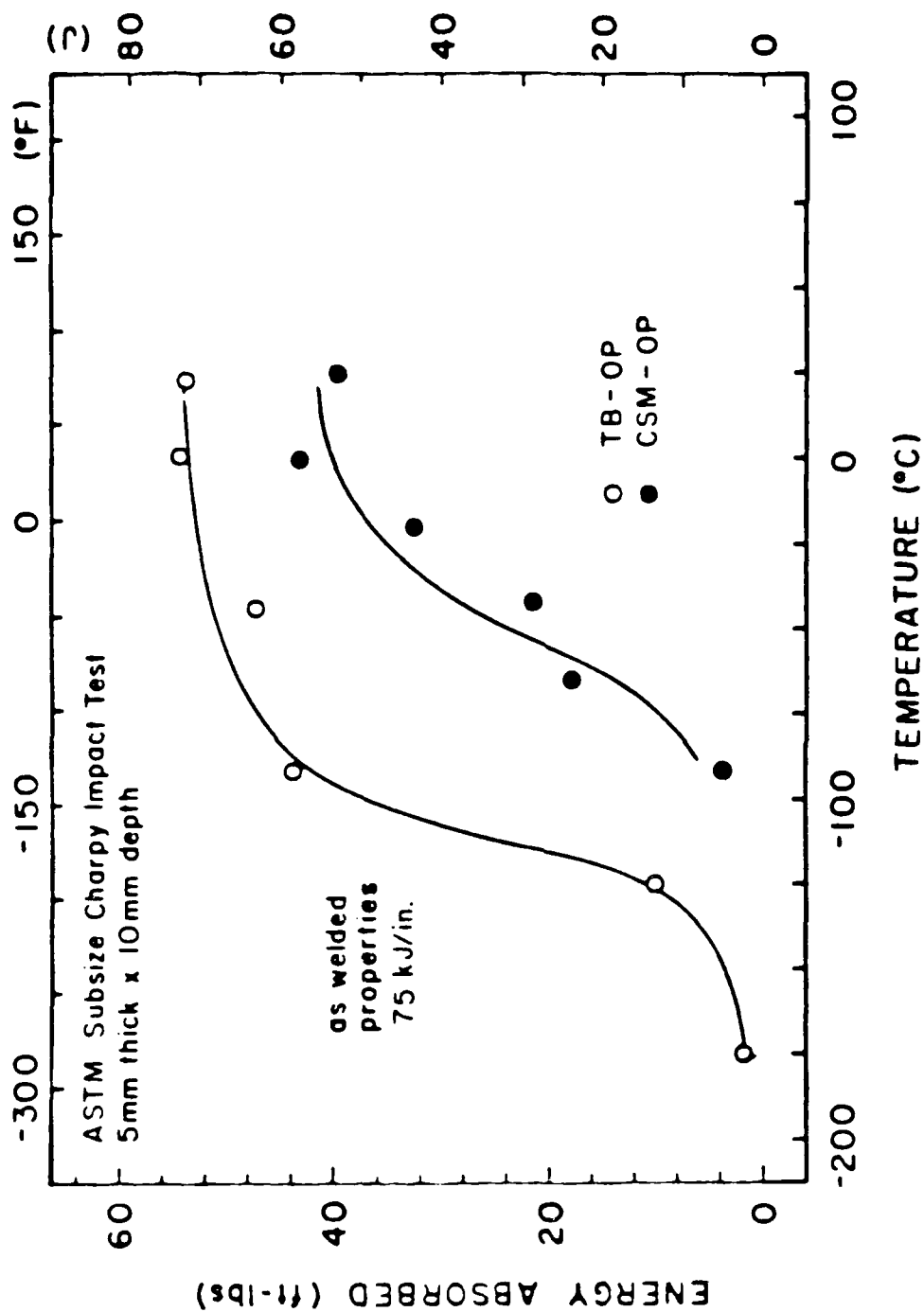


Figure 30. Subsize (5.0 x 10.0 x 55.0 mm) Charpy impact values of two submerged arc welds performed on quenched and tempered C-Mn-Mo-Nb plate as a function of temperature.

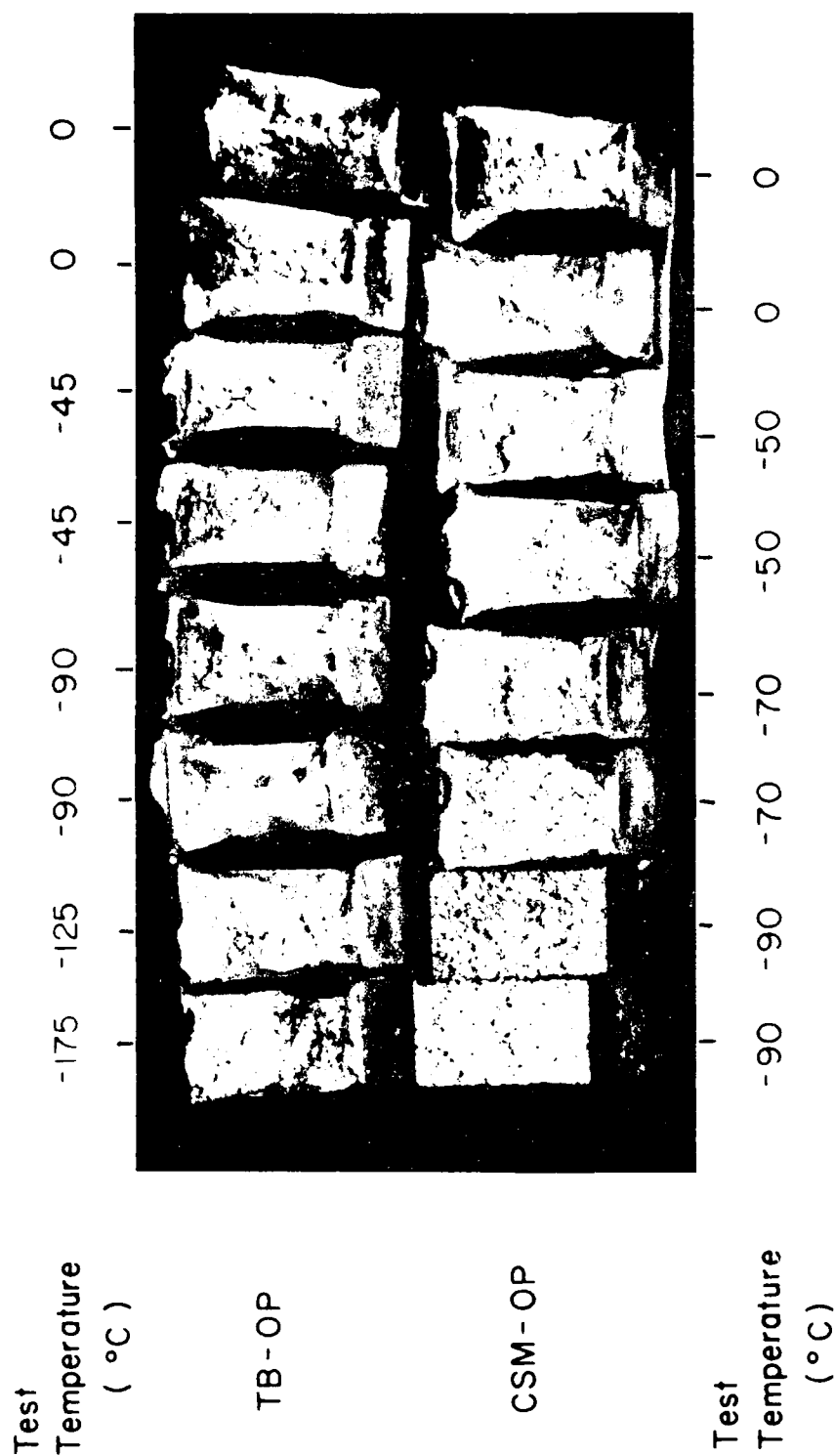
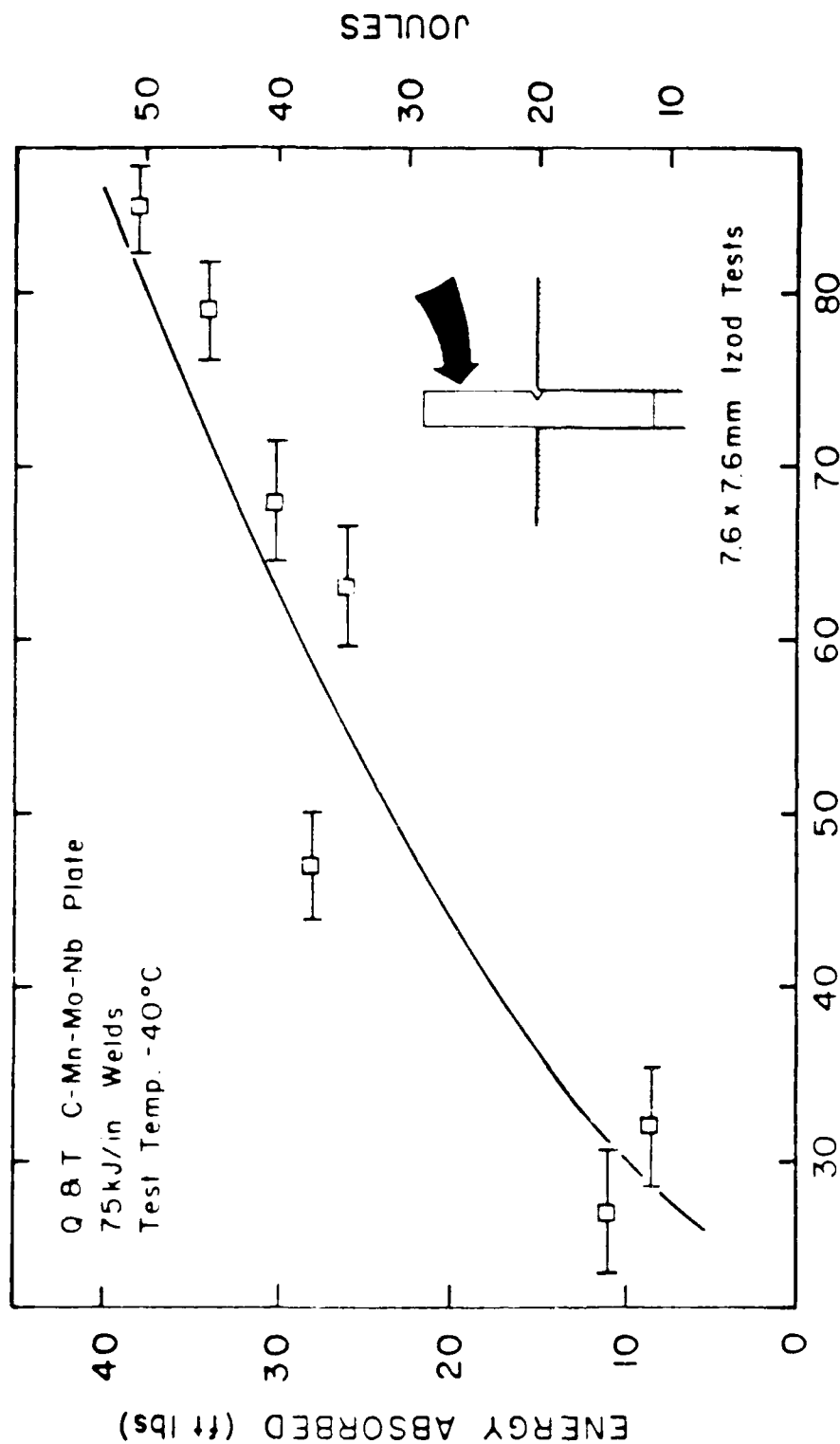


Figure 31. Subsize (5.0 x 10.0 x 55.0 mm) Charpy fracture surfaces of two submerged arc welds performed on quenched and tempered C-Mn-Mo-Nb plate showing the effect of temperature on fracture appearance.

were tested from all seven experimental welds at -40°C , were plotted against the volume percent of acicular ferrite, as shown in Figure 32. These data exhibit an increase in energy absorbed from 9 to 38 ft-lbs as the volume of acicular ferrite increases from 26 to 85 percent in the weld metal. These results correlate well with Figure 33, which shows the same increase in energy absorbed as the primary ferrite content decreases from 37 to 11 percent. The two solid squares in Figure 33 represent welds TB-CaO and TB-MgO, with the only difference between them being the flux compositions. Figure 33 shows that the weld made with the MgO flux produced more primary ferrite in the weld metal microstructure and thus exhibited poorer toughness than the weld made with the CaO flux. These results indicate that MgO does not simply substitute for CaO as a submerged arc flux ingredient.

Figure 34 shows the fracture surfaces of the subsize Izod specimens. The percent shear fracture was measured from the Izod specimens and these results are plotted against the volume percent acicular ferrite in Figure 35. As indicated in Figure 35, an increase in percent shear from 10 to 100 percent was observed as the acicular ferrite volume fraction increased from 26 to 85 percent. Figure 36, which is a plot of the energy absorbed at -40°C versus the



VOLUME PERCENT ACICULAR FERRITE

Figure 32. Subsize (7.6 x 7.6 x 55.0 mm) Izod impact impact values of submerged arc welds performed on quenched and tempered C-Mn-Mo-Nb plate as a function of their respective acicular ferrite contents.

AD-A149 529

THE EFFECT OF FILLER WIRE AND FLUX COMPOSITIONS ON THE
MICROSTRUCTURE AND (U) COLORADO SCHOOL OF MINES GOLDEN
DEPT OF METALLURGICAL ENGINEERING N A FLECK AUG 84

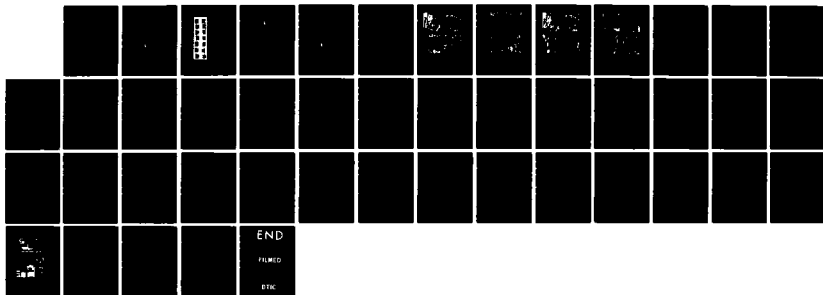
2/2

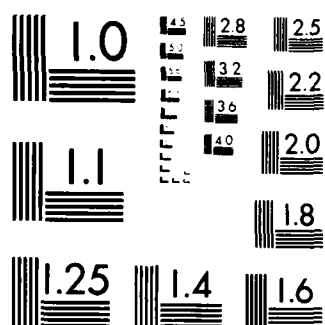
UNCLASSIFIED

DTNSRDC/SHE-CR-17-84 N00014-83-K-0779

F/G 11/9

NL





MICROCOPY RESOLUTION TEST CHART
NATIONAL BUREAU OF STANDARDS 1963-A

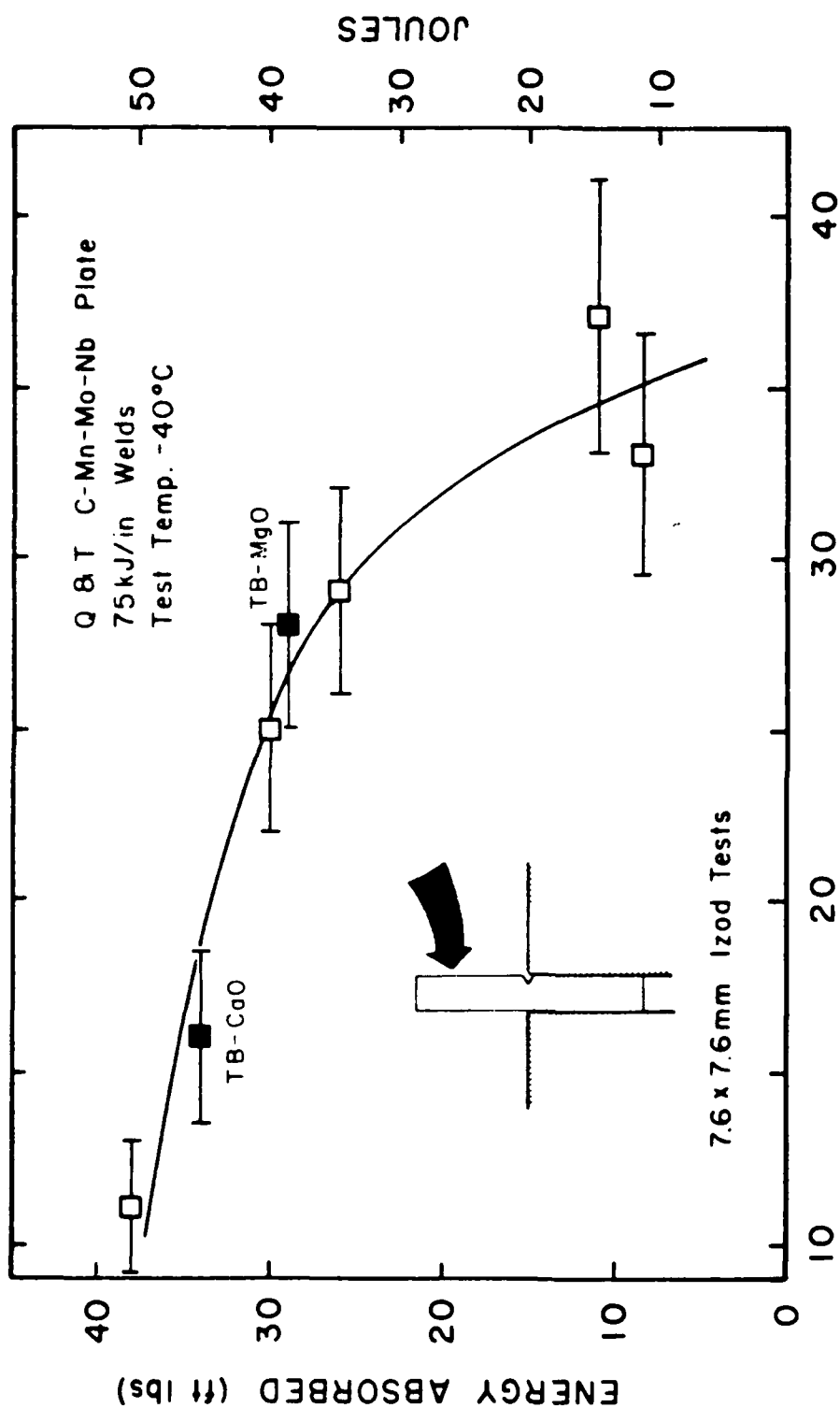
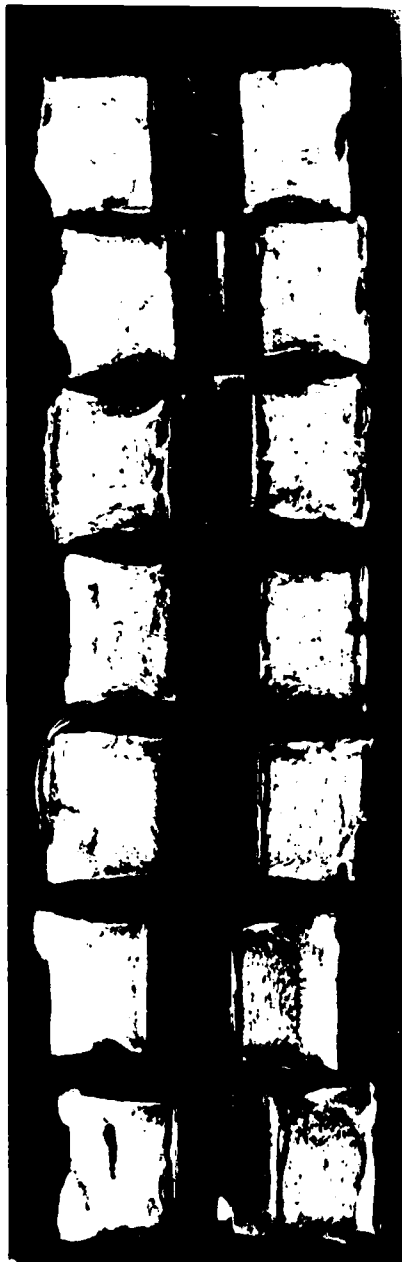


Figure 33. Subsize (7.6 x 7.6 x 55.0 mm) Izod impact values of submerged arc welds performed on quenched and tempered C-Mn-Mo-Nb plate as a function of their respective primary ferrite contents.

SUBSIZE IZOD FRACTURE SURFACES

TEST TEMPERATURE = - 40 °C



TB	TB	TB	TB	CSM+	CSM+	CSM
OP	CaO	MgO	SiO ₂	Ti/Mo	Mo	OP
				OP	OP	

Figure 34. Subsize (7.6 x 7.6 x 55.0 mm) Izod fracture surfaces of seven submerged arc welds performed on quenched and tempered C-Mn-Mo-Nb plate showing the different fracture appearances produced at constant test temperature.

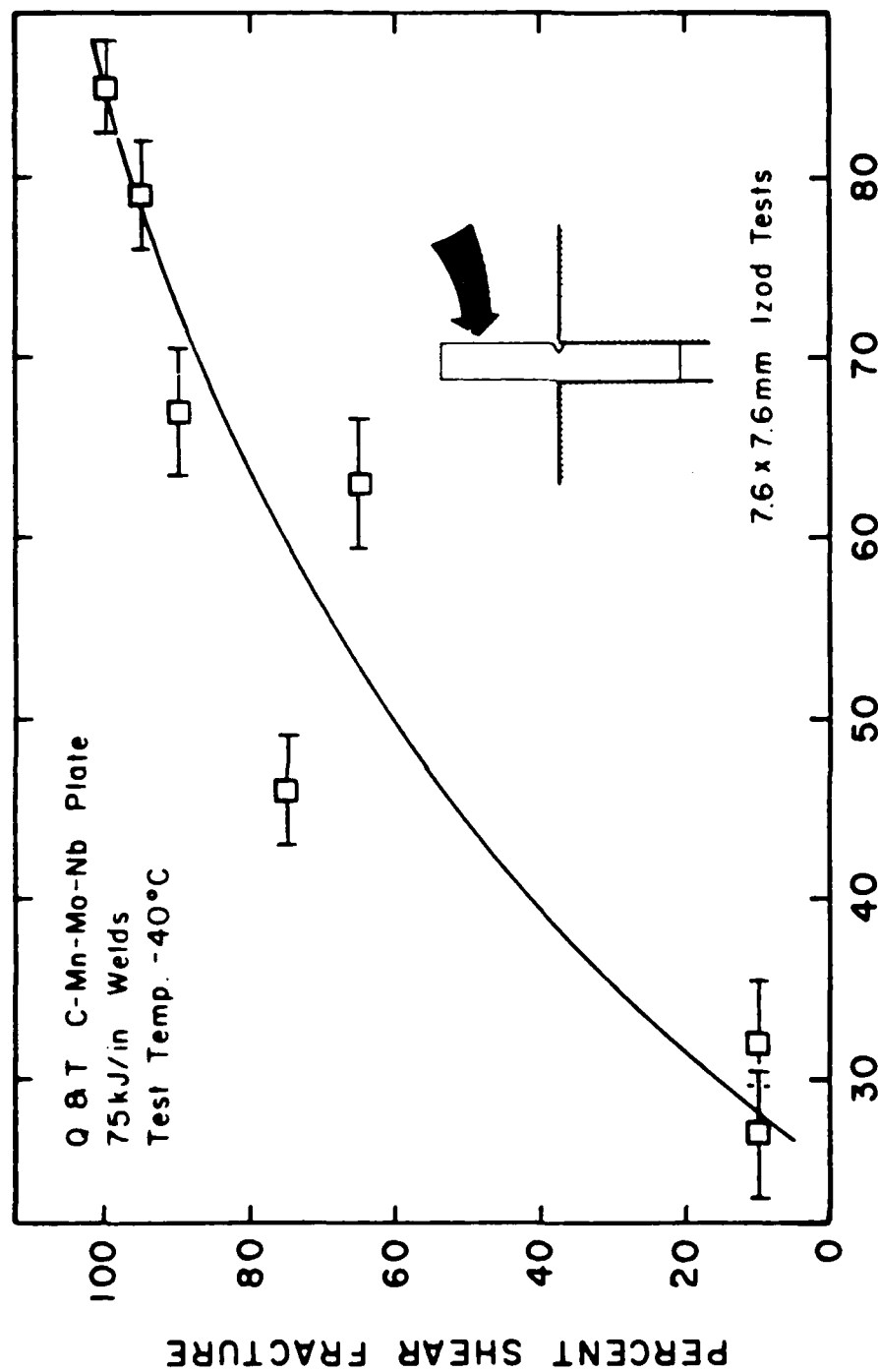


Figure 35. The percent shear fracture area from subsize (7.6 x 7.6 x 55.0 mm) Izod specimens of submerged arc welds performed on quenched and tempered C-Mn-Mo-Nb plate as a function of their respective primary ferrite contents.

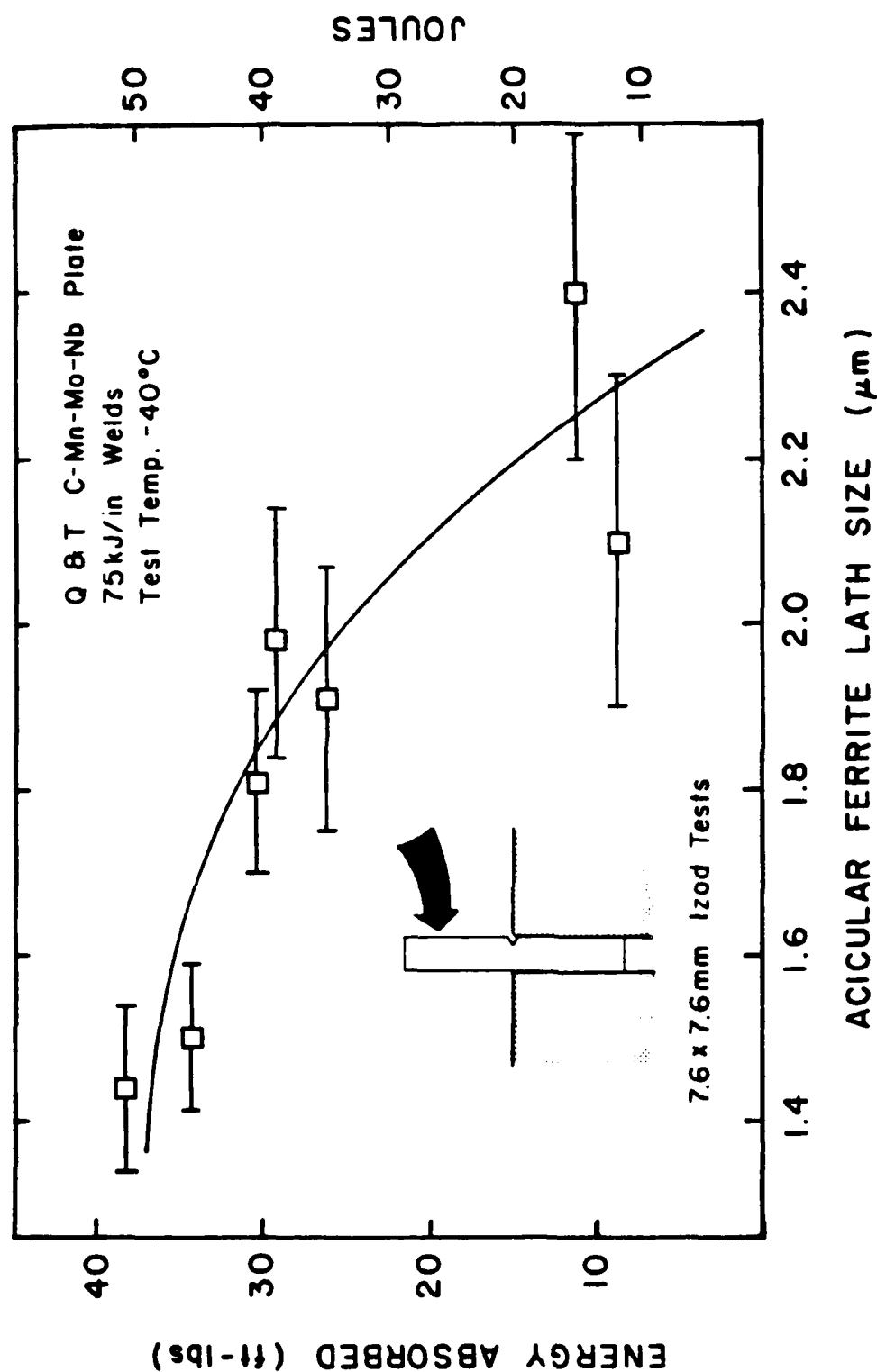


Figure 36. Subsize (7.6 x 7.6 x 55.0 mm) Izod impact values of submerged arc welds performed on quenched and tempered C-Mn-Mo-Nb plate as a function of their respective acicular ferrite spacing.

mean acicular ferrite lath size, exhibits a decrease in the energy absorbed from 38 to 9 ft-lbs as the lath size increases from 1.4 to 2.4 microns. Figures 35 and 36 support other previous work (1) in showing that by increasing the percent acicular ferrite in the weld metal, and decreasing the acicular ferrite lath size, improved weld metal properties will be obtained.

Weld metal fractographs of the Izod specimens were taken at 1000X. The centerline fractographs, which are presented in Figures 37a 37b, 37c, and 37d, were taken at the root of the notch and 0.6 mm in from the notch. A schematic diagram showing where the fractographs were taken is located in the bottom left hand corner of the photographs in Figures 37a, 37b, 37c, and 37d (the crack propagates from left to right). The surfaces in Figures 37a and 37b show the different fracture appearances produced by changes in the flux during the welding operation. Weld TB-OP features a microvoid coalescence fracture mechanism with some tearing both at the notch and at 0.6 mm from the notch. Welds TB-CaO and TB-MgO also exhibit microvoid coalescence, but weld TB-CaO contains more elongated tearing dimples at the notch, which become equiaxed dimples as the crack front propagates. In contrast, weld TB-MgO exhibited elongated dimples throughout. A correlation can be made between the fracture

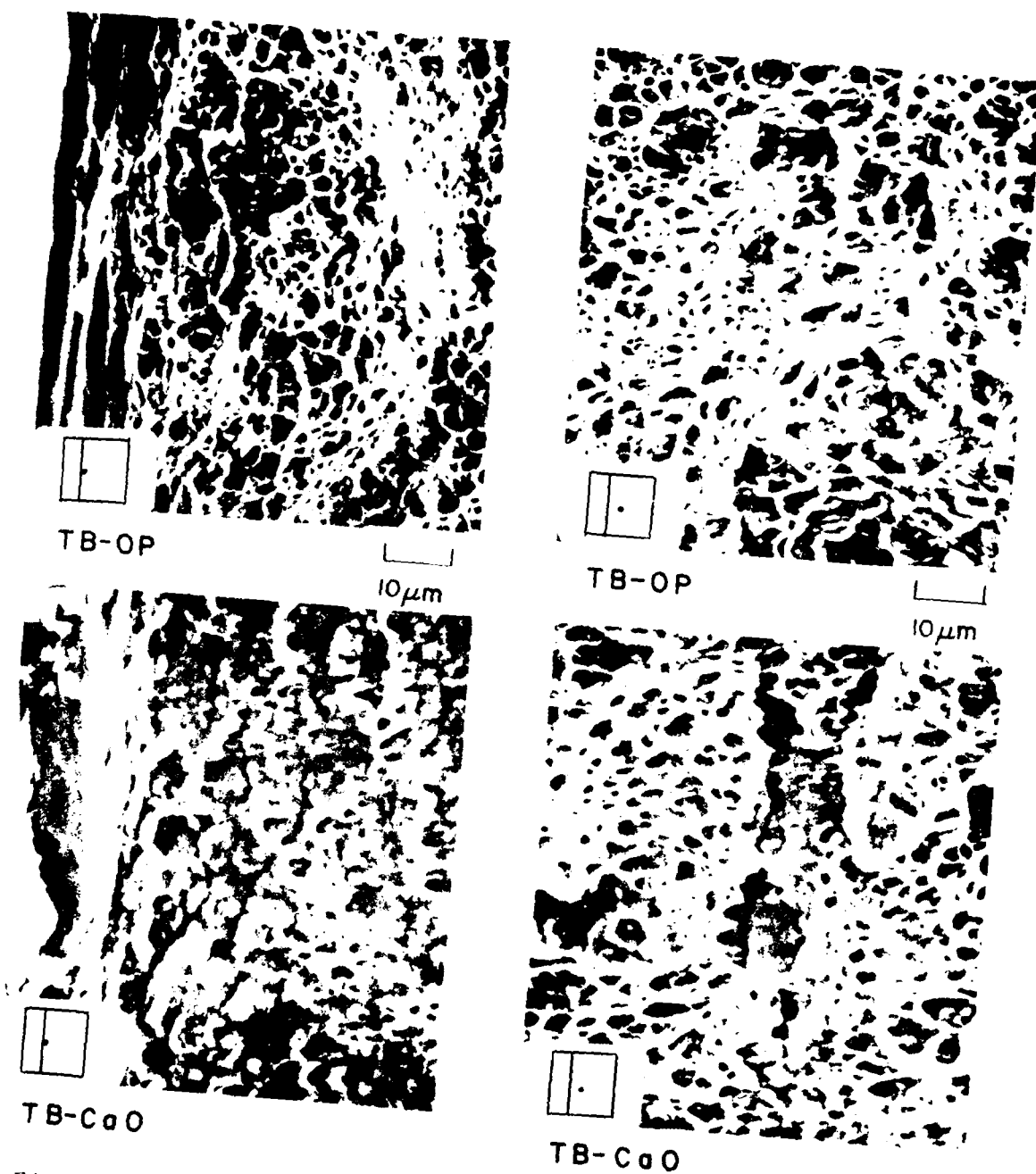


Figure 37a. Weld centerline fractographs of two subsize (7.6 x 7.6 x 55.0 mm) Izod specimens taken at the notch and 0.64 mm in from the notch. The specimen orientation is shown in Figure 16. Crack propagated from left to right. 1000x

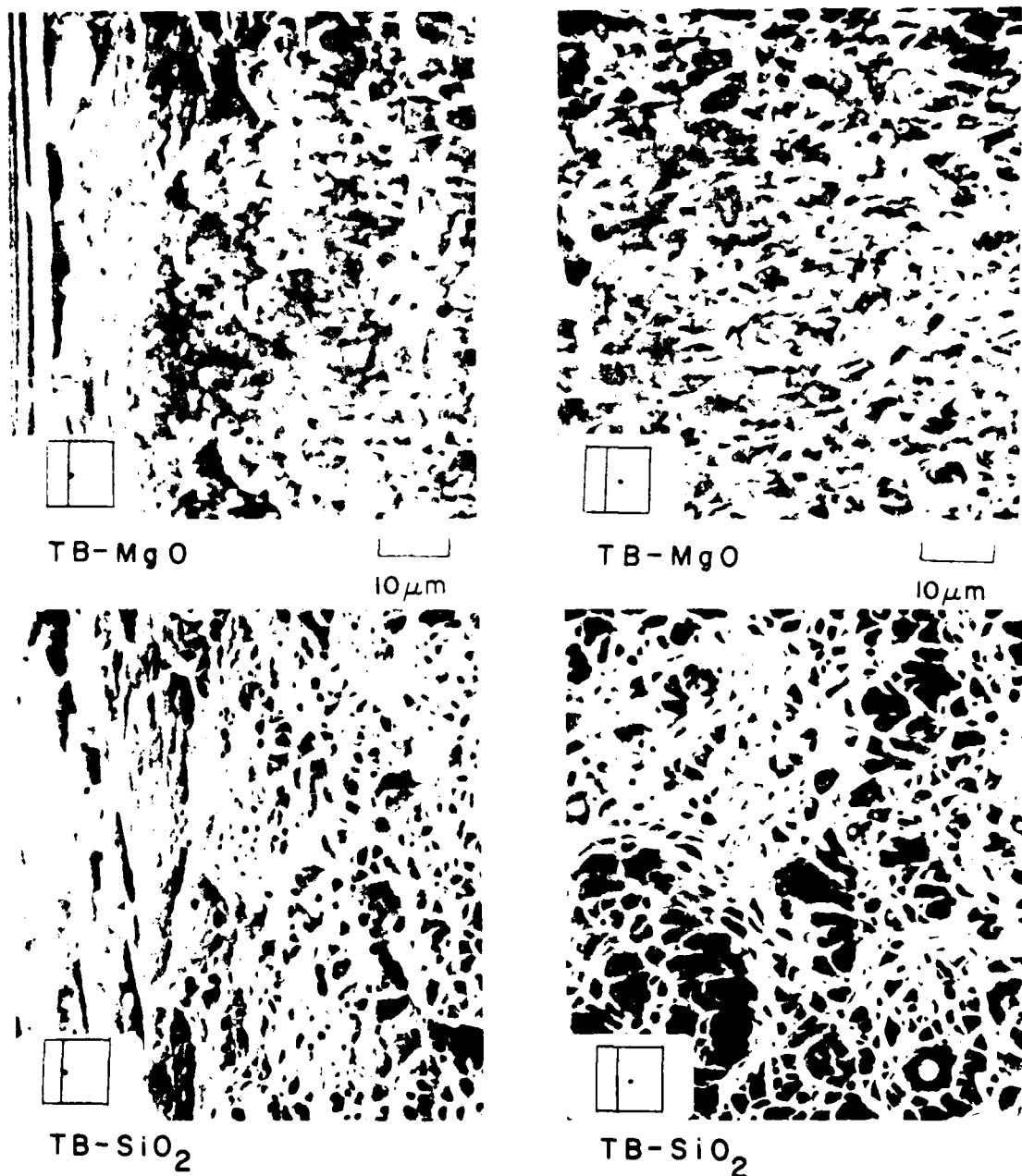


Figure 37b. Weld centerline fractographs of two subsize (7.6 x 7.6 x 55.0 mm) Izod specimens taken at the notch and 0.64 mm in from the notch. The specimen orientation is shown in Figure 13. Crack propagated from left to right. 1000x

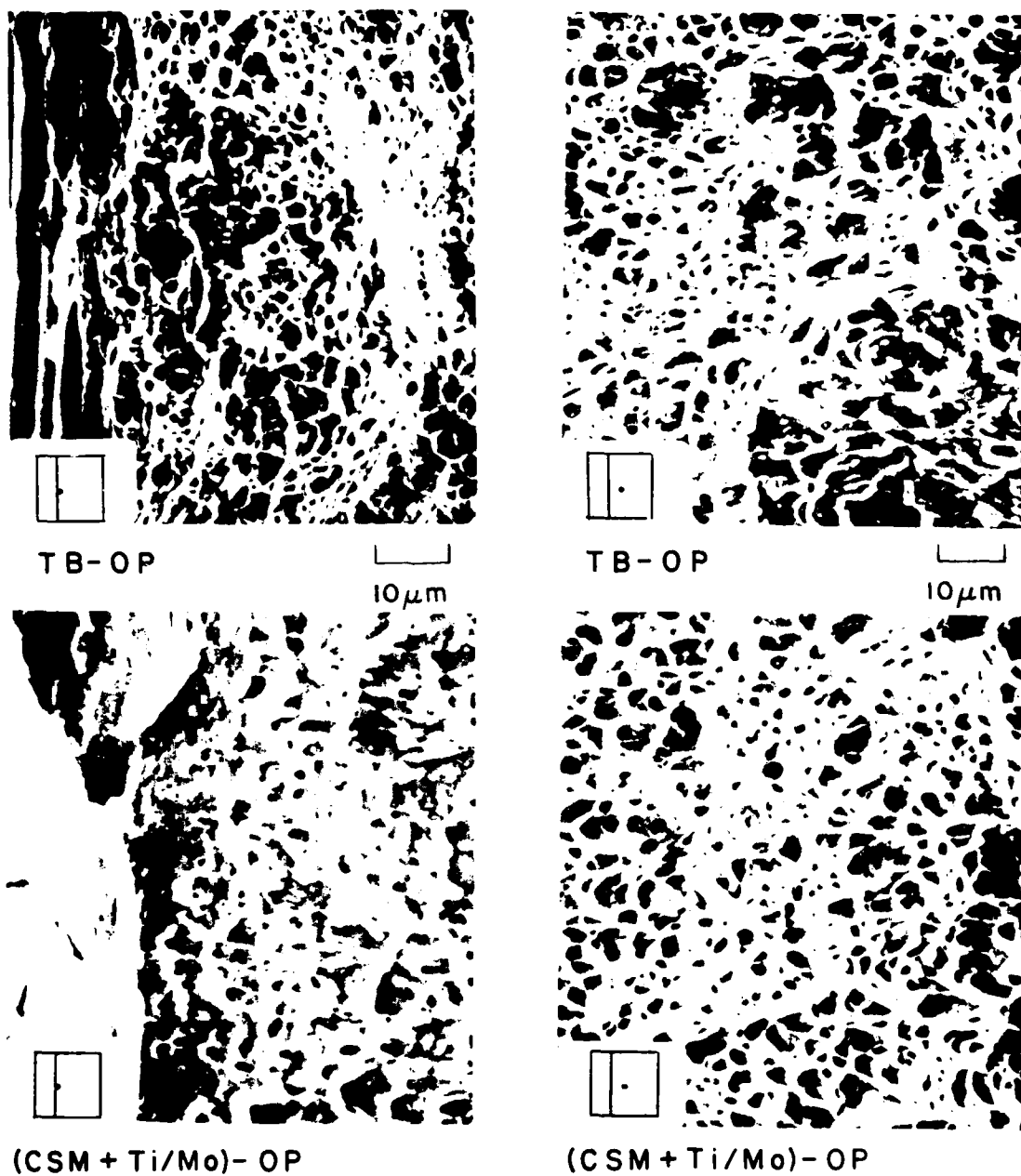
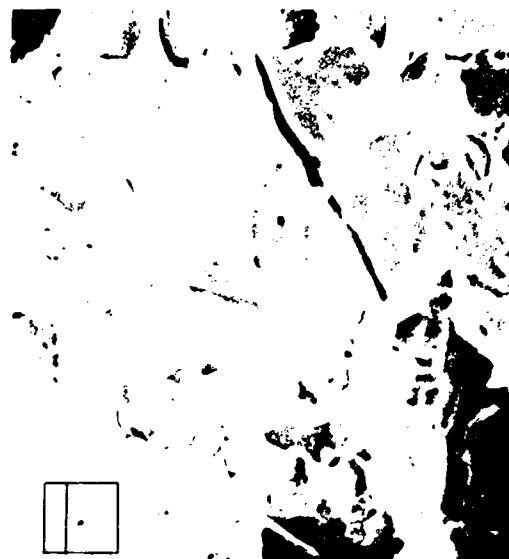


Figure 37c. Weld centerline fractographs of two subsize (7.6 x 7.6 x 55.0 mm) Izod specimens taken at the notch and 0.64 mm in from the notch. The specimen orientation is shown in Figure 16. Crack propagated from left to right. 1000x



(CSM+Mo)-OP

10 μ m

(CSM+Mo)-OP

10 μ m

CSM-OP



CSM-OP

Figure 37d. Weld centerline fractographs of two subsize (7.6 x 7.6 x 55.0 mm) Izod specimens taken at the notch and 0.64 mm in from the notch. The specimen orientation is shown in Figure 16. Crack propagated from left to right. 1000x

surfaces of the welds and their respective weld metal microstructures, presented in Figure 19a. As the percent of acicular ferrite decreased in the weld metal (going from weld TB-OP to TB-CaO to TB-MgO), the fracture surface changed from upper shelf microvoid coalescence to elongated tearing dimples, indicative of being in the transition range of the impact curve. Although weld TB-SiO₂ contained more equiaxed dimples on the fracture surface compared to welds TB-CaO and TB-MgO, large inclusions and other second phase particles were found on the surface which could explain the lower impact energy exhibited.

Figures 37c and 37d show the different fracture surfaces produced by changing the wire composition during the welding procedure. Weld (CSM + Ti/Mo)-OP, which does not contain boron in the weld metal as compared to weld TB-OP, exhibited an elongated dimple, tearing-type fracture mechanism at the notch, which reverted to equiaxed microvoid coalescence as the crack propagated onward. Both welds (CSM + Mo)-OP and CSM-OP show a small amount of microvoid coalescence at the notch center which then immediately transformed into a cleavage fracture mode as the crack propagated onward. Cleavage type fracture is a brittle type failure mode which will occur on the lower shelf of the transition curve and explains why both welds exhibited poor

impact toughness values. Weld (CSM + Mo)-OP, which does not contain titanium, shows a drastic difference in the fracture appearance when compared to weld (CSM + Ti/Mo)-OP. The fracture mechanism changes from a microvoid coalescence mode to a cleavage mode when titanium is not present in the weld metal. On the other hand, adding molybdenum to the weld metal, as in weld (CSM + Mo)-OP, does not seem to have much effect on the fracture appearance or the impact properties as compared to weld CSM-OP. The same correlation can be made between the fracture surfaces of these welds and their respective weld metal microstructures presented in Figure 19b. As the amount of AC (in this case bainite) in the weld metal increases [going from TB-OP to (CSM + Ti/Mo)-OP to (CSM + Mo)-OP to CSM-OP], the fracture surface changes from upper shelf microvoid coalescence to lower shelf cleavage.

III.5. EFFECT OF PRIOR AUSTENITE GRAIN SIZE

Weld metal oxygen content was plotted against the volume percent grain boundary ferrite for each weldment and these results are shown in Figure 38. As the weld metal oxygen increased from 0.011 to 0.051 weight percent, the grain boundary ferrite increased almost linearly from 5 to 18 percent. Figure 39 exhibits a virtually linear correlation between the weld metal oxygen content and the

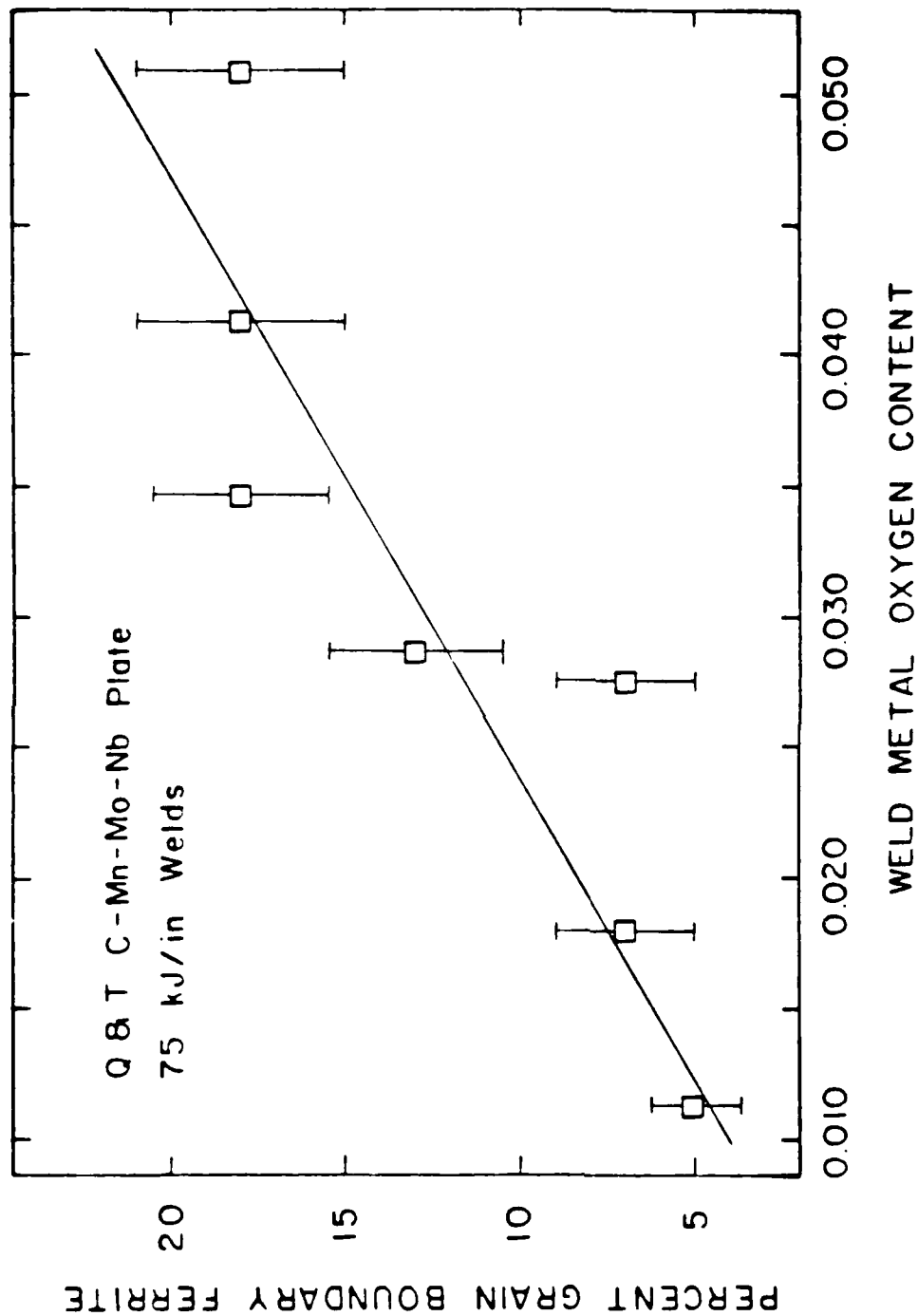


Figure 38. The volume percentage of grain boundary ferrite of submerged arc welds performed on quenched and tempered C-Mn-Mo-Nb plate as a function of their respective weld metal oxygen contents.

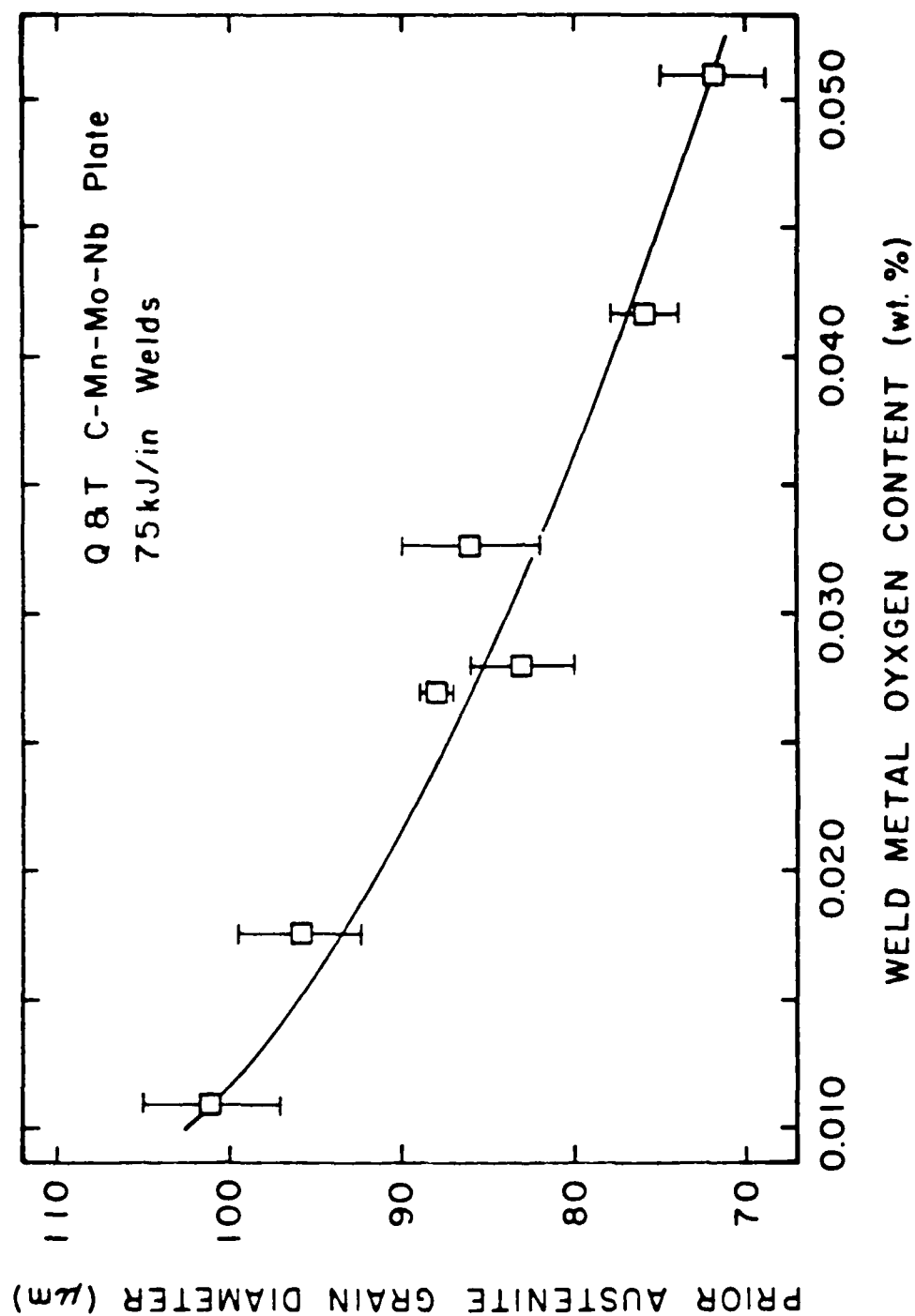


Figure 39. The prior austenite grain diameter of submerged arc welds performed on quenched and tempered C-Mn-Mo-Nb plate as a function of their respective weld metal oxygen contents.

prior austenite grain size. As the weld metal oxygen increased from 0.011 to 0.051 weight percent, the prior austenite grain size decreased from 100 to 70 microns. This can be explained by the work of Liu (88), which showed that increasing weld metal oxygen content increased the inclusion volume fraction, as shown in Figure 40. Furthermore, Liu also showed (see Figure 41) that the inclusion size decreased with increasing weld metal oxygen, if all the particles having a diameter greater than 0.08 microns are counted. This result is in contrast to the results of others (89-90), who have reported that average oxide particle size increased with increasing oxygen content. Fine second phase particles are known to increasingly inhibit grain growth as the particles get smaller and more abundant in the weld metal (91-92). This explains why increasing the weld metal oxygen content will decrease the prior austenite grain size. Figure 42 relates the prior austenite grain size to the amount of grain boundary ferrite, and shows that increasing amounts of grain boundary ferrite will be formed as the prior austenite grain size decreases. These results indicate that if the austenite grain size (which is dependent on the amount of oxygen) decreases, more austenite grain boundary surface will be available to provide nucleation sites for grain boundary

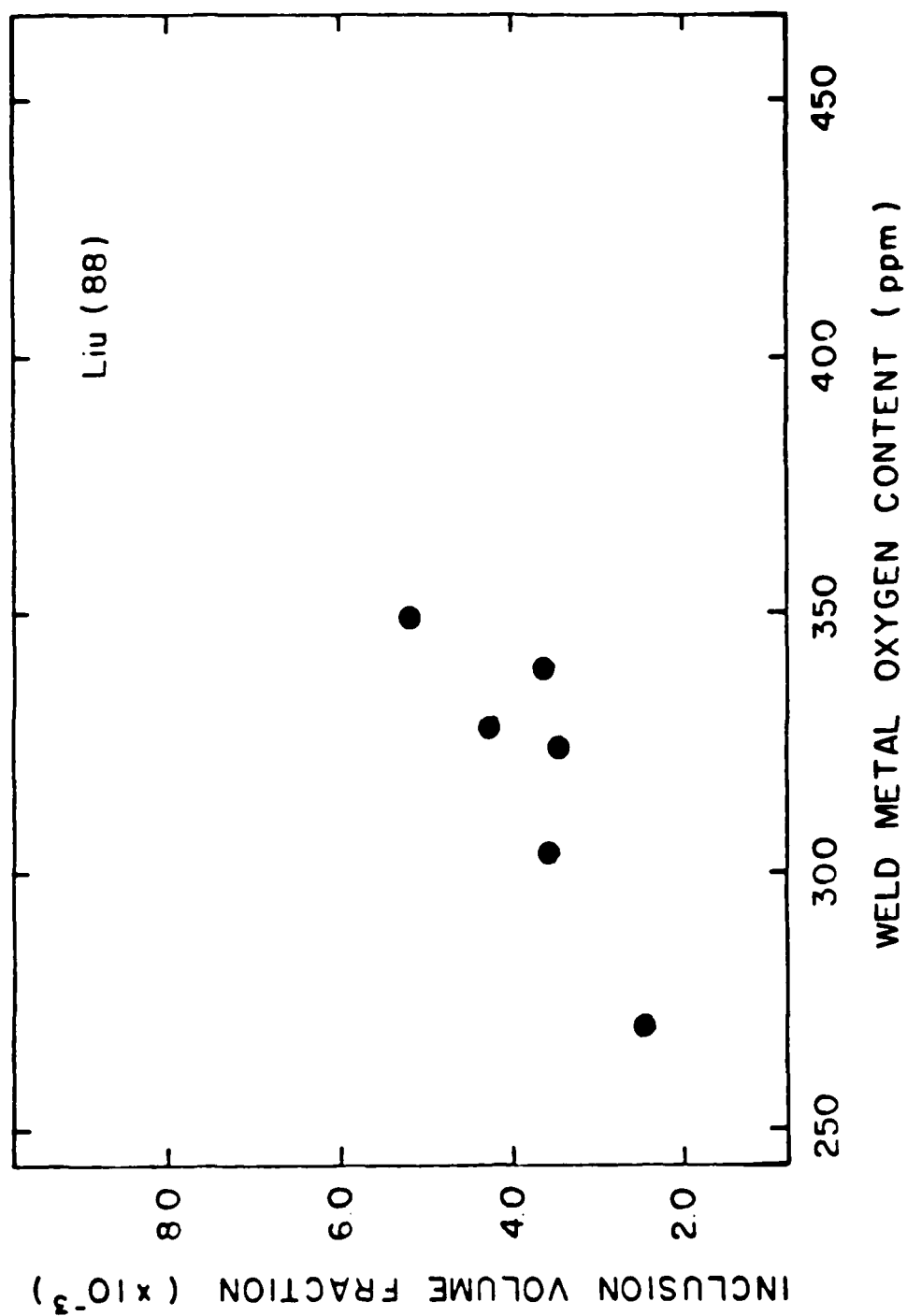


Figure 40. Effect of weld metal oxygen content on the inclusion volume fraction (88).

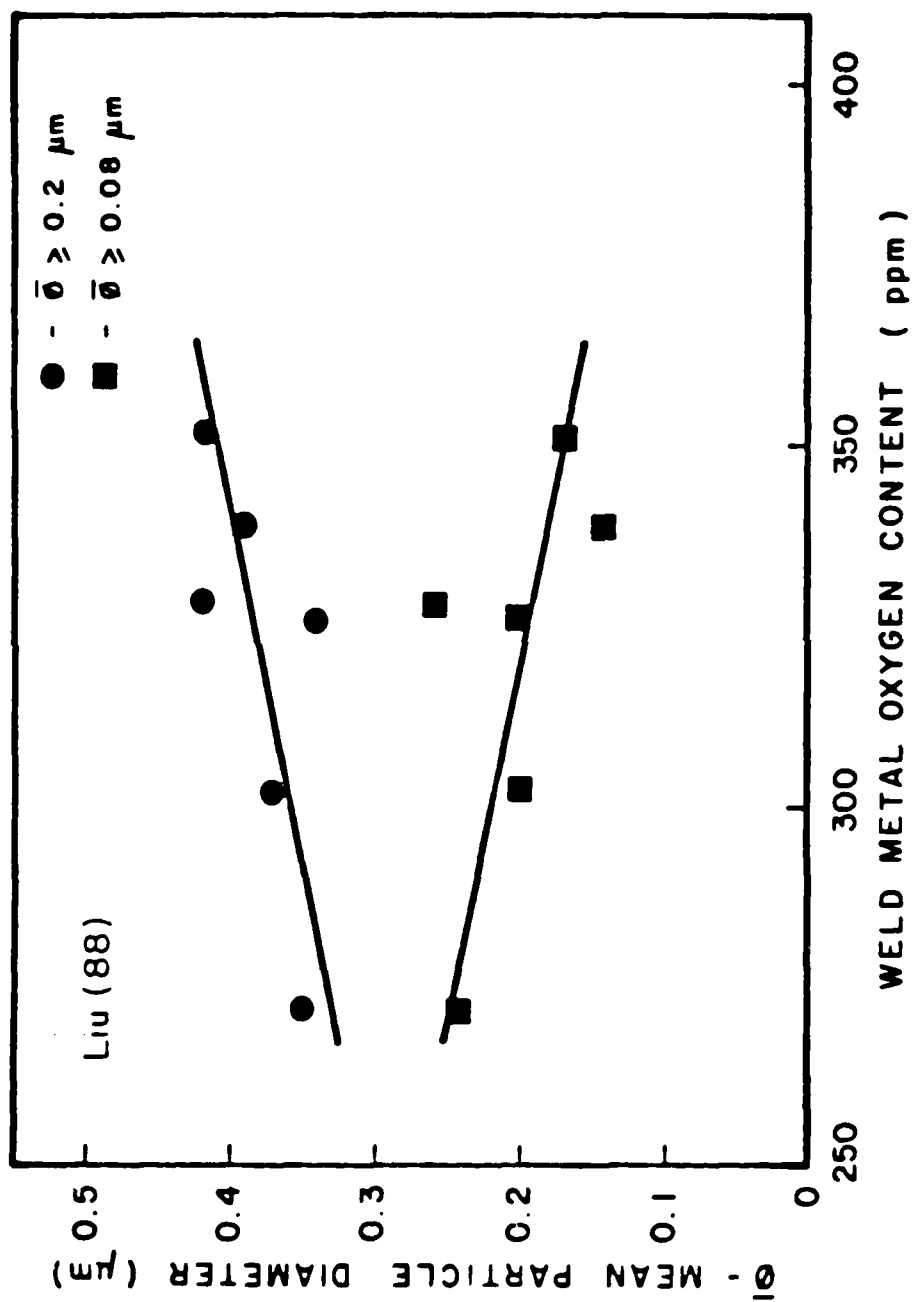
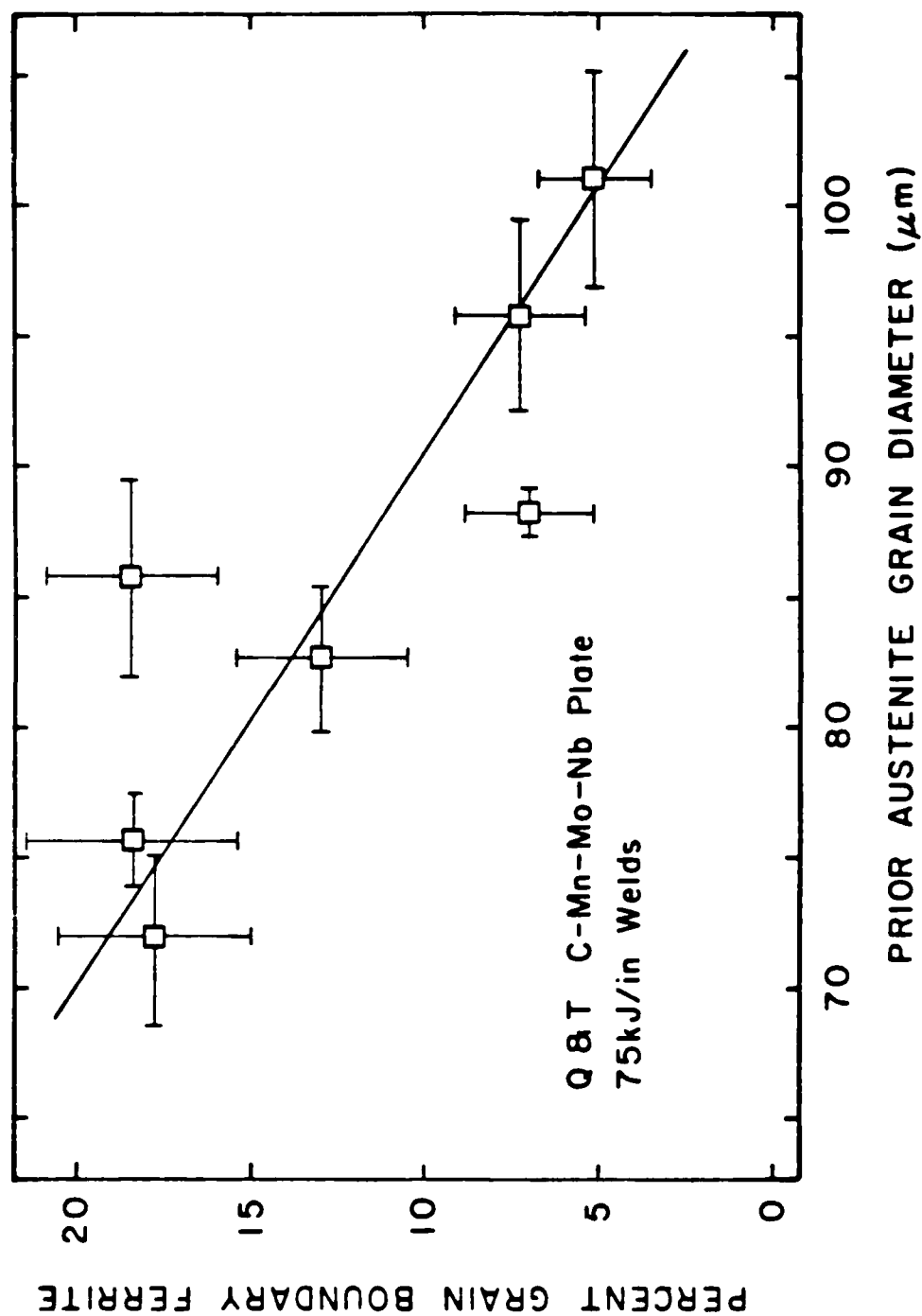


Figure 41. Effect of weld metal oxygen content on the mean particle diameter (88).

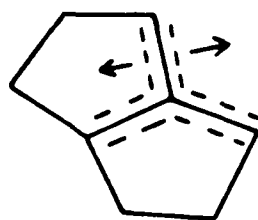


ferrite.

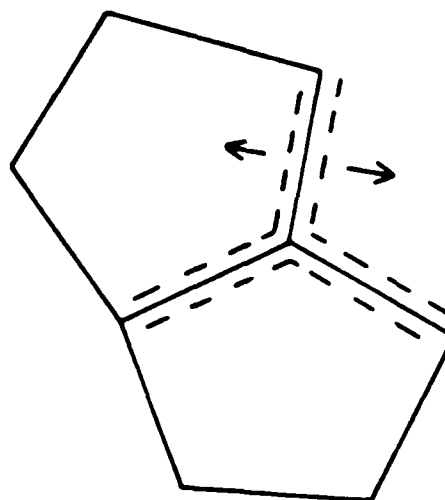
An approximate measure of the fraction of grain boundary ferrite created from a certain austenite grain size can be obtained from a specific form of the Avrami equation:

$$X = 1 - \exp(-2SGt) \quad (13)$$

where X is the volume fraction of allotriomorphic ferrite, S is the grain boundary area per unit volume, G is the growth rate of the ferrite/austenite boundary, and t is the reaction time. Figure 43 shows a schematic comparing low oxygen weld metal to high oxygen oxygen weld metal. The prior austenite grain size will be smaller for high oxygen weld metal contents, thus allowing more grain boundary ferrite to be nucleated which will be detrimental to weld metal properties. But for lower oxygen contents, a increase in austenite grain size will result, producing fewer nucleation sites for grain boundary ferrite. Thus, more acicular ferrite will be created, resulting in improved weld metal properties. Liu (88) modified Equation 13 by assuming: 1) that all the potential nucleation sites are consumed in the process (i.e. site saturation), 2) that diffusion-controlled growth occurs in both directions perpendicular to the boundary, and 3) that the grain shape



High Oxygen



Low Oxygen

AVRAMI KINETICS :

$$X = 1 - \exp \left(k t^{\frac{1}{2}} \right)$$

$$X = 1 - \exp \left(\frac{-4 \alpha t^{\frac{1}{2}}}{d} \right)$$

$$\ln(1-X) = \frac{(\text{const})}{d}$$

Figure 43. Schematic comparing low oxygen weld metal to high oxygen weld metal showing the Avrami relationship between the volume fraction of grain boundary ferrite and the prior austenite grain diameter.

is cylindrical. By using these assumptions he showed the growth rate to be:

$$G = dr/dt = 1/2\alpha t^{-1/2} \quad (14)$$

where α is a parabolic rate constant that has been measured by Kinsman and Aaronson (93) for various alloyed steels. Assuming that each grain is sharing with another, the surface area per unit volume can be shown to be:

$$S = \frac{4\pi dl}{d^2 l} * \frac{1}{2} = \frac{2}{d} \quad (15)$$

where d is the average diameter of the austenite grains. Putting these values into Equation 13, the following equation can be obtained:

$$X = 1 - \exp\left(\frac{-2\alpha t^{1/2}}{d}\right) \quad (16)$$

Taking the natural logarithm of both sides gives the following:

$$\ln (1 - X) = (-2\alpha t^{1/2}) * 1/d \quad (17)$$

Equation 17 indicates that the natural logarithm of the volume fraction of grain boundary ferrite transformed should be proportional to the reciprocal of the austenite grain diameter. Figure 44 shows the correlation between the average austenite grain diameter and the volume fraction of weld metal grain boundary ferrite. Christensen (94) showed that the reaction time ($\Delta t_{800-500}$) for submerged arc welds can be estimated if the plate thickness and heat input are known. By using a 3/4-in-plate thickness and a 3.0 KJ/mm heat input, a reaction time of 21 seconds was calculated for the experimental welds. Aaronson and Kinsman (93) measured the grain boundary ferrite thickness and plotted it against the growth time for iron-carbon alloys so that the parabolic rate constants could be calculated. Their maximum and minimum values of the rate constant for a 0.11 weight percent carbon alloy was calculated to be 3.0 and 2.0 $\mu\text{m}/\text{sec}^{1/2}$ respectively. By using 21 seconds for the reaction time and the maximum and minimum values for the parabolic rate constant, theoretical lines were calculated using Equation 17 and plotted on Figure 44 to see if the experimental data compared to the theoretical data. As Figure 44 shows, the experimental data fits in between the theoretical lines. Using a regression analysis on the experimental data, a value for α was calculated to be

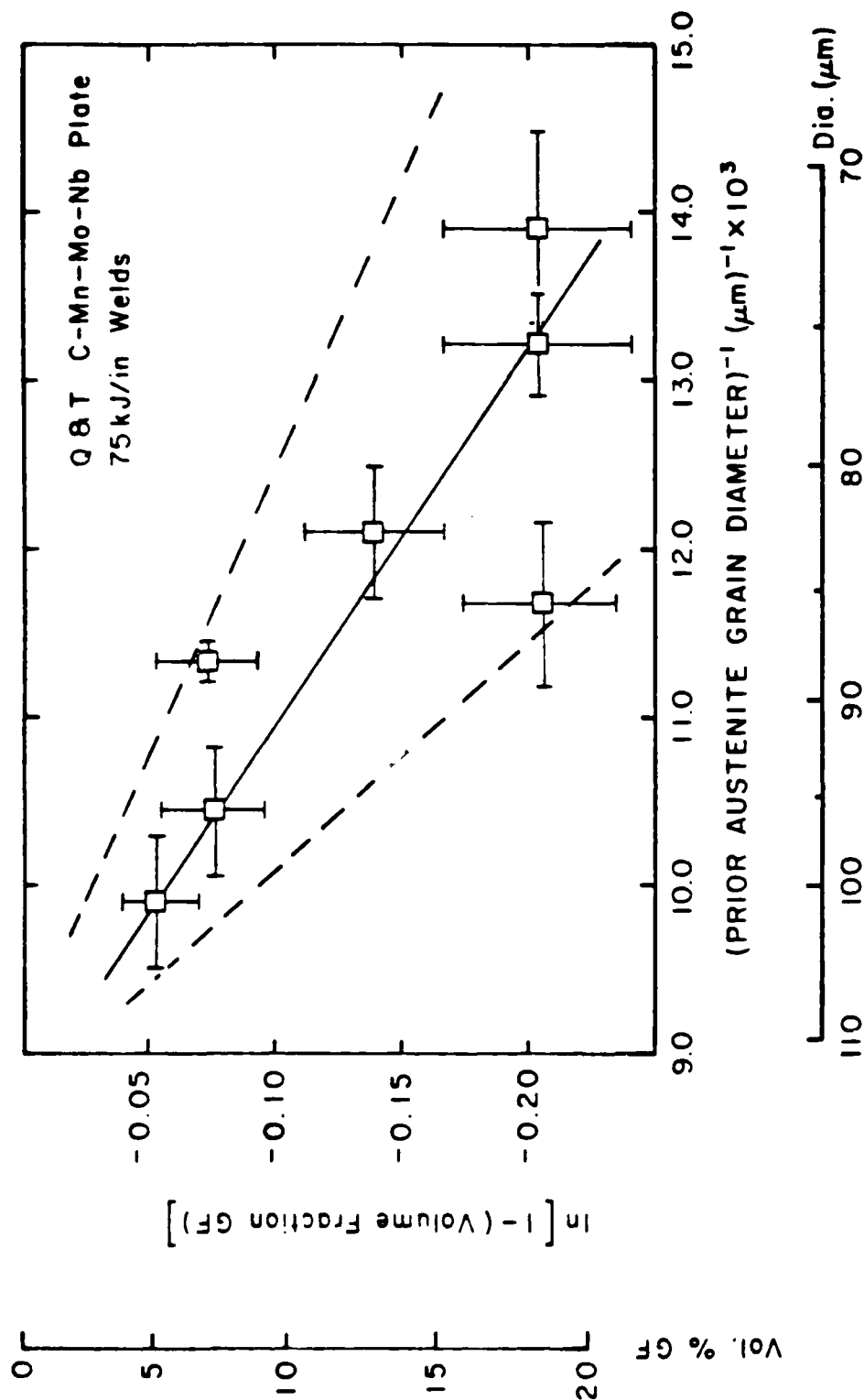


Figure 44. The volume fraction grain boundary ferrite of submerged arc welds performed on quenched and tempered C-Mn-Mo-Nb plate as a function of their respective prior austenite grain diameters.

2.4 $\mu\text{m}/\text{sec}^{1/2}$, which falls between the theoretical range of Aaronson and Kinsman (93). These data imply, by increasing the prior austenite grain size, the percent grain boundary ferrite will decrease in the weld metal, thus providing a better microstructure in terms of weld metal toughness. Although the austenite grain size is probably the most important parameter affecting the transformation of grain boundary ferrite, other factors such as weld metal boron content can also have an effect, as shown previously in Figures 28 and 29.

Transforming Equation 16 and assuming a constant for X and α , one can show that the square of the austenite grain diameter is directly proportional to the reaction time:

$$d^2 = \left(\frac{-2\alpha}{\ln 1-X} \right)^2 \cdot t \quad (18)$$

In the case of the seven experimental weldments, the largest prior austenite grain size (given in the Appendix) was approximately 100 microns, while the smallest grain size was approximately 70 microns. Therefore the ratio of the largest prior austenite grain size versus the smallest squared is:

$$\left(\frac{100}{70}\right)^2 = 2 \quad (19)$$

This result shows that no matter what constants are appropriate for α and X , the observed change in prior austenite grain size should effect the transformation time for all triomorphic ferrite by a factor of 2. This idea is schematically displayed in Figure 45. Increasing the prior austenite grain size from approximately 70 microns to approximately 100 microns decreases the transformation time for grain boundary ferrite by a factor of 2, thus producing a finer acicular ferrite microstructure.

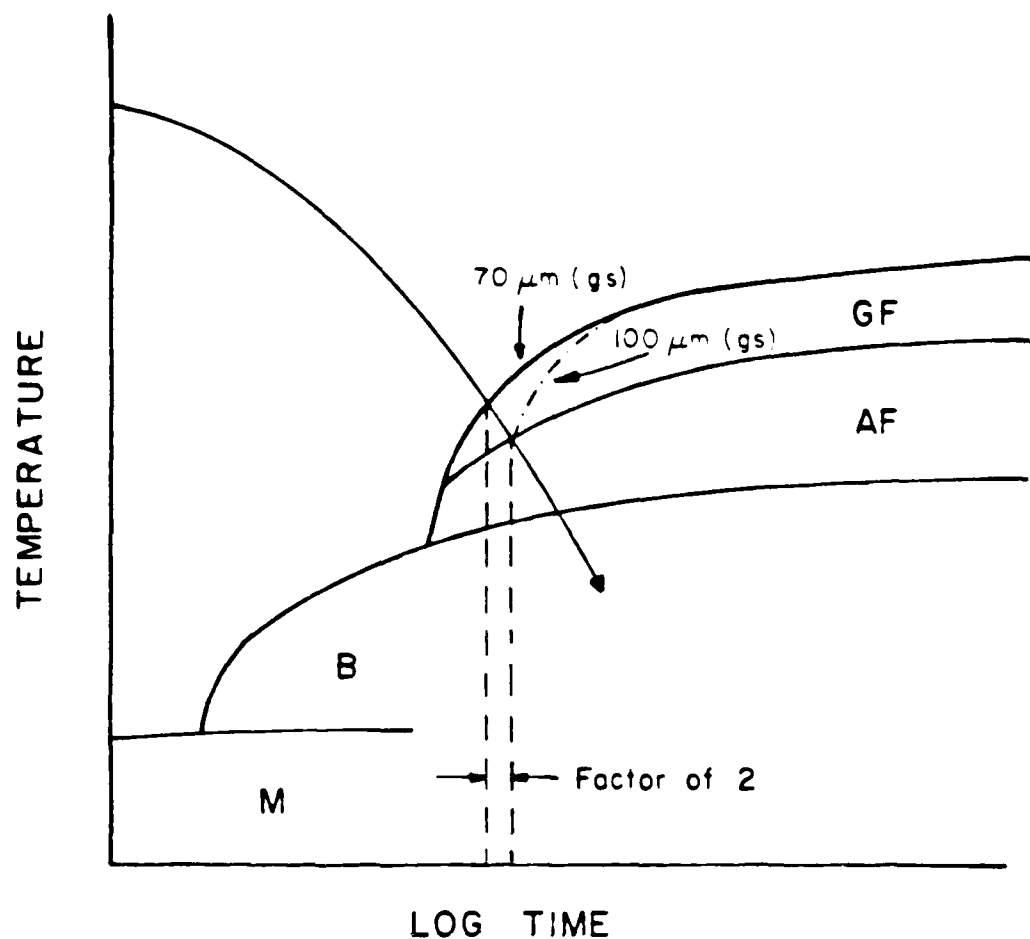


Figure 45. Schematic of a continuous cooling transformation diagram of a microalloyed HSLA steel weldment showing the effect of prior austenite grain size on weld metal microstructural transformation.

IV. CONCLUSIONS

1. The largest amount of weld metal acicular ferrite was produced in a quenched and tempered C-Mn-Mo-Nb base plate by using the commercially available OP121TT welding flux and the TiBor-22 welding wire. Weld metal made from these consumables also exhibited the best mechanical properties.
2. High SiO_2 fluxes produce weld metal which is high in oxygen and silicon and low in manganese and carbon. High oxygen welds contain relatively large volume fractions of grain boundary ferrite.
3. Replacing MgO with CaO in the flux produced a slightly coarser microstructure which exhibited poorer weld metal properties. This result implies that in welding fluxes, MgO does not simply and equivalently substitute for CaO as has been previously reported.

4. Increasing amounts of acicular ferrite, and thus decreasing amounts of primary ferrite, correspond with increasing Ito Bessyo carbon equivalent numbers (in the range of 0.18 - 0.22) for submerged arc welds performed on quenched and tempered C-Mn-Mo-Nb plate.
5. Microalloy additions of titanium and boron, together with low oxygen activity, are effective in producing weld metal with large fractions of fine acicular ferrite.
6. Increasing weld metal oxygen content will create many fine oxides which pin the austenite grain boundaries and decrease the prior austenite grain size, thus producing more surface area for grain boundary ferrite nucleation.

7. A predominant effect of high weld metal oxygen content is to increase the volume fractions of grain boundary ferrite through a reduction in austenite grain size. Fractions of grain boundary ferrite can be adequately predicted by means of well-established overall transformation kinetics theory.

REFERENCES CITED

1. D. J. Abson and R. E. Dolby: Welding Institute Research Bulletin, (June 1976).
2. L. G. Taylor and R. A. Farrar: Welding and Metal Fabrication, V. 43, p. 305, (1975).
3. L. Davis: An introduction to welding fluxes for mild and low alloy steels, The Welding Institute, (1981).
4. Ø. Grong and N. Christensen: Factors controlling weld metal chemistry, Final Technical Report to the European Research Office of The United States Army, Contract No. DAJA 37-81-C-0309, (August 1982).
5. R. A. Kubli and W. B. Sharav: Welding Journal, V. 40, p. 497s, (1961).
6. A. P. Bennett and P. J. Stanley: British Welding Journal, V. 34, p. 59, (1966).
7. W. J. Lewis, G. E. Faulkner, and P. J. Rieppel: Welding Journal, V. 39, p. 266s, (1960).
8. W. J. Lewis, G. E. Faulkner, and P. J. Rieppel: Welding Journal, V. 50, p. 337s, (1961).
9. J. E. Indacochea: Ph. D. Thesis, Colorado School of Mines, (1981).
10. J. E. Indacochea and D. L. Olson: Relationship of weld metal microstructure and penetration to weld metal oxygen content, ASM Conference on Welding Consumables and Process Developments, Peoria Illinois, (September 1981).
11. R. J. Parageter, Welding Institute Research Report No. 202/1978, (1978).
12. B. R. Keville and R. C. Cochrane: Steels for pipelines and pipe fittings, Metals Society, London, (1981).
13. S. S. Tuliani, T. Boniszewski, and N. F. Eaton: Notch toughness of commercial submerged arc weld metal, Welding and Metal Fabrication, V. 37, p. 327, (1969).

14. N. Mori, H. Homma, S. Okita, and M. Wakabayashi: Mechanism of notch toughness improvement in Ti-B bearing weld metals, IIW Doc. IX-1196-81, (May 1981).
15. D. J. Abson and R. E. Dolby: Microstructural transformations in steel weld metals - a reappraisal. Welding Institute Research Bulletin, pp. 202-207, (July 1978).
16. J. G. Garland and P. R. Kirkwood: Towards improved submerged arc weld metal, Metal Construction, p. 275, V. 7, (1975).
17. T. W. Eager: Sources of weld metal oxygen contamination during submerged arc welding, Welding Journal, V. 57, p. 76s, (March 1978).
18. J. E. Indacochea and D. L. Olson: Unpublished work, Colorado School of Mines, (1981).
19. J. H. Palm: Welding Journal, V. 51, p. 358s, (1972).
20. T. H. North, H. B. Bell, A. Nowicki, and I. Craig: Slag/metal interaction, oxygen and toughness in submerged arc welding, Welding Journal, V. 57, p. 63s, (March 1978).
21. M. A. B. Noor, T. H. North, and H. B. Bell: Welding and Metal Fabrication, V. 46, p. 194, (1978).
22. K. Mori: A new scale of basicity in oxide slags, Bulletin of the Faculty of Engineering, Ibaraki University, V. 2, p. 45, (1960).
23. D. Wood: The case for determining the silica activity of submerged arc fluxes, Presentation to the Welding Institute, (1975).
24. J. Wegrzyn: Properties of mild steel submerged arc welds made with neutral and basic fluxes, Institute of Welding, Gliwice, Poland, IIW Doc. II-A-384-75, (1975).
25. Classification of microstructures in low C - low alloy steel weld metal and terminology, Committee of Welding Metallurgy of Japan Welding Society, IIW Report, IX-1282-83, (1983).

26. C. A. Dube, H. I. Aaronson, and R. E. Mehl: Rev. Met., V. 55, p. 201, (1958).
27. H. I. Aaronson: Decomposition of austenite by diffusional processes, AIME, Philadelphia, p. 389, (1960).
28. R. C. Cochrane: British Steel Corporation Report No. T/PDM/462/1/77/C, V. 1, p. 462, (1977).
29. D. J. Widgery and T. G. Davey: IIW Doc. IIA-389-76, (1976).
30. D. J. Abson and R. E. Dolby: Welding Institute Research Bulletin, p. 100, (April 1980).
31. R. J. Parageter: IIW Doc. IX-J-37-80, (1980).
32. M. N. Watson, P. L. Harrison, and R. A. Farrar: Welding and Metal Fabrications, p. 161, (March/April/May 1981).
33. E. Levine and D. C. Hill: Metal Construction, p. 346, (1977).
34. E. Levine and D. C. Hill: Structure-property relationships in low carbon weld metal, Metallurgical Transactions, A8, p. 1453, (1977)
35. J. M. Sawhill: Climax Molybdenum Report No. L176-115, pp. 21-32 (1973).
36. C. L. Choi and D. C. Hill: Welding Journal, V. 57, p. 232s, (1978).
37. A. G. Glover, J. T. McGrath, M. J. Tinkler, and G. C. Weatherly: The Influence of Cooling Rate and Composition on Weld Metal Microstructures in C/Mn and HSLA Steel, pp. 267s-273s, (September 1977).
38. A. J. Pacey and K. W. Kerr: Welding and Metal Fabrication, V. 46, p. 613, (1978).
39. D. J. Abson, R. E. Dolby, and P. H. M. Hart: The role of non-metallic inclusions in ferrite nucleation in carbon steel weld metals. Welding Institute Research Bulletin, p.75, (November 1978).

40. Itoh and Nakanishi: Yosetsu Gakkaishi Journal, V. 44, p. 728, (1975).
41. Itoh and Nakanishi: Yosetsu Gakkaishi Journal, V. 44, p. 815, (1975).
42. I. Watanabe and T. Kojima: Role of titanium and boron in refinement of microstructure - Report 2, Presented at the Spring National Congress 1979, p. 772, (1980).
43. Y. Kikuta, T. Araki, M. Yoneda, H. Yoshida, and H. Kabata: IIW Doc. IX-1162-80, (1980).
44. Itoh, Nakanishi, and Komizo: Yosetsu Gakkaishi Journal, V. 52, p. 111, (1982).
45. R. C. Cochrane and P. R. Kirkwood: The effects of oxide inclusions on weld metal metal microstructures. Presented at The Metals Society Conference "Modern Metallography", University of Strathclyde, (September 1977).
46. A. P. Coldren, Y. E. Smith, and R. L. Cryderman: Toward Improved Ductility and Toughness, in Symposium. AMAX Foundation, p. 119, Kyoto (1971).
47. G. M. Evans: Effect of manganese on the microstructure and properties of all-weld-metal deposits, Welding Journal Supplement, p. 67s, (March 1980).
48. R. J. Jesseman: in Microalloying 75, New York, Union Carbide Corporation, (1977).
49. D. J. Abson and P. H. M. Hart: An investigation into the influence of Nb and V on the microstructure and mechanical properties of submerged arc welds in C-Mn steels - Phase 1, Welding Institute Members' Report, 122/1980, p. 122, (September 1980).
50. G. Bernard and B. Chevet: Soudage Tech. Connexes, (January - February 1976).
51. Y. Yoshino and R. D. Stout: Welding Journal, V. 3, p. 59s, (1979).

52. J. Wegrzyn and J. Dziubinski: The effect of minor additions of vanadium and niobium in the submerged arc weld metal on its mechanical properties and resistance to brittle fracture, IIW Doc. XIIA-145-77, (December 1976).
53. N. E. Hannerz, G. Valland, and K. Easterling: Influence of Nb on the microstructure and mechanical properties of submerged arc weld metals for C-Mn steels, IIW Doc. II-612-72, IX-798-72, (1972).
54. J. M. Sawhill and T. Wada: Welding Journal, V. 1, (1975).
55. P. R. Kirkwood and J. G. Garland: Welding and Metal Fabrications, (January - February 1977), (March - April 1977).
56. A. H. Koukabi, T. H. North, and H. B. Bell: Metal Construction, p. 639 (1979).
57. P. R. Kirkwood and J. G. Garland: Metallurgical factors controlling weld metal toughness in the seam welding of line pipe, symposium on pipeline steel, St Louis, American Welding Society, May 1976, Welding Research Council, (1977).
58. N. E. Hannerz and B. M. Jonsson-Holmquist: Metal Construction, V. 2, (1974).
59. R. E. Dolby: The effects of V and Nb on weld metal properties, Presented at The Metals Society Conference at Grosvenor House, London, (October 1981).
60. N. Mori, H. Homma, S. Okita, and O. Asano: The behavior of B and N in notch toughness improvement of Ti-B bearing weld metals, IIW Doc. IX-1158-80, (1980).
61. H. Terashima, N. Nishiyama, and J. Tsuboi: Effects of Ti, Al, and N on toughness in 60 kg/mm² class submerged-arc weld metal, Proceedings, Annual Assembly of the Japanese Welding Society 80-81, (1981).
62. H. Homma, N. Mori, S. Saito, and K. Shinmyo: Effects of titanium-boron and niobium additions on the mechanical properties of submerged arc weld metals, IIW Doc. XII-E-10-78, IX-1072-78, (1978).

63. K. Shinmyo, S. Saito, N. Mori, T. Takami, and R. Kono: A new submerged arc welding flux for offshore structure in arctic use, IIW Doc. XII-A-138-77 (1977), IX-1073-78, (1978).
64. K. Hirabayashi, T. Taira, T. Yamaguchi, and K. Takashige: Improvement of toughness of submerged arc weld metal of low temperature service line pipe, IIW Doc. XII-A-135-77, (1977).
65. A. Shiga, H. Imura, and J. Tsuboi: Effects of niobium and vanadium on toughness of submerged arc weld metal, IIW Doc. XII-A-149-77, (1977).
66. Y. Ito, and M. Nakanishi: Study on charpy impact properties of weld metal with submerged arc welding, IIW Doc. XII-A-113-75, (1975).
67. R. D. Thomas: Submerged arc welding of HSLA steels for low temperature service, IIW Doc. XII-A-143-77, (1977).
68. I. Masumoto: Effects of micro-alloying elements on toughness of steel weld metal, IIW Doc. XII-E-38-79, (1979).
69. I. Watanabe, M. Suzuki, and T. Kojima: Applicability of large current MIG arc welding techniques, Presented at International Conference in Osaka Japan, (October 1980).
70. A. H. Koukabi, T. H. North, and H. B. Bell: Properties of submerged arc deposits - Effects of zirconium, vanadium, and titanium/boron, Metal Construction, V. 11-12, pp. 639-644, (1979).
71. Y. Ito, M. Nakanishi, and Y. Konizo: Effect of oxygen on transformation of low carbon weld metal, IIW. Doc. IX-1194-81, (1981).
72. R. C. Cohrane and P. R. Kirkwood: The effect of oxygen on weld metal microstructure, Trends in Steel and Consumables for Welding, International Conference London, p. 103, (November 1978).
73. J. G. Garland and P. R. Kirkwood: Welding and Metal Fabrication, V. 44, p. 217, (1976).

74. P. R. Kirkwood: Metal Construction, V. 10, p. 260, (1978).
75. B. R. Keville: British Steel Corporation Report No. T/WE/1137/1/79/C, V. 1, p. 1137, (April 1979).
76. R. J. Parageter: Investigation of submerged arc weld metal inclusions, Welding Institute Research Report No. 151/1981, p. 151, (1981).
77. Estimating the average grain size of metals, Annual Book of ASTM Standards, E 112-81 (1981).
78. T. Gladman and J.H. Woodhead: The accuracy of point counting in metallographic investigations, Journal of the Iron and Steel Institute, pp. 189-193, (February 1960).
79. Standard methods for notched bar impact testing of metallic materials, 1982 Annual Book of ASTM Standards, E 23-82, p. 288, (1982).
80. Standard methods of tension testing of metallic materials, 1982 Annual Book of ASTM Standards, E 8-81, p. 208, (1982).
81. N. J. Petch: J. Iron Steel Institute, London, V. 173, p. 25, (1953).
82. Y. Ito and K. Bessyo: A prediction of welding procedure to avoid heat affected zone cracking, IIW Doc. No. 1X-631-69, (1969).
83. B. A. Graville: Cold cracking in welds in HSLA Steels, in welding of HSLA (microalloyed) structural steels, ASM and Associazione Italiana di Metallurgia, Edited by A. B. Rothwell and J. Malcolm Gray, p. 85, (1976).
84. H. Suzuki: Carbon equivalent and maximum hardness, IIW Doc. No. 1X-1279-83, (1983).
85. Ø. Grong: Microstructural developments in HSLA steel weld metals, To be published in International Metals Review, (1984).

86. E. D. Hondros and M. P. Seah: Interfacial and surface microchemistry, Physical Metallurgy, Elsevier Science Publishers BV, Chapter 13, (1983).
87. J. Tsuboi and H. Terashima: Review of strength and toughness of Ti and Ti-B microalloyed deposits, Welding in the World, V. 21, pp. 304-316, (1983).
88. S. Liu: The role of non-metallic inclusions in controlling weld metal microstructures in niobium microalloyed steels, Ph. D. Thesis No. T-2923, Colorado School of Mines, (1974).
89. R. C. Cochrane, J. L. Ward, and B. R. Keville: The influence of deoxidation and/or desulphurisation practice on the weld metal toughness of high dilution welds, Given in Proc. Intl. Conf. on The effects of residual, impurity, and micro-alloying elements on weldability and weld properties, London, The Welding Institute, Paper 16, (1983).
90. M. Ferrante and R. A. Farrar: The role of oxygen rich inclusions in determining the microstructure of weld deposits, Journal of Materials Science, V. 17, p. 3293, (1982).
91. Jefferies, Zay, and Archer: The science of metals, McGraw-Hill Book Co., Inc, New York, p. 95, (1924).
92. Zener, as quoted by C. S. Smith: Trans. AIME, V. 15, p. 175, (1948).
93. K. R. Kinsman and H. I. Aaronson: Influence of Al, Co, and Si upon the kinetics of the proeutectoid ferrite reaction, Metallurgical Transactions, V. 4, pp. 959-967, (April 1973).
94. N. Christensen: Welding metallurgy, Welding Compendium, The Norwegin Institute of Technology, Trondheim, Norway, p. 89, (1981).

Appendix A. Weld Metal Dilution, Weld Penetration, and
Bead Area of the Welds

Weld	Dilution %	Penetration (mm)	Bead Area (mm ²)
TB-OP	62.6	10.4	690
TB-CaO	52.5	7.5	630
TB-MgO	57.7	9.9	670
TB-SiO ₂	61.8	8.7	650
(CSM+Ti/Mo)-OP	60.4	8.5	540
(CSM+Mo)-OP	53.0	6.1	530
CSM-OP	59.8	10.0	720

Appendix B. Summary of the Average Acicular Ferrite
Lath Size and the Average Prior Austenite Grain Size Diameter

Weld	Acicular Ferrite Lath Spacing (μm)	Prior Austenite Grain Diameter (μm)
TB-OP	1.44	88
TB-CaO	1.50	102
TB-MgO	1.81	96
TB-SiO ₂	1.91	72
(CSM+Ti/Mo)-OP	1.98	86
(CSM+Mo)-OP	2.10	83
CSM-OP	2.40	75

Appendix C. Summary of the Hardness Measurements of the Welds

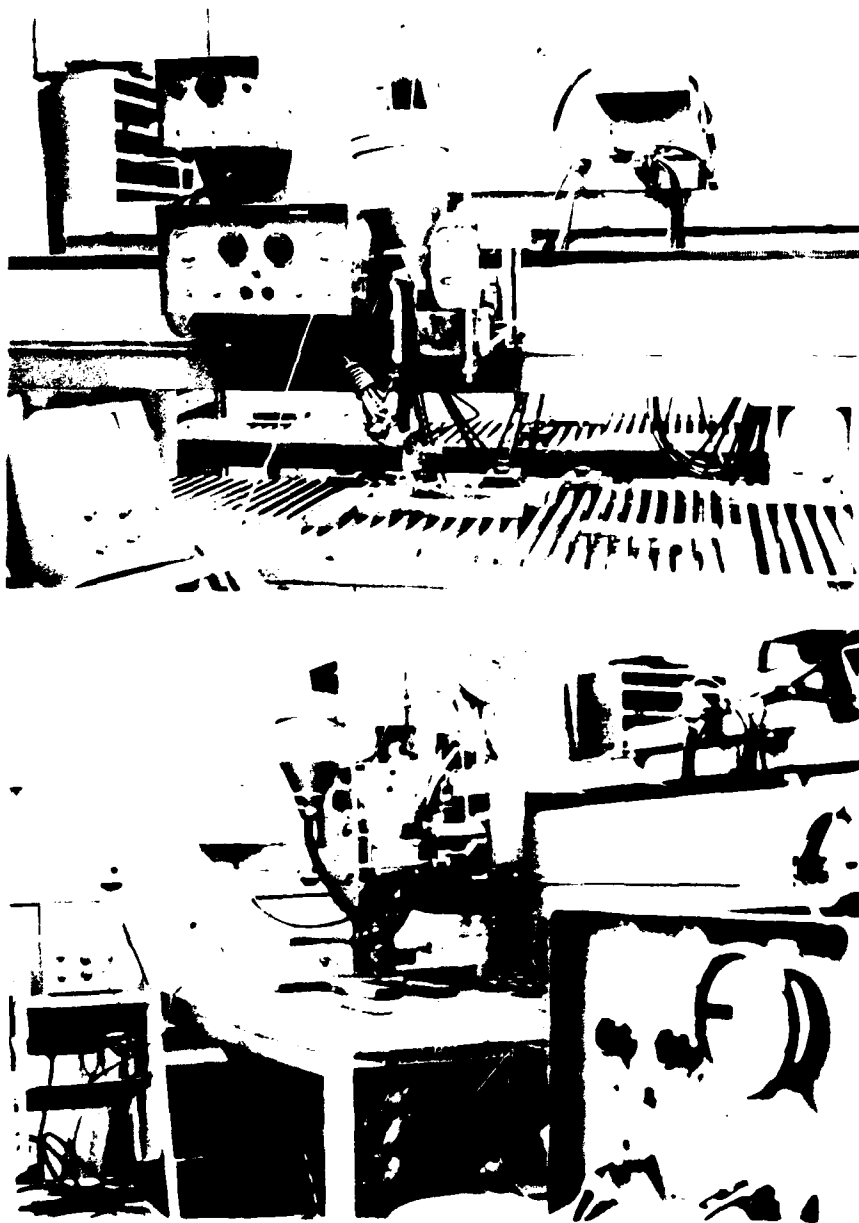
Weld	Macrohardness Average (DPH)	Microhardness Average (DPH)
TB-OP	237	223
TB-CaO	225	238
TB-MgO	231	224
TB-SiO ₂	226	220
(CSM+Ti/Mo)-OP	222	230
(CSM+Mo)-OP	222	230
CSM-OP	209	215

Appendix D. Calculation of the Amount of Boron Per Grain Boundary Area of the Welds.

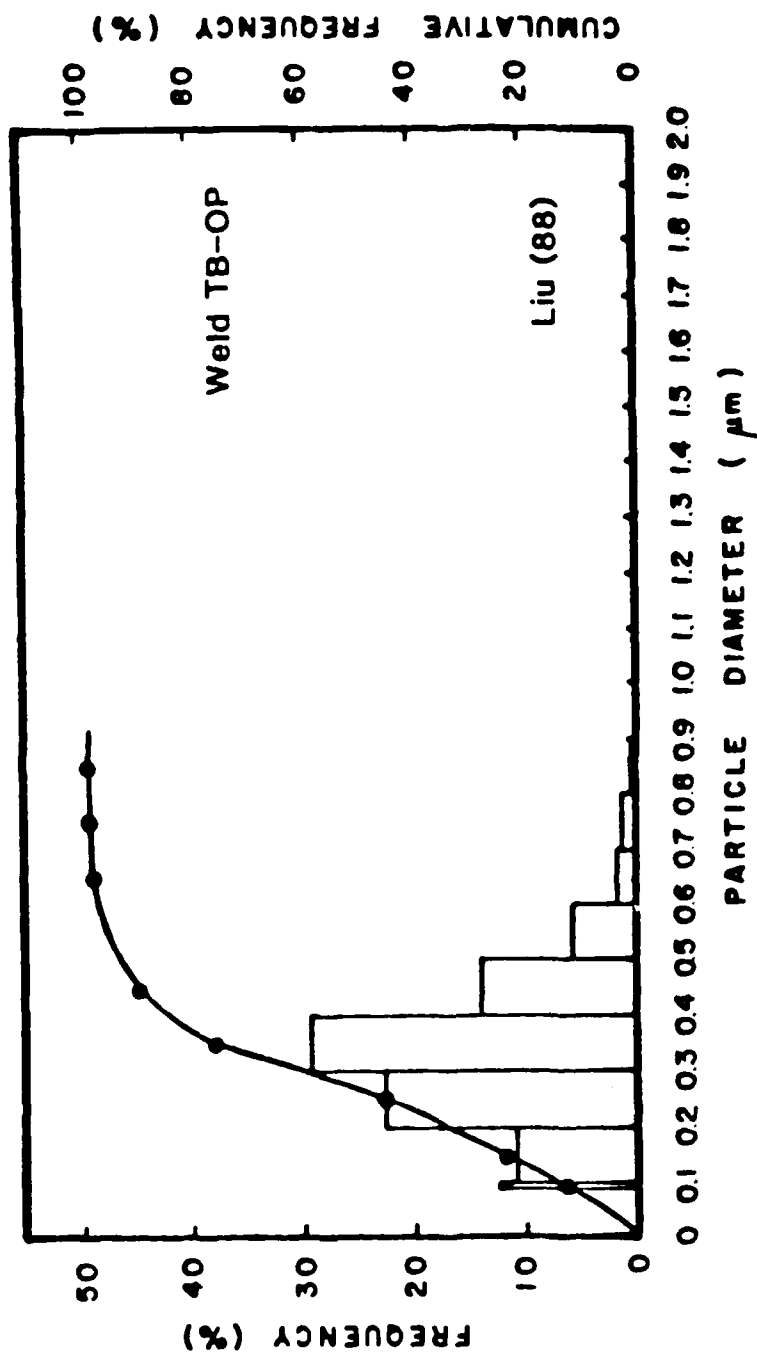
$$\text{wt. \% Boron of weld} \times \frac{1 \text{ mole B}}{10.8 \text{ g. B}} \times \frac{6.02 \times 10^{23} \text{ atoms B}}{1 \text{ mole B}} \times \frac{7.8 \text{ g. matrix}}{1 \text{ cm}^3} \times \frac{\gamma \text{ g.s. (cm)}}{2}$$

$$= \frac{\text{No. of atoms of Boron}}{\text{cm}^2} = \text{Grain Boundary Boron Concentration}$$

where γ g.s. is the prior austenite grain size diameter for each weld.



Appendix E. Submerged arc welding machine used for bead on plate weld tests.



Appendix F. Simple and Cumulative Size Distribution of the Inclusions Extracted From Weld TB-OP (88).

Appendix G. Chemical Composition of the Inclusions
Extracted From Weld TB-OP (88).

Mn (%)	Si (%)	Al (%)	Fe (%)	Ti (%)	S (%)
42.7	7.3	21.0	0	9.9	19.1
46.2	1.0	29.9	0	2.1	20.9
48.7	5.2	17.9	0	2.3	26.0
19.0	17.1	19.3	29.3	0	15.4
27.3	9.2	47.3	5.2	2.8	8.3
24.1	7.7	55.7	4.0	6.2	2.4
25.7	18.7	40.4	0	8.8	6.4
40.5	0.9	36.8	5.3	1.8	14.7
22.0	7.2	45.9	6.1	15.6	3.2
27.5	3.9	56.0	3.9	6.7	2.0
50.5	3.5	12.5	8.4	0	25.0
25.8	11.7	49.1	5.6	4.5	3.3
25.4	1.0	61.7	3.8	7.4	0.8
28.0	10.8	44.3	4.4	9.4	3.1
34.4	5.1	37.1	5.4	5.1	13.0
54.0	1.8	5.6	7.4	0	31.4
0	19.8	66.6	10.2	0	3.5
21.8	15.5	38.9	8.4	11.5	4.0
27.0	4.6	56.6	4.4	5.2	2.3
25.9	8.0	44.4	6.3	13.1	2.4
34.9	6.0	36.8	5.7	10.4	6.2
0	72.3	0	27.8	0	0
16.6	38.0	23.2	0	17.9	4.5
20.3	29.5	34.9	0	10.5	4.9
25.4	14.0	45.0	5.1	0	10.5
10.5	43.5	39.2	6.9	0	0
29.8	4.4	58.8	0	3.9	3.1
24.6	4.2	59.0	4.3	6.3	1.7
29.5	8.3	36.8	6.7	6.4	12.5
0	63.9	7.9	28.2	0	0
45.2	4.3	27.3	0	2.5	20.8
27.6	6.4	55.9	4.6	3.3	2.2
30.5	5.0	48.9	9.0	5.2	1.5
29.5	8.2	27.6	12.5	5.4	17.0
17.5	11.1	60.7	7.8	3.0	0
42.0	3.8	30.5	0	6.4	17.3
26.3	13.7	36.3	0	23.7	0
35.7	4.0	36.4	5.1	1.8	17.1
28.4	4.8	54.5	0	4.6	7.7
0	38.5	42.9	18.6	0	0
31.1	69.0	0	0	0	0

INITIAL DISTRIBUTION

Copies

16 NAVSEA

1 (SEA 05M)
 1 (SEA 05R)
 2 (SEA 05R25)
 1 (SEA 05R26)
 2 (SEA 05M2)
 1 (SEA 05MP)
 2 (SEA 55Y)
 1 (SEA 55Y3)
 1 (SEA 55Y12)
 2 (SEA 99612)
 1 (PMS 400D)
 1 (PMS 400C)

12 DTIC

CENTER DISTRIBUTION

Copies

Code

Name

1	17	W. Murray
1	172	M. Krenzke
1	1720.4	A. Wiggs
1	173	A. Stavovy
1	1730.2	N. Nappi
2	1730.6	J. Beach
1	1740.3	M. Salive
1	28	J. Belt
1	2803	J. Cavallaro
1	2803	R. Hardy
1	2809	A. Malec
5	281	G. Wacker
1	2812	
1	2812	T. Scoonover
20	2814	J. Gudas
2	2815	P. Holsberg
1	2815	G. Franke
1	2815	R. Brenna
1	2816	A. Pollack
1	2816	R. Juers
1	2816	R. McCaw
5	522.1	Unclass Library
2	5231	Office Services

END

FILMED

2-85

DTIC